IEEE Access
Multidisciplinary | Rapid Review | Open Access Journal

Received November 8, 2019, accepted November 29, 2019, date of publication December 4, 2019,
date of current version December 23, 2019.

Digital Object Identifier 10.1109/ACCESS.2019.2957698

Battery Energy Storage Models for Optimal Control

DAVID M. ROSEWATER[1], (Member, IEEE), DAVID A. COPP[2], (Member, IEEE), TU A. NGUYEN[1], (Senior Member, IEEE), RAYMOND H. BYRNE[1], (Fellow, IEEE), AND SURYA SANTOSO[3], (Fellow, IEEE)

[1]Sandia National Laboratories, Albuquerque, NM 87185, USA
[2]Department of Mechanical and Aerospace Engineering, University of California at Irvine, Irvine, CA 92697, USA
[3]The Department of Electrical and Computer Engineering, University of Texas at Austin, Austin, TX 78712, USA

Corresponding author: David M. Rosewater (dmrose@sandia.gov)

This work was funded by the U.S. Department of Energy, Office of Electricity, through the Energy Storage Program.

ABSTRACT As batteries become more prevalent in grid energy storage applications, the controllers that decide when to charge and discharge become critical to maximizing their utilization. Controller design for these applications is based on models that mathematically represent the physical dynamics and constraints of batteries. Unrepresented dynamics in these models can lead to suboptimal control. Our goal is to examine the state-of-the-art with respect to the models used in optimal control of battery energy storage systems (BESSs). This review helps engineers navigate the range of available design choices and helps researchers by identifying gaps in the state-of-the-art. BESS models can be classified by physical domain: state-of-charge (SoC), temperature, and degradation. SoC models can be further classified by the units they use to define capacity: electrical energy, electrical charge, and chemical concentration. Most energy based SoC models are linear, with variations in ways of representing efficiency and the limits on power. The charge based SoC models include many variations of equivalent circuits for predicting battery string voltage. SoC models based on chemical concentrations use material properties and physical parameters in the cell design to predict battery voltage and charge capacity. Temperature is modeled through a combination of heat generation and heat transfer. Heat is generated through changes in entropy, overpotential losses, and resistive heating. Heat is transferred through conduction, radiation, and convection. Variations in thermal models are based on which generation and transfer mechanisms are represented and the number and physical significance of finite elements in the model. Modeling battery degradation can be done empirically or based on underlying physical mechanisms. Empirical stress factor models isolate the impacts of time, current, SoC, temperature, and depth-of-discharge (DoD) on battery state-of-health (SoH). Through a few simplifying assumptions, these stress factors can be represented using regularization norms. Physical degradation models can further be classified into models of side-reactions and those of material fatigue. This article demonstrates the importance of model selection to optimal control by providing several example controller designs. Simpler models may overestimate or underestimate the capabilities of the battery system. Adding details can improve accuracy at the expense of model complexity, and computation time. Our analysis identifies six gaps: deficiency of real-world data in control literature, lack of understanding in how to balance modeling detail with the number of representative cells, underdeveloped model uncertainty based risk-averse and robust control of BESS, underdevelopment of nonlinear energy based SoC models, lack of hysteresis in voltage models used for control, lack of entropy heating and cooling in thermal modeling, and deficiency of knowledge in what combination of empirical degradation stress factors is most accurate. These gaps are opportunities for future research.

INDEX TERMS Batteries, modeling, distributed energy resources, battery energy storage system (BESS), state-of-charge (SoC), state-of-health (SoH), energy storage, optimal control.

The associate editor coordinating the review of this manuscript and approving it for publication was Khmaies Ouahada.

Term	Meaning
Ah	- ampere-hour
BESS	- battery energy storage system

BoL - beginning-of-life
BMS - battery management system
CRM - charge reservoir model
EER - energy efficiency ratio
EMS - energy management system
EoL - end-of-life
ERM - energy reservoir model
EPRI - Electric Power Research Institute
HVAC - heating ventilation and air conditioning
kW - kilowatt
kWh - kilowatt-hour
LQR - linear quadratic regulator
MPC - model predictive control
P2D - pseudo two-dimensional model
SEI - solid electrolyte interphase
SNL - Sandia National Laboratories
SPM - single particle model
SoC - state-of-charge
SoH - state-of-health
SoL - state-of-life
ToU - time-of-use

Symbol	Decision variable description
p	- ac power provided to the BESS
p_{dc}	- dc power provided to the battery
i_{bat}	- dc current provided to the battery
v_{bat}	- battery terminal voltage
v_{oc}	- open-circuit-voltage
ς	- state-of-charge
c_p	- concentration in the cathode
c_n	- concentration in the anode
Φ_p	- cathode half-cell potential
Φ_n	- anode half-cell potential
η_p	- cathode overpotential
η_n	- anode overpotential
τ	- peak net electrical load
T	- battery surface temperature
T'	- battery internal temperature
T_{EN}	- BESS enclosure temperature
p_{HVAC}	- ac power provided to the HVAC unit of the BESS
$\dot{\varrho}$	- degradation rate (rate of change in SoH)
$\mathfrak{f}_{\text{d}}$	- aggregate degradation stress factor
S_{t}	- time degradation stress factor
S_ς	- state-of-charge degradation stress factor
S_{T}	- temperature degradation stress factor
δ	- depth-of-discharge
S_δ	- depth-of-discharge degradation stress factor
x	- generalized decision variable in a given application problem (subscript denotes model used: ERM, CRM, SPM, T (temperature), H (degradation))

Simplified vector, vector equation, and vector function notation

- If z is a decision variable, $\mathbf{z}$ is a column vector of decision variables. This is normally used to indicate decision variables at discrete times (e.g., p at each time-step in a control horizon becomes $\mathbf{p}$)

- The expression $\mathbf{z}_{[1:3]}$ denotes a column vector with the elements of $\mathbf{z}$ indicated by the index(es) (in this case, the first three elements)

- The expression $\mathbf{z} + \mathbf{y}$ denotes a column vector that is the element-wise addition of the vectors $\mathbf{z}$ and $\mathbf{y}$

- For the scalar value b, the expression $b[\mathbf{1}]$ denotes the multiplication of the constant (b), times a vector of ones ($[\mathbf{1}]$), that produces a column vector that is populated with b

- The vector equation $\mathbf{z} + \mathbf{y} = b[\mathbf{1}]$ denotes a number of equations equal to the length of $\mathbf{z}$ and $\mathbf{y}$, each with indexed variables (a.k.a, $\mathbf{z}_{[1]} + \mathbf{y}_{[1]} = b$, $\mathbf{z}_{[2]} + \mathbf{y}_{[2]} = b$, etc.)

- The vector equation $\mathbf{z} + \mathbf{y} = b[\mathbf{1}]$, can alternatively be written as $g(\mathbf{z}, \mathbf{y}) = [\mathbf{0}]$ where g is the vector function $g(\mathbf{z}, \mathbf{y}) = \mathbf{z} + \mathbf{y} - b[\mathbf{1}]$

Parameters

Model parameters are introduced and explained together as there are too many to list here. All parameters used in the application sections can be found in Tables 4, 5, 6, 11, and 13 respectively.

I. INTRODUCTION

Battery energy storage systems (BESS) can play an integral role in resilient and efficient power systems because of their ability to provide a range of energy services [1]. One of the fundamental problems in BESS integration within the electric power grid is designing control systems to maximize the value of energy services provided [2]. BESS models used in control systems formally represent assumptions about the physics underlying the conversion and storage of electrical energy. The BESS model is a critical element of effective control and operation of BESS that, ultimately, enables more resilient and efficient power systems.

The control objective for a BESS often involves minimizing an objective function (e.g., cost to the operator) subject to the constraints of the system. The controller must decide settings for both real and reactive power (decision variables), within limits on power, energy, state-of-charge (SoC), voltage, current, temperature, and state-of-health (constraints). Unlike in electric vehicles or consumer electronics (where the controller is an element of the battery management system (BMS) [3]), the BESS controller is an element of the energy management system (EMS), which is responsible for issuing control decisions for all devices within its purview (e.g., a home, building, microgrid, etc.). The BMS and EMS can share hardware and have overlapping responsibilities, as shown in Fig. 1, and often do not share a BESS model. Models used in BMSs are often developed by the battery manufacturers themselves and hence can contain detailed information about underlying chemical process not available

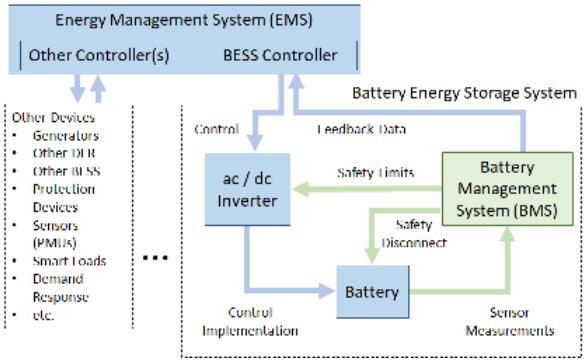

FIGURE 1. Typical energy management system control diagram.

to an EMS controller. Further, for applications that require accuracy at very high sample rates, such as power system stability, the inverter can have its own battery model for dynamic optimal control. This article focuses on optimal BESS control design within the EMS and so falls between the established fields of optimal control and battery modeling.

The methods for designing optimal controllers for energy storage systems have already been reviewed in [2]. Example methods as applied to BESS include model predictive control (MPC) [4]–[7], and linear quadratic regulator (LQR) control [8], [9]. While there are large differences between the methods for designing controllers, at the core of any approach is a model of the battery system. In this article, we will largely ignore what method is used to design the controller, instead focusing on the commonalities and differences between the models.

BESS models mathematically represent the physical dynamics and constraints of real systems. When choosing a BESS model, implicit assumptions are made about which physical dynamics are important to the controller's operation and which can be ignored. If a model ignores a state variable (e.g., temperature) that ends up as a constraining factor in the physical system, the control will be suboptimal. Similarly, if a model inaccurately represents a system state variable (e.g., battery state-of-charge), the controller will have to constantly correct for the modeling error and again will be suboptimal. However, consideration of which state variables to include and what physical dynamics to represent must inevitably be balanced with the complexity of the model and the computational burden of the controller [10]–[12]. The chart in Fig. 2 conceptually illustrates the trade-off between model accuracy and complexity. The model categories to the left on the chart are simple enough for control design and do not require detailed knowledge of battery cell construction and chemistry. At some level of model complexity there is a tipping point where the improvements in accuracy are too costly, in terms of computation or level of information required, to be useful in control design. Further, as there are thousands of individual cells in a BESS, there is logically some point at which it is better to represent more cells at the same level of detail rather than increasing the level of detail. These points are different depending on application and technology.

The goal of this article is to review the forms and functions of BESS models with critical attention to their advantages, disadvantages, and characteristics. This work will help readers navigate the complex trade-offs involved in designing a BESS controller. To explicitly define the scope of this review, we start with a general optimal control problem and then add detail relevant to BESS in order to classify different aspects of battery models. A general optimal control problem is formulated in:

$$\begin{aligned} &\min_{\mathbf{x}\in\mathbb{R}^m} f(\mathbf{x}) \\ &\text{subject to: } g(\mathbf{x}) = [\mathbf{0}] \\ &\qquad\qquad h(\mathbf{x}) \leq [\mathbf{0}] \end{aligned} \tag{1}$$

where $\mathbf{x}$ is a vector of decision variables, m is the total number of decision variables (roughly equal to number of BESS model variables $\times$ the number of time steps in the optimization time horizon), $f : \mathbb{R}^m \to \mathbb{R}$ is the objective function, $g : \mathbb{R}^m \to \mathbb{R}^r$ is a vector of equality constraints, and $h : \mathbb{R}^m \to \mathbb{R}^w$ is a vector of inequality constraints. In general, for BESS applications, the objective function to be minimized can be split into two terms: an objective associated with battery operation and degradation (f_b) and an objective associated with the service being provided (f_s). Further, the sets of constraints can be split into constraints dealing with the service (e.g., peak load constraint) and constraints based on the equipment (e.g., maximum battery voltage). This split is formalized in the multi-objective optimization problem in:

$$\begin{aligned} &\min_{\mathbf{x}\in\mathbb{R}^m} f_\mathrm{s}(\mathbf{x}) + f_\mathrm{b}(\mathbf{x}) \\ &\text{subject to: } g_\mathrm{s}(\mathbf{x}) = [\mathbf{0}] \\ &\qquad\qquad g_\mathrm{b}(\mathbf{x}) = [\mathbf{0}] \\ &\qquad\qquad h_\mathrm{s}(\mathbf{x}) \leq [\mathbf{0}] \\ &\qquad\qquad h_\mathrm{b}(\mathbf{x}) \leq [\mathbf{0}] \end{aligned} \tag{2}$$

The purpose of splitting the problem up is to isolate the components of the battery model (f_b, g_b, and h_b), as distinct from those of the service model (f_s, g_s, and h_s).

This article conducts a review of the battery model components of the problem in (2). Specifically, the objective functions $f_\mathrm{b}(\mathbf{x})$ and constraints $g_\mathrm{b}(\mathbf{x})$, and $h_\mathrm{b}(\mathbf{x})$ associated with optimal control of BESS. The inequality constraints $h_\mathrm{b}(\mathbf{x}) \leq 0$ ensure safe operation and battery longevity (e.g., preventing over-temperature $T \leq T_\mathrm{max}$, where T is the battery temperature, and T_max is the maximum temperature). The equality constraints generally represent a battery's physical dynamics and the mathematical relationships between variables (e.g., $p_\mathrm{dc} = v_\mathrm{bat} i_\mathrm{bat}$, where p_dc is the dc power, v_bat is the battery voltage, and i_bat is the battery current). The expression $f_\mathrm{b}(\mathbf{x})$ represents the BESS's contribution to the objective function based on the control action (e.g., where the objective is to minimize costs, $f_\mathrm{b}(\mathbf{x})$ may be $\mathrm{C}_\mathrm{EoL}\dot{\varrho}$, where C_EoL is the end-of-life cost and $\dot{\varrho}$ is the rate of change in state-of-health (SoH)). Our goal is to present the

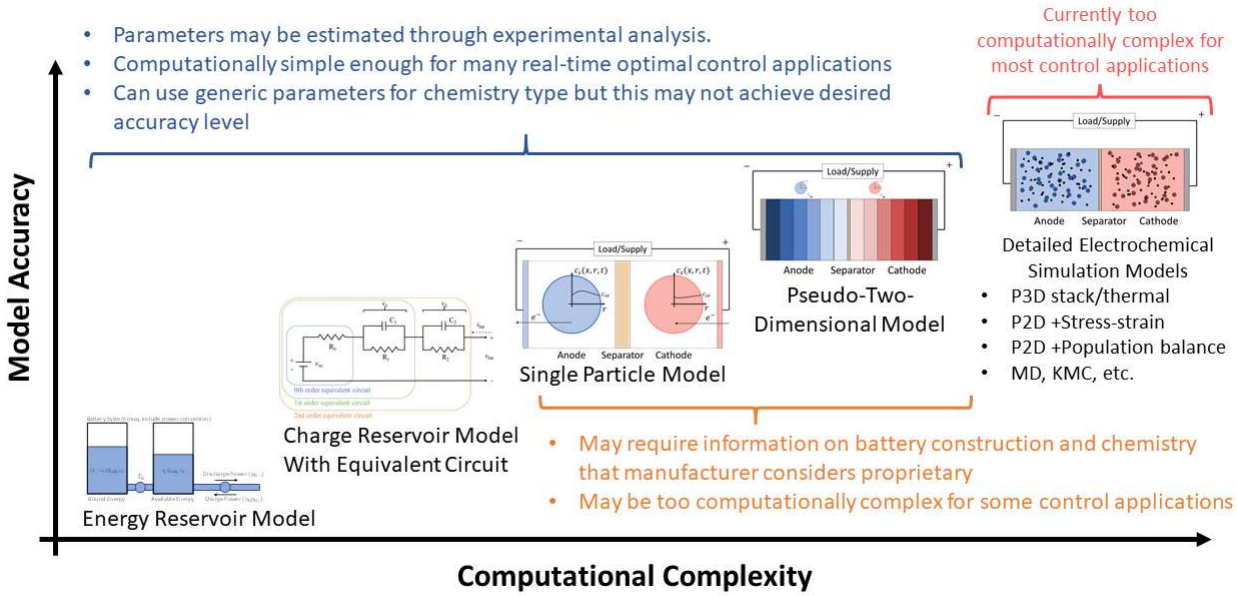

FIGURE 2. Illustration of the trade-off between model accuracy and complexity (computational complexity equates to CPU time, and model accuracy has also been referred to as "predictability" [12]).

advantages and disadvantages of various models to inform design and further research on optimal control of BESS.

This article is organized as follows. Section II establishes an example scenario used in each model domain section to demonstrate its application. Section III introduces the various models for state-of-charge, Section IV discusses temperature models, and Section V discusses battery degradation models. Each of these sections first introduces the model's functions, state variables and physical dynamics, and then includes a representative controller design. Section VI discusses broad trends and observations on the state-of-the-art including identified gaps, and Section VII provides a summary and conclusions.

II. PROBLEM STATEMENT

In this article we introduce models for different battery system dynamics. To illustrate the impact of different classes of models on control system performance, a representative controller is formulated for each modeling domain. This section establishes our example scenario in the form of a problem statement. A summary of scenario assumptions can be found in Table 1.

We consider a commercial electrical customer billed for both time-of-use (ToU) energy and peak-demand charges. This customer decides to purchase and install a battery to reduce their electricity bill. The customer's energy contract charges 9 ¢/kWh during off-peak hours, 11 ¢/kWh during partial-peak hours, and 15 ¢ during peak hours according to the schedule in Fig. 3 (top) [13]. The utility then charges a \$50/kW service fee according to the peak net load measured during the billing period. This price is consistent with demand charges in specific localities in California and New York [14].

TABLE 1. Summary of case study assumptions.

Ownership	Commercial Electrical Customer
Load Profile	From the EPRI test circuit 'Ckt5' loadshape summer, scaled to a 1.0 MW peak [15].
ToU Tariff	9 ¢/kWh off-peak, 11 ¢/kWh partial-peak hours (9:00 to 21:00), 15 ¢/kWh peak (12:00 to 18:00) [13]
Demand Tariff	ν = \$50/kW based on peak net load [14].
Billing	Daily, 15 minute time steps.

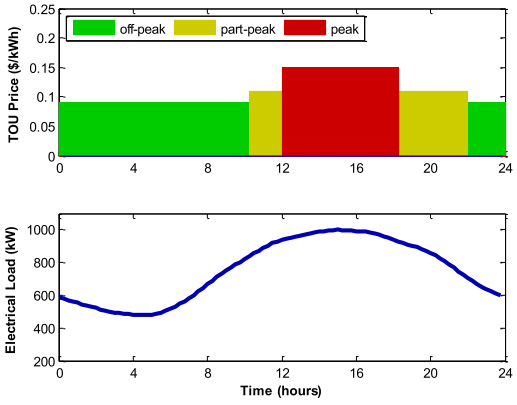

FIGURE 3. Time-of-use price schedule (top), and customer electrical load (bottom) [15].

The load data used for this problem, as shown in Fig. 3 (bottom), are adapted from the EPRI test circuit 'Ckt5' loadshape, normalized to a 1.0 MW peak [15]. We will assume that the load and price are known a priori. Without the battery, the total bill would be calculated according to:

$$f_s = \Delta t\, \mathbf{w}^\top \mathbf{l} + \max(\mathbf{l})\, \nu \tag{3}$$

where $\mathbf{l} \in \mathbb{R}^n$ is the load (kW) over time, $\mathbf{w} \in \mathbb{R}^n$ is the ToU energy price (\$/kWh) over time, ν is the service fee in \$/kW for peak net load measured during the billing period, and $\bullet^\top$ denotes a vector's transpose. We use a time-step $\Delta t = 15$ minutes (0.25 hours), and $n = 96$ (1 day). For this problem we assume that the net-load is always greater than zero. The total baseline electrical bill for this day is \$52,080 (\$50,000 demand, \$2,080 energy). With the addition of a BESS that can supply $(-)$, or absorb $(+)$, power $\mathbf{p}$, the customer's total bill can be modified to:

$$f_s(\mathbf{p}) = \Delta t\, \mathbf{w}^\top(\mathbf{l} + \mathbf{p}) + \max(\mathbf{l} + \mathbf{p})\, \nu \tag{4}$$

where $\mathbf{p}$ is the battery system power that element wise subtracts from $\mathbf{l}$ when the battery system is discharging. The problem formulation can be expressed as: design an optimal battery dispatch control scheme that minimizes the customer's total bill subject to the constraints of the battery and the customer's system. The dispatch is open-loop, and we do not consider modeling uncertainty in this control scheme. Hence, we do not consider the mismatch between the controller model and a real system. Research into the effects of modeling uncertainty on BESS controller performance is ongoing [16].

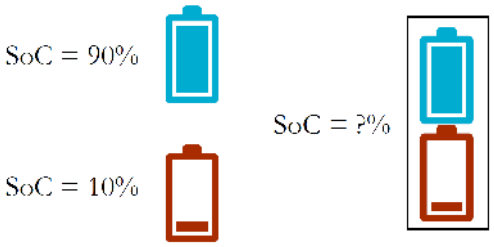

FIGURE 4. Thought experiment demonstrating how the electrochemical definition of the SoC of a battery loses physical meaning when applied to strings [17].

III. STATE-OF-CHARGE MODELS

Electrochemically, a battery cell's SoC is related to the concentration of the limiting active species, in the relevant reaction at the associated electrode [17]. This physical association however, breaks down when the electrochemical definition of SoC is applied to strings as the thought experiment in Fig. 4 illustrates. When referring to BESS, it is more common to use an empirical definition of SoC, represented in:

$$\text{State of Charge} \triangleq \frac{\text{Available Capacity}}{\text{Nominal Capacity}} \tag{5}$$

which is the ratio of available to nominal capacity. Normalizing SoC to the range [0,1] or [0%,100%] is an intuitive simplification, especially as nominal capacity can change over time, but it is not mathematically necessary to do so. In this context, capacity can be measured in energy with units of kilowatt-hours (kWh), charge with units of ampere-hours (Ah) or in concentration with units of moles-per-liter (mol/L). Constraints on SoC are shown in:

$$\varsigma_{\min} \le \varsigma \le \varsigma_{\max} \tag{6}$$

where ς is the SoC, $\varsigma_{\max}$ is the maximum SoC, and $\varsigma_{\min}$ is the minimum SoC. These box constraints are often enforced by a controller to ensure safety and design life, but many alternative methods for incorporating degradation into optimal control are discussed in Section V. Note that a BMS can also prevent overcharge/overdischarge by constraining SoC, but these bounds are generally set at or outside the normal operational range the controller uses.

Modeling SoC helps the controller know when in the future it is likely to encounter these limits and to make control decisions accordingly. In optimal control, SoC models inform the controller how control decisions affect future SoC and enable the controller to adjust decisions to optimize an objective. Therefore, errors in SoC models can lead to poor control performance or even infeasible solutions.

The various models for SoC can be classified by the units with which they define nominal and available capacity according to (5). Models that define capacity in units of energy (kWh) can be classified as energy reservoir models (ERMs), those which define it in units of charge (Ah) can be classified as charge reservoir models (CRMs), and those which define it in units of concentration (mol/L) can be classified as concentration-based models. ERMs, discussed in Section III-A, do not include dc voltage or current, so they generally have fewer variables and constraints. This simplification can lead to unrepresented physical dynamics that can, under some circumstances, have negative effects. CRMs, discussed in Section III-B, include expressions to represent current-voltage (I-V) dynamics which can improve accuracy at the expense of increased model complexity. Concentration based models, discussed in Section III-C, include many parameters associated with the specific electrochemical reaction and cell design that can predict battery dynamics. Each has its appropriate applications in control design as well as difficulties and drawbacks. Table 2 shows a summary of these trade-offs as discussed in detail in the following subsections.

A. ENERGY RESERVOIR MODELS

ERMs are a class of SoC model that define capacity in units of energy (kWh). An example ERM for SoC is shown in:

$$Q_{\text{cap}} \frac{\partial \varsigma}{\partial t} = \eta_e p^+ + p^- \tag{7}$$

where ς is the SoC, p^+ and p^- are the charge and discharge ac power respectively, Q_{cap} is the energy capacity, η_e is the round trip energy efficiency, and $\partial\varsigma/\partial t$ represents the rate of change of SoC. To make this constraint convex, charge power and discharge power are formulated as independent decision variables. While this means that simultaneous charge and discharge would not violate the explicit constraints, the objective function is often structured such that there is no advantage to candidate solutions that do so. Hence, as long as energy prices are positive, and efficiency is in the range [0, 1], the optimal solution to a control problem with this SoC constraint will always satisfy complementary slackness between

TABLE 2. Summary of SoC models.

Model Type	Measurable Variables	Calculated Variables	Parameters	Advantages	Disadvantages	References
ERM: no efficiency losses or self-discharge	p, q	ς	Q_{cap}, $\varsigma_{\max}$, $\varsigma_{\min}$, $p_{\max}$, $p_{\min}$, $S_{\max}$, p.f.$_{\min}$	convex constraints, lowest computational burden	assumes extremely narrow operational conditions	[7], [18]–[23]
ERM: with linear efficiency losses, self-discharge, and kinetic-model constraints	p, q	ς	Q_{cap}, η_{e}, p_{sd}, $\varsigma_{\max}$, $\varsigma_{\min}$, $p_{\max}$, $p_{\min}$, m_1, b_1, m_2, b_2, $S_{\max}$, p.f.$_{\min}$	convex constraints, simple to parameterize	inaccurate when operated over a range of voltage, current, or SoC	Without kinetic-model: [6], [24]–[35]. With kinetic-model: [36], [37]
ERM: nonlinear	p, q	ς	$Q_{\text{cap}}(\varsigma, T)$, $\eta_{\text{e}}(\varsigma, T)$, $p_{\text{sd}}(\varsigma, T)$, $\varsigma_{\max}$, $\varsigma_{\min}$, $p_{\max}$, $p_{\min}$, m_1, b_1, m_2, b_2, $S_{\max}$, p.f.$_{\min}$	potential for higher accuracy depending on accuracy of nonlinear functions	nonlinear models increase complexity and computational burden	[38]–[40]
CRM: no dynamic voltages	p, q, p_{dc}, i_{bat}, v_{bat}	v_{oc}, ς	$p_{\text{dc}}(p)$*, C_{cap}, η_{c}, i_{sd}, $v_{\text{oc}}(\varsigma)$*, R_0, $\varsigma_{\max}$, $\varsigma_{\min}$, $p_{\max}$, $p_{\min}$, $i_{\max}$, $i_{\min}$, $v_{\max}$, $v_{\min}$, $S_{\max}$, p.f.$_{\min}$	high accuracy for low sample rate, long duration model forecast	nonlinear models increase complexity and computational burden	[41]–[47]
CRM: with dynamic voltages	p, q, p_{dc}, i_{bat}, v_{bat}	v_{oc}, v_1, v_2, ς	$p_{\text{dc}}(p)$*, C_{cap}, η_{c}, i_{sd}, $v_{\text{oc}}(\varsigma)$*, R_0, R_1, C_1, R_2, C_2, $\varsigma_{\max}$, $\varsigma_{\min}$, $p_{\max}$, $p_{\min}$, $i_{\max}$, $i_{\min}$, $v_{\max}$, $v_{\min}$, $S_{\max}$, p.f.$_{\min}$	good accuracy for high sample rate, long duration model forecasts	high complexity and computational burden	[4], [5], [48]–[52]
SPM	p, q, p_{dc}, i_{bat}, v_{bat}	v_{oc}, $x_{s,p,\text{surf}}$, $x_{s,n,\text{surf}}$, ς	$p_{\text{dc}}(p)$*, $\Phi_p\left(x_{s,p,\text{surf}}\right)$*, $\Phi_n\left(x_{s,n,\text{surf}}\right)$*, $\varsigma_{\max}$, $\varsigma_{\min}$, $p_{\max}$, $p_{\min}$, $i_{\max}$, $i_{\min}$, $v_{\max}$, $v_{\min}$, $S_{\max}$, p.f.$_{\min}$	good accuracy for high sample rate, long duration model forecasts, enables physical degradation models	difficult to parameterize, much more computationally complex than the CRM.	[46], [53]–[56]
P2D	p, q, p_{dc}, i_{bat}, v_{bat}	v_{oc}, v_1, v_2, ς	$p_{\text{dc}}(p)$*, C_{cap}, η_{c}, i_{sd}, $v_{\text{oc}}(\varsigma)$*, R_0, R_1, C_1, R_2, C_2, $\varsigma_{\max}$, $\varsigma_{\min}$, $p_{\max}$, $p_{\min}$, $i_{\max}$, $i_{\min}$, $v_{\max}$, $v_{\min}$, $S_{\max}$, p.f.$_{\min}$	similar to SPM but more accurate at high currents.	highest complexity and computational burden, may need simplifying assumptions for use in control	[10], [54], [57], [58]

* Functions such as $p_{\text{dc}}(p)$ and $v_{\text{oc}}(\varsigma)$ each have many variations. The accuracy of these functions has a significant impact on the overall model's accuracy and should be chosen to closely approximate the state variable.

charge and discharge power. When objective does not have these properties, an additional non-convex constraint can be added to prevent solutions with simultaneous charge and discharge ($p^+p^- = 0$).

Rather than a constant, as shown in (7), the energy efficiency of a BESS can be a time-varying, nonlinear function of battery SoC, voltage, current, temperature, and state-of-health (SoH). Assuming a constant energy efficiency can, by extension, be an implicit assumption these states are also constant. Some of these assumptions are valid for a range of applications. SoH, for instance, changes very slowly with respect to a control horizon. Other assumptions however, are only valid for a narrow operational range. How wide the operational range can be, while the ERM remains a sufficiently accurate approximation, depends on how flat the energy efficiency curve is with respect to each variable. For example, changing battery voltage can change BESS efficiency but some battery types have a wide range of SoC where the open-circuit-voltage is nearly constant. ERMs are more accurate over a wider range of SoC for these types of batteries than for a battery whose open-circuit-voltage changes quickly with respect to SoC. ERMs use a simple representation of SoC that is based on many assumptions, so it may or may not be appropriate for a given application.

Some previous work using ERM ignore efficiency losses entirely [7], [18], [20]–[22]. However, due to the error it incurs, this is ill-advised for controllers that schedule SoC over any significant time horizon. Much work includes both charge and discharge efficiencies [6], [23]–[25], [27]–[32]. Self-discharge power can also be included in an ERM [6], [25], [27], [31]–[34] as shown in:

$$Q_{\text{cap}} \frac{\partial \varsigma}{\partial t} = \eta_{\text{e}} p^+ + p^- + p_{\text{sd}} \tag{8}$$

where p_{sd} is the self-discharge power.

We refer to (8) as a Type 1 model, in that it only includes charge efficiency. Models that include both charge and discharge efficiencies are referred to as Type 2 models, while those that only include discharge efficiency are referred to as Type 3 models. These model types are able to produce equivalent relationships between power and the rate of change in SoC over time. Table 3 shows the conversion calculations needed to move from one type to another while maintaining this equivalence. We use a Type 1 model in this paper (with

TABLE 3. Conversion between equivalent efficiency representations.

Type 1 $Q_{\text{cap}}^{(1)} \frac{\partial \varsigma}{\partial t} = \eta_{\text{cha}}^{(1)} p^+ + p^- + p_{\text{sd}}^{(1)}$

Type 2 $Q_{\text{cap}}^{(2)} \frac{\partial \varsigma}{\partial t} = \eta_{\text{cha}}^{(2)} p^+ + \frac{1}{\eta_{\text{dis}}^{(2)}} p^- + p_{\text{sd}}^{(2)}$

Type 3 $Q_{\text{cap}}^{(3)} \frac{\partial \varsigma}{\partial t} = p^+ + \frac{1}{\eta_{\text{dis}}^{(3)}} p^- + p_{\text{sd}}^{(3)}$

	To Type 1	**To Type 2**	**To Type 3**
From Type 1	$Q_{\text{cap}}^{(1)}$ $\eta_{\text{dis}}^{(1)}$ $p_{\text{sd}}^{(1)}$	$Q_{\text{cap}}^{(2)} = \frac{Q_{\text{cap}}^{(1)}}{\sqrt{\eta_{\text{cha}}^{(1)}}}$ $\eta_{\text{cha}}^{(2)} = \sqrt{\eta_{\text{cha}}^{(1)}}$ $\eta_{\text{dis}}^{(2)} = \sqrt{\eta_{\text{cha}}^{(1)}}$ $p_{\text{sd}}^{(2)} = \frac{p_{\text{sd}}^{(1)}}{\sqrt{\eta_{\text{cha}}^{(1)}}}$	$Q_{\text{cap}}^{(3)} = \frac{Q_{\text{cap}}^{(1)}}{\eta_{\text{cha}}^{(1)}}$ $\eta_{\text{dis}}^{(3)} = \eta_{\text{cha}}^{(1)}$ $p_{\text{sd}}^{(3)} = \frac{p_{\text{sd}}^{(1)}}{\eta_{\text{cha}}^{(1)}}$
From Type 2	$Q_{\text{cap}}^{(1)} = Q_{\text{cap}}^{(2)} \eta_{\text{dis}}^{(2)}$ $\eta_{\text{cha}}^{(1)} = \eta_{\text{cha}}^{(2)} \eta_{\text{dis}}^{(2)}$ $p_{\text{sd}}^{(1)} = p_{\text{sd}}^{(2)} \eta_{\text{dis}}^{(2)}$	$Q_{\text{cap}}^{(2)}$ $\eta_{\text{cha}}^{(2)}$ $\eta_{\text{dis}}^{(2)}$ $p_{\text{sd}}^{(2)}$	$Q_{\text{cap}}^{(3)} = \frac{Q_{\text{cap}}^{(2)}}{\eta_{\text{cha}}^{(2)}}$ $\eta_{\text{dis}}^{(3)} = \eta_{\text{cha}}^{(2)} \eta_{\text{dis}}^{(2)}$ $p_{\text{sd}}^{(3)} = \frac{p_{\text{sd}}^{(2)}}{\eta_{\text{cha}}^{(2)}}$
From Type 3	$Q_{\text{cap}}^{(1)} = Q_{\text{cap}}^{(3)} \eta_{\text{dis}}^{(3)}$ $\eta_{\text{cha}}^{(1)} = \eta_{\text{dis}}^{(3)}$ $p_{\text{sd}}^{(1)} = p_{\text{sd}}^{(3)} \eta_{\text{dis}}^{(3)}$	$Q_{\text{cap}}^{(2)} = Q_{\text{cap}}^{(3)} \sqrt{\eta_{\text{dis}}^{(3)}}$ $\eta_{\text{cha}}^{(2)} = \sqrt{\eta_{\text{dis}}^{(3)}}$ $\eta_{\text{dis}}^{(2)} = \sqrt{\eta_{\text{dis}}^{(3)}}$ $p_{\text{sd}}^{(2)} = p_{\text{sd}}^{(3)} \sqrt{\eta_{\text{dis}}^{(3)}}$	$Q_{\text{cap}}^{(3)}$ $\eta_{\text{dis}}^{(3)}$ $p_{\text{sd}}^{(3)}$

This conversion table applies equally to the ERM and CRM. For the CRM, replace variables p^+ and p^- with i_{bat}^+ and i_{bat}^- and parameters Q_{cap} and p_{sd} with C_{cap} and i_{sd} respectively.

$\eta_{\text{cha}} = \eta_{\text{e}}$ the round trip energy-efficiency) because it has the intuitive property that the SoC multiplied by the capacity directly reflects how much energy is expected to be available from the battery on discharge.

While most ERM use ac power, a few use dc power [59] by including many of the constraints in the CRM. The manufacturer dc kWh rating for batteries is calculated based on either the Ah rating multiplied by the nominal battery voltage or the energy extracted during a constant current discharge test. Hence, this approach is still subject to the inaccuracy of other ERM, over a wide operational range, if voltage is far from the nominal voltage assumed or the constant current rate used during testing.

Though it is not commonly done, all three parameters can be functions of the SoC or temperature or both ($Q_{\text{cap}}(\varsigma, T)$, $\eta_{\text{e}}(\varsigma, T)$, and $p_{\text{sd}}(\varsigma, T)$) [38]–[40]. The most common version of this is SoC dependent losses $p_{\text{sd}}(\varsigma) = m_{\text{sd}}\varsigma + b_{\text{sd}}$ where m_{sd} is the proportional power loss and b_{sd} is the power loss at $\varsigma = 0$ [23], [26]. Adding nonlinearity to these functions has the potential to increase predictive accuracy over a wider operational range of SoC and warrants further investigation [38].

To represent the relationship between SoC and the power limits (p_{max} and p_{min}) a two reservoir ERM, also called the kinetic battery model, is sometimes used [36], [37]. The

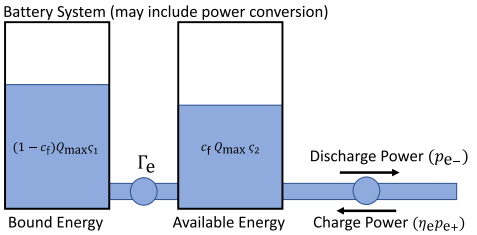

FIGURE 5. Energy Based Kinetic Battery Model [36].

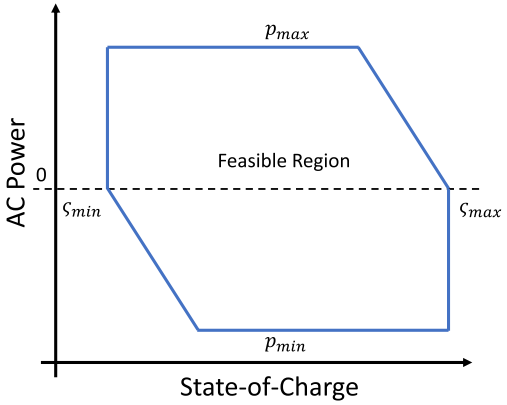

FIGURE 6. Feasible region for ac power described by the kinetic battery model.

kinetic battery model splits the reservoir into available energy and bound energy as shown in Fig. 5 and in:

$$(1 - c_{\text{f}})Q_{\text{cap}} \frac{\partial \varsigma_1}{\partial t} = \Gamma_{\text{e}}(\varsigma_2 - \varsigma_1) \tag{9a}$$

$$c_{\text{f}}\, Q_{\text{cap}} \frac{\partial \varsigma_2}{\partial t} = \eta_{\text{e}} p^+ + p^- + \Gamma_{\text{e}}(\varsigma_1 - \varsigma_2) \tag{9b}$$

where c_{f} is the fraction of total capacity in the available reservoir, and Γ_{e} is a time constant that governs the rate of energy transfer between the two reservoirs. The physical intuition of this model is that the higher the discharge rate the more quickly the available energy is depleted, and the low-level limit of the tank is reached. This is equivalent to the linear inequality constraints on power in:

$$p_{\text{min}} \leq p \leq p_{\text{max}} \tag{10a}$$

$$m_1 \varsigma + b_1 \leq p \leq m_2 \varsigma + b_2 \tag{10b}$$

where p_{min} is the discharge power limit, p_{max} is the charge power limit, m_1 and b_1 are the slope and intercept of the linear power limit on discharge, respectively, and m_2 and b_2 are the slope and intercept of the linear power limit on charge, respectively. These constraints are encountered at high discharge rate more quickly according to the slope m_1 and intercept b_1. These constraints then reduce maximum power linearly as SoC approaches its minimum, the same as if the maximum power is constrained by the difference between tank levels in the kinetic battery model. The limits defined in (10) are shown in Fig. 6

Injection and absorption of reactive power can be an important capability for BESS in many applications [1]. While

reactive power does not directly affect SoC, it can indirectly affect SoC by constraining real power. Constraints on apparent power and power factor are presented in [28]:

$$p = p^+ + p^- \tag{11a}$$
$$p^2 + q^2 \leq S_{\max}^2 \tag{11b}$$
$$\left| \frac{p}{\sqrt{p^2+q^2}} \right| \geq \text{p.f.}_{\min} \tag{11c}$$

where q is the reactive power (var), $S_{\max}$ is the apparent power limit, and $\text{p.f.}_{\min}$ is the minimum power factor. While there are no direct incentives for reactive power, there might be penalties on poor power factors. Therefore in many cases, constraint 11 must be enforced.

TABLE 4. Energy reservoir model parameters.

Name	Symbol	Value
Energy Capacity	Q_{cap}	600 kWh
Energy Efficiency	η_{e}	65%
Self-Discharge Power	p_{sd}	-7 kW
Maximum Discharge Power	$p_{\max}$	500 kW
Maximum Charge Power	$p_{\min}$	-500 kW
Maximum SoC	$\varsigma_{\max}$	95%
Initial SoC	ς_0	60%
Minimum SoC	$\varsigma_{\min}$	20%
Kinetic model discharge slope	m_1	$p_{\min}$ / 10% *
Kinetic model discharge intercept	b_1	-$\varsigma_{\min} \times m_1$ *
Kinetic model charge slope	m_2	-$p_{\max}$ / 5% *
Kinetic model charge intercept	b_2	-$\varsigma_{\max} \times m_2$ *

Note: these model parameters are meant to represent a typical battery system and do not necessarily reflect any specific equipment.
* These slope and intercept values are written in terms of the power and SoC limits above. The value -$p_{\max}$ / 10% indicates that the charge limit will be imposed over an SoC band of 10%, while -$\varsigma_{\min} \times m_1$ calculates a y-intercept that makes the power limit = 0 at $\varsigma = \varsigma_{\min}$.

1) ERM APPLICATION

In this section we solve the problem outlined in Section II with an optimal controller designed using an ERM. The ERM is used here to demonstrate its application, however, it is not the most appropriate model for this problem because of its inaccuracy over a wide range of voltage in this scenario. In cases where the performance of the ERM model is less than desirable, it is sometimes employed because of the computational simplicity. The example scenario listed here serves to demonstrate how the ERM can be applied to solve a simple problem, and one can extrapolate it to how it could be used to solve a more complicated problem. Example parameters for the ERM are listed in Table 4.

We can express the constraint described in (8) between each SoC using the vector equation (12).

$$Q_{\text{cap}}\mathbf{D}\boldsymbol{\varsigma} = \eta_{\text{e}}\mathbf{p}^+ + \mathbf{p}^- + p_{\text{sd}}[\mathbf{1}] \tag{12}$$

where $\boldsymbol{\varsigma} \in \mathbb{R}^{n+1}$ is the SoC at each time step, $\mathbf{p}^+ \in \mathbb{R}_+^n$ and $\mathbf{p}^- \in \mathbb{R}_-^n$ are the ac charge and discharge power during each time step, and the matrix $\mathbf{D}$ is defined below.

$$\mathbf{D} = \frac{1}{\Delta t}\begin{bmatrix} -1 & 1 & 0 & . & . & 0 \\ 0 & -1 & 1 & 0 & . & . \\ & & . & . & & \\ & & & . & . & \\ 0 & & & 0 & -1 & 1 \end{bmatrix}_{n\times(n+1)} \tag{13}$$

The SoC constraint in (12) can be included with the kinetic battery model constraints in (10) yielding the problem formulation in:

$$\min_{\mathbf{x}_{\text{ERM}} \in \mathbb{R}^{3n+2}} \ \Delta t \mathbf{w}^\top(\mathbf{l} + \mathbf{p}^+ + \mathbf{p}^-) + \nu\tau \tag{14a}$$
subject to: $Q_{\text{cap}}\mathbf{D}\boldsymbol{\varsigma} = \eta_{\text{e}}\mathbf{p}^+ + \mathbf{p}^- + p_{\text{sd}}[\mathbf{1}]$
$$\boldsymbol{\varsigma}_{[1]} = \varsigma_0 \tag{14b}$$
$$\boldsymbol{\varsigma}_{[1]} = \boldsymbol{\varsigma}_{[n]} \tag{14c}$$
$$p_{\min}[\mathbf{1}] \leq \mathbf{p}^+ + \mathbf{p}^- \leq p_{\max}[\mathbf{1}] \tag{14d}$$
$$\varsigma_{\min}[\mathbf{1}] \leq \boldsymbol{\varsigma} \leq \varsigma_{\max}[\mathbf{1}] \tag{14e}$$
$$m_1\boldsymbol{\varsigma} + b_1[\mathbf{1}] \leq \mathbf{p}^+ + \mathbf{p}^- \leq m_2\boldsymbol{\varsigma} + b_2[\mathbf{1}] \tag{14f}$$
$$\mathbf{l} + \mathbf{p}^+ + \mathbf{p}^- \leq \tau[\mathbf{1}] \tag{14g}$$

where $\mathbf{x}_{\text{ERM}} = \{\mathbf{p}^+, \mathbf{p}^-, \boldsymbol{\varsigma}, \tau\} \in \mathbb{R}^{3n+2}$, and $\tau \in \mathbb{R}$ is a dummy variable that represents the peak net load. The constraint (14b) ensures that control decisions are made based on the current estimated SoC. The constraint (14c) represents the intuitive assumption that the BESS will continue to operate after the end of the current control horizon and that the next period will be similar to this one. In this application, (14c) is used to make simulation results easier to interpret and compare. The objective has been modified to use the dummy variable τ to represent peak load in the objective and add a constraint that it be greater than the net load at every time (14g).

In the code accompanying this article the minimum heat generation regularization term, described in Section V-A.1 ($\Pi||\mathbf{p}^+ + \mathbf{p}^-||_2^2$, with a very small weight Π = 1e-5), is applied to the objective in this and each application script. This has the effect of avoiding spikes or abrupt changes in power, while not significantly impacting the minimum value achieved.

Information on numerical algorithms for solving general linear and nonlinear optimization problems can be found in [60], [61]. We solve this using the Pyomo optimization modeling language [62], [63] and the Ipopt interior point optimization problem solver [64]. The solution is shown in Fig. 7. Note that even though the maximum discharge power is 500 kW, the battery is only able to reduce the peak net load by approximately 85 kW because of limitations on energy. The effect of the kinetic battery model can be observed around hour 10, when the battery finishes charging then pauses for one time step only to then charge at a low level to maintain 94.8% SoC. This artifact of the model is because the maximum charge rate at 95% SoC is 0 kW which

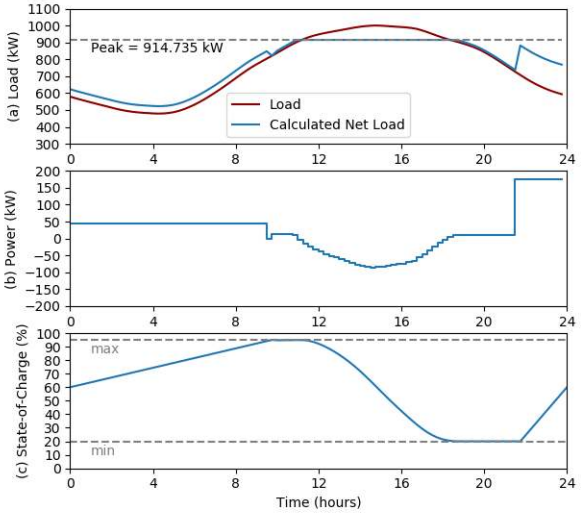

FIGURE 7. Results calculated with the ERM: (a) Net load with BESS power control, (b) Battery power, (c) Battery SoC (bottom).

is insufficient to counter self-discharge power. The ERM expects to be able to reduce the peak to 914.7 kW and it is clear from the calculated net load the schedule allocates charging to the periods of low electricity price.

The control solution reduces the total electrical bill from \$52,080 (\$50,000 demand, \$2,080 energy) to \$47,837 (\$45,737 demand, \$2101 energy). The net effect is a \$4,243, or 8.15%, reduction in the electrical bill. Note that while the demand charge is reduced significantly, the energy bill increases due to efficiency losses in the BESS.

B. CHARGE RESERVOIR MODEL (CRM)

CRMs are a class of BESS models that define capacity in units of charge (Ah). An example CRM is shown in:

$$C_{\text{cap}} \frac{\partial \varsigma}{\partial t} = \eta_{\text{c}} i_{\text{bat}}^{+} + i_{\text{bat}}^{-} \tag{15}$$

where i_{bat}^{+} and i_{bat}^{-} are the charge and discharge current respectively, ς is the battery SoC, C_{cap} is the charge capacity, η_{c} is the coulombic efficiency, and $\partial\varsigma/\partial t$ represents the rate of change of SoC. Like with the ERM, to make this constraint convex, charge current and discharge current are formulated as independent decision variables. Simultaneous charge and discharge is avoided in the same way, by structuring the objective function such that there is no advantage to those candidate solutions.

Peukert's equation relates the charge capacity to the discharge rate in amps [65], [66]:

$$C_{\text{cap}} = (i_{\text{bat}}^{-})^{k_{\text{peu}}} t_{\text{discharge}} \tag{16}$$

where k_{peu} is the Peukert exponent, and t_{peu} discharge time before the battery reaches its low voltage limit. Peukert's equation is sometimes used in control design [67]. However, it makes several simplifying assumptions that do not make sense for optimal control applications. The parameters of Peukert's equation assume a constant-current discharge, where 0% SoC corresponds to battery reaching its minimum voltage under load. This model implies a battery equivalent circuit, that is better to represent explicitly, and a static operating condition (constant-current discharge) that is one of the decision variables in our problem formulation.

While some previous work ignore efficiency losses [41]–[45], this many not be accurate for controllers that predict SoC over an extended time horizon for the same reason as discussed in Section III-A. Self-discharge current can be included in a CRM [42], [52], [68] as in:

$$C_{\text{cap}} \frac{\partial \varsigma}{\partial t} = \eta_{\text{c}} i_{\text{bat}}^{+} + i_{\text{bat}}^{-} + i_{\text{sd}} \tag{17}$$

where i_{sd} is the self-discharge current. While less common for CRM, efficiency in this model can be represented equivalently with Type 2 and Type 3 models as shown in Table 3.

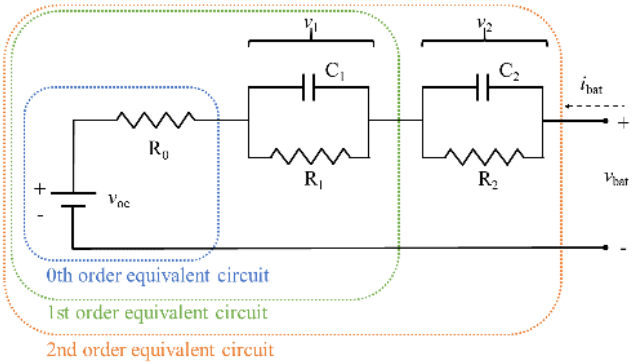

FIGURE 8. Equivalent Circuit Models.

Several additional constraints are needed to govern internal relationships between voltage, current, dc power, and ac power. The foundation of these is an equivalent circuit model [49], [50], [69], [70]. The most common battery equivalent circuit models are shown in Fig. 8 and described in:

$$i_{\text{bat}} = i_{\text{bat}}^{+} + i_{\text{bat}}^{-} \tag{18a}$$

$$\frac{\partial v_1}{\partial t} = \frac{-1}{R_1 C_1} v_1 + \frac{1}{C_1} i_{\text{bat}} \tag{18b}$$

$$\frac{\partial v_2}{\partial t} = \frac{-1}{R_2 C_2} v_2 + \frac{1}{C_2} i_{\text{bat}} \tag{18c}$$

$$v_{\text{oc}} + R_0 i_{\text{bat}} + v_1 + v_2 = v_{\text{bat}} \tag{18d}$$

where R_0, R_1, C_1, R_2, and C_2 are equivalent circuit resistor and capacitor parameters. The 0^{th} order equivalent circuit is accurate for steady state analysis as it accounts for battery ohmic resistance R_0 but not any time-domain dynamic response. The 1^{st} and 2^{nd} order models are increasingly accurate for analyses requiring short time steps (roughly faster than 10 minutes between samples or (1/600)Hz) [48]. The R-C parallel elements of the circuit can represent different chemical reaction dynamics within battery cells: R_1 & C_1 can represent ion-diffusion (Warburg impedance) whereas R_2 & C_2 can represent anode-cathode capacitance or constant phase element [69]. Note that the time

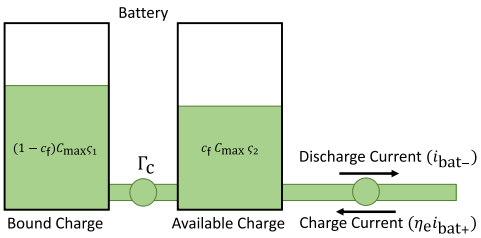

FIGURE 9. Charge Based Kinetic Battery Model [72], [73].

constant of the diffusion element ($\tau_1 = R_1C_1$) is generally much larger than the time constant of the capacitance element ($\tau_2 = R_2C_2$). The equivalent circuit's impedance parameters can be calculated using least squares system identification [71]. These parameters can be functions of current, SoC, SoH, temperature, or any combination thereof [52].

There are many variations of these equivalent circuits. Adding a resistor across the voltage source is equivalent to making i_{sd} a linear function of v_{oc}. Adding a resistor across the battery terminals is equivalent to making i_{sd} a linear function of v_{bat}. Several other configurations are discussed in [48], but it is unclear how these additions affect the accuracy of the model.

Though it is rare to do so in a controller, battery voltage hysteresis can be incorporated into the equivalent circuit model [17] as shown in:

$$\frac{\partial v_{hys}}{\partial t} = \gamma_{hys}\,\mathrm{sgn}(i_{bat})\,(M(\varsigma, i_{bat}) - v_{hys}) \tag{19}$$

where v_{hys} is the dynamic voltage hysteresis, γ_{hys} is a decay rate tuning constant, and $M : \mathbb{R}^2 \mapsto \mathbb{R}$ is a function that returns the maximum voltage hysteresis. Specifically, $M(\varsigma, i_{bat})$ is an empirical approximation based on experimental data that is positive for charge and negative for discharge. Alternatively, the hysteresis can be modeled using an additional charge reservoir as in [72], [73]. This approach splits the total charge capacity into two states: bound charge, and available charge as shown in Fig. 9 and in:

$$(1-c_f)C_{cap}\frac{\partial \varsigma_1}{\partial t} = \Gamma_c(\varsigma_2 - \varsigma_1) \tag{20a}$$

$$c_f\,C_{cap}\frac{\partial \varsigma_2}{\partial t} = \eta_c i_{bat}^{+} + i_{bat}^{-} + \Gamma_c(\varsigma_1 - \varsigma_2) \tag{20b}$$

where c_f is the fraction of total capacity in the available reservoir, and Γ_c is a time constant that governs the rate of charge transfer between the two reservoirs. The open-circuit-voltage is then based on the available charge level only. This effectively represents energy recovery effect and is structurally similar to the discrete version of the single particle model discussed in Section III-C.

Open-circuit-voltage v_{oc}, also referred to as electromotive potential or force, is the terminal voltage of the battery when measured 'at-rest' and is a function of the SoC, SoH and temperature of the cell. Several example functions for v_{oc} are given in:

$$v_{oc} = v_m\varsigma + v_0 \tag{21a}$$

$$v_{oc} = k_T(T - T_{ref})(m\varsigma + v_0) \tag{21b}$$

$$v_{oc} = a\varsigma^2 + b\varsigma + c \tag{21c}$$

$$v_{oc} = \alpha\varsigma^3 + \beta\varsigma^2 + \gamma\varsigma + \delta \tag{21d}$$

$$v_{oc} = b_k - m_k\frac{(1-\varsigma)}{\varsigma} + c_k e^{d_k\varsigma} \tag{21e}$$

$$v_{oc} = \alpha(\varsigma)\varsigma^3 + \beta(\varsigma)\varsigma^2 + \gamma(\varsigma)\varsigma + \delta(\varsigma) \tag{21f}$$

where v_m and v_0 are the slope and intercept of a linear v_{oc} model, respectively, k_T is a linear temperature adjustment, T and T_{ref} are the battery temperature and reference battery temperature, respectively, a, b, and c are the coefficients for a quadratic polynomial fit, α, β, γ, and δ are the coefficients for a cubic polynomial fit, b_k, m_k, c_k, and d_k are the coefficients for a negative reciprocal and exponential function fit, and $\alpha(\varsigma)$, $\beta(\varsigma)$, $\gamma(\varsigma)$, and $\delta(\varsigma)$ are piecewise functions that collectively comprise a cubic spline. The simplest function for v_{oc} is a linear approximation (21a) which can be accurate within a narrow range of SoC [4], [35], [50], [74]. A temperature adjustment can also be applied (21b) to improve accuracy [50], [68]. Polynomial approximations are also used, (21c) or (21d), but these are sometimes non-convex and so can be more computationally intensive to work with. Another approach is to model v_{oc} as a combination of a negative reciprocal and exponential functions (21e) [75], [76]. This model works better for lithium-cobalt batteries or other chemistries with exponential curves near 100% and 0% SoC but that are relatively flat and straight in a wide range around 50% SoC. Note that (21e) has an asymptote at $\varsigma = 0$, and hence the model must constrain SoC to some positive threshold to work well. Piecewise cubic splines (21f) are the most accurate [48], but these can be very difficult functions to work with in optimization. Example open-circuit-voltage data along with different fit types are shown in Fig. 10. Battery voltage hysteresis can alternatively be represented within the open-circuit-voltage function by modeling v_{oc} differently on charge and discharge [75].

Battery power is modeled through Ohm's power law:

$$p_{dc} = i_{bat}v_{bat} \tag{22}$$

where p_{dc} is the dc power.

The conversion efficiency from ac to dc power, or vice versa, is sometimes ignored. When it is modeled, conversion efficiency is commonly modeled as a constant [28]. One way of modeling inverter efficiency as a constant is shown in:

$$p_{dc} = \phi_e p^{+} + \frac{1}{\phi_e}p^{-} \tag{23}$$

where $\phi_e \in [0, 1]$ is the conversion efficiency constant. Alternatively, a linear fit or quadratic fit can be used [77]:

$$p_{dc} = \phi_m p + \phi_b \tag{24}$$

$$p_{dc} = \phi_0 p^2 + \phi_1 p + \phi_2 \tag{25}$$

where ϕ_m and ϕ_b are the slope and intercept of a linear efficiency function, respectively, and ϕ_0, ϕ_1, and ϕ_2 are the

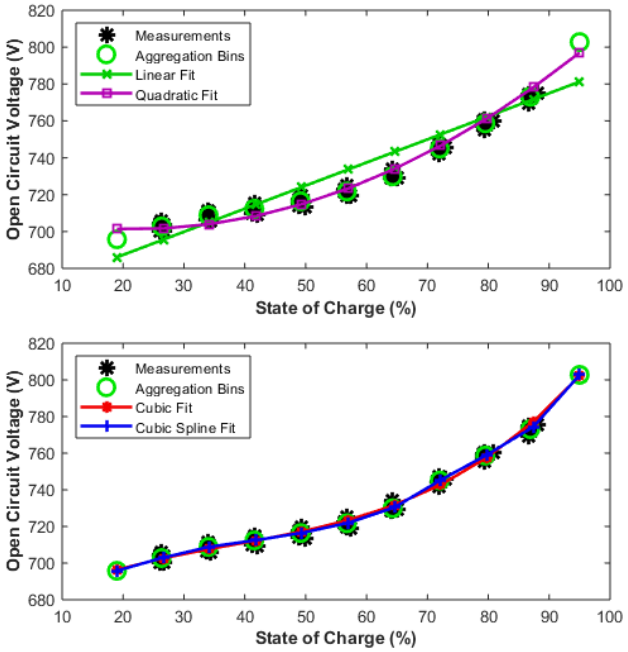

FIGURE 10. Open-Circuit-Voltage Models.

coefficients of a quadratic efficiency function. Inverter efficiency can be a nonlinear function of ac voltage, dc voltage, and temperature [78].

While CRMs normally include box constraints on SoC and real/reactive power, additional box constraints on current and battery voltage are shown in:

$$i_{\min} \leq i_{\text{bat}} \leq i_{\max} \tag{26a}$$

$$v_{\min} \leq v_{\text{bat}} \leq v_{\max} \tag{26b}$$

Unlike the ERM, it is not necessary to add SoC dependent power constraints as the voltage constraints handle these limits implicitly.

An important factor to consider is that battery cells within a string may have significantly different parameters resulting from normal manufacturing variation. When using a CRM in a controller design, there are at least three methods for accounting for distributions in parameters and states within a BESS [69], [79]. What follows is a discussion of these methods and their relative advantages for optimal control.

"Big cell" method: This method is based on a simplification that models a battery pack as one large battery cell. In this approach, the battery voltage is the individual cell voltage multiplied by the number of cells in series, the capacity is the total capacity and so on. Intercell balancing is generally handled within the self-discharge current parameter. This method is most accurate when a string is made up of very well-matched cells, which are manufactured to have a very narrow distribution of performance. For poorly matched cells, or for cells that have degraded and hence have widened in their performance distribution, this approach is optimistic in its approximation of string capacity on both charge and discharge.

"Short board effect" method: This method uses models of the extreme cells in a string to better represent limiting factors. The maximum SoC cell and minimum SoC cell are tracked independently, each with their own decision variables and limits. The total string voltage is then the sum of the highest SoC cell voltage, the lowest SoC cell voltage, and the voltage of a "big cell" representing all remaining cells. This approach more accurately models when the string will encounter cell voltage or SoC limits. There is some increase in the computational complexity as there must be additional decision variable for voltage, dynamic voltage, and SoC as well as their associated constraint sets.

"One-by-one calculation" method: This method explicitly represents all cells in a battery pack. In cases where cells have a wide variance in capacity and coulombic efficiency, it is possible that the highest SoC cell and/or lowest SoC cell will switch cells within the control horizon. This method will be able to predict and optimize operation whichever cell is the limiting factor for a given cycle. Explicitly modeling every cell within a string also enables the direct representation of cell balancing circuits within the controller, as in [79], [80]. This also enables the representation of unequal current splitting in parallel cells or strings. With hundreds or even thousands of cells in a grid scale BESS, this approach can easily become computationally infeasible to apply in practice.

As CRMs account for changes in battery dynamics over the range of voltage and current, they are more accurate than ERMs in applications where the SoC and charge/discharge currents vary significantly. However, given the increase in complexity, they are much more difficult to use in the design of optimal controllers. Hence, CRMs are best used in applications relying on long duration, if sparse, charge/discharge schedules (e.g., day-ahead hourly energy arbitrage). In such applications the high rate battery dynamics in (18) can often be ignored.

1) CRM APPLICATION

In this section we solve the problem outlined in Section II with an optimal controller designed around a CRM. Example parameters for a CRM are listed in Table 5.

The 'CRM: no dynamic voltages' from Table 2 is the most appropriate model for this problem because of the long forecast horizon, low (15 minute) time resolution, and because we are only controlling one battery system. We also use the "big battery" approach to modeling the dc battery string. Implementing the CRM into a usable format requires reformulating the differential equation for SoC defined in (15) into the vector of equality constraints as shown in:

$$C_{\text{cap}}\mathbf{D}\boldsymbol{\varsigma} = \eta_c \mathbf{i}_{\text{bat}}^{+} + \mathbf{i}_{\text{bat}}^{-} \tag{27}$$

where $\boldsymbol{\varsigma} \in \mathbb{R}^{n+1}$ is the vector of SoC at each time step, $\mathbf{i}_{\text{bat}}^{+} \in \mathbb{R}_{+}^{n}$ and $\mathbf{i}_{\text{bat}}^{-} \in \mathbb{R}_{-}^{n}$ are the vectors of charge and discharge dc current respectively, and $\mathbf{D}$ is a matrix defined

TABLE 5. Battery system charge reservoir model parameters.

Name	Symbol	Value
Charge Capacity	C_{cap}	800 Ah
Coulombic Efficiency	η_{c}	94.6%
Self-Discharge Current	i_{sd}	0.50 A
Inverter Efficiency Coefficient	ϕ_0	-2.0503e-04
Inverter Efficiency Coefficient	ϕ_1	0.99531
Inverter Efficiency Coefficient	ϕ_2	-6.1631
Battery Internal Resistance	R_0	71.6 mΩ
Maximum Discharge Power	$p_{\min}$	-500 kW
Maximum Charge Power	$p_{\max}$	500 kW
Maximum SoC	$\varsigma_{\max}$	95%
Initial SoC	ς_0	60%
Minimum SoC	$\varsigma_{\min}$	20%
Minimum Battery Voltage	$v_{\min}$	680 V
Maximum Battery Voltage	$v_{\max}$	820 V
Maximum Current Discharge	$i_{\min}$	-1000 A
Maximum Current Charge	$i_{\max}$	1000 A

Cubic Polynomial Fit	α	β	γ	δ
$0.2 \leq \varsigma \leq 0.95$	320.377	-368.742	201.004	669.282

Note: these model parameters are meant to represent a representative battery system and do not necessarily reflect any specific equipment.

above in (13). Like with the ERM, charge current and discharge current are formulated as separate decision variables. While this does not make the optimization problem convex, it does improve the convergence time of the solver without affecting the solution. The resulting problem formulation is shown in:

$$\min_{\mathbf{x}_{\text{CRM}} \in \mathbb{R}^{6n+2}} \Delta t\, \mathbf{w}^{\top}(\mathbf{l}+\mathbf{p}) + \nu\tau \tag{28a}$$

$$\mathbf{p}_{\text{dc}} = \phi_0 \mathbf{p}^2 + \phi_1 \mathbf{p} + \phi_2 \tag{28b}$$

$$\mathbf{p}_{\text{dc}} = (\mathbf{i}^{+}_{\text{bat}} + \mathbf{i}^{-}_{\text{bat}})\mathbf{v}_{\text{bat}} \tag{28c}$$

$$\mathbf{v}_{\text{bat}} = \mathbf{v}_{oc[1:n]} + R_0(\mathbf{i}^{+}_{\text{bat}} + \mathbf{i}^{-}_{\text{bat}}) \tag{28d}$$

$$\mathbf{v}_{\text{oc}} = \alpha \boldsymbol{\varsigma}^3 + \beta \boldsymbol{\varsigma}^2 + \gamma \boldsymbol{\varsigma} + \delta \tag{28e}$$

$$C_{\text{cap}}\mathbf{D}\boldsymbol{\varsigma} = \eta_{\text{c}}\mathbf{i}^{+}_{\text{bat}} + \mathbf{i}^{-}_{\text{bat}} \tag{28f}$$

$$\boldsymbol{\varsigma}_{[1]} = \varsigma_0 \tag{28g}$$

$$\boldsymbol{\varsigma}_{[1]} = \boldsymbol{\varsigma}_{[n]} \tag{28h}$$

$$p_{\min}[\mathbf{1}] \leq \mathbf{p} \leq p_{\max}[\mathbf{1}] \tag{28i}$$

$$\varsigma_{\min}[\mathbf{1}] \leq \boldsymbol{\varsigma} \leq \varsigma_{\max}[\mathbf{1}] \tag{28j}$$

$$v_{\min}[\mathbf{1}] \leq \mathbf{v}_{\text{bat}} \leq v_{\max}[\mathbf{1}] \tag{28k}$$

$$i_{\min}[\mathbf{1}] \leq \mathbf{i}^{-}_{\text{bat}} \leq [\mathbf{0}] \tag{28l}$$

$$[\mathbf{0}] \leq \mathbf{i}^{+}_{\text{bat}} \leq i_{\max}[\mathbf{1}] \tag{28m}$$

$$\mathbf{l}+\mathbf{p} \leq \tau[\mathbf{1}] \tag{28n}$$

where $\mathbf{x}_{\text{CRM}} = \{\mathbf{p}, \mathbf{p}_{dc}, \mathbf{i}_{\text{bat}}, \mathbf{v}_{\text{bat}}, \mathbf{v}_{\text{oc}}, \boldsymbol{\varsigma}, \tau\} \in \mathbb{R}^{6n+2}$, $\mathbf{p}_{\text{dc}} \in \mathbb{R}^n$ is the dc electrical power provided to the battery, $\mathbf{v}_{\text{bat}} \in \mathbb{R}^n$ is the battery terminal voltage, $\mathbf{v}_{\text{oc}} \in \mathbb{R}^{n+1}$ is the battery open-circuit-voltage, and τ is the dummy variable for peak power. The CRM includes constraints on inverter conversion efficiency (28b), Ohm's law relating dc power, voltage and current (28c), the battery equivalent circuit model (28d), and the open-circuit-voltage curve (28e). The constraint (28g) ensures that control decisions are made based on the current estimated SoC. The constraint (28h) represents the intuitive assumption that the BESS will continue to operate after the end of the current control horizon and that the next period will be similar to this one. In this application, (28h) is used to make simulation results easier to interpret and compare. Again, while simultaneous charge and discharge does not violate explicit constants, the structure of the objective ensures that solutions will comply with complementary slackness between charge and discharge current.

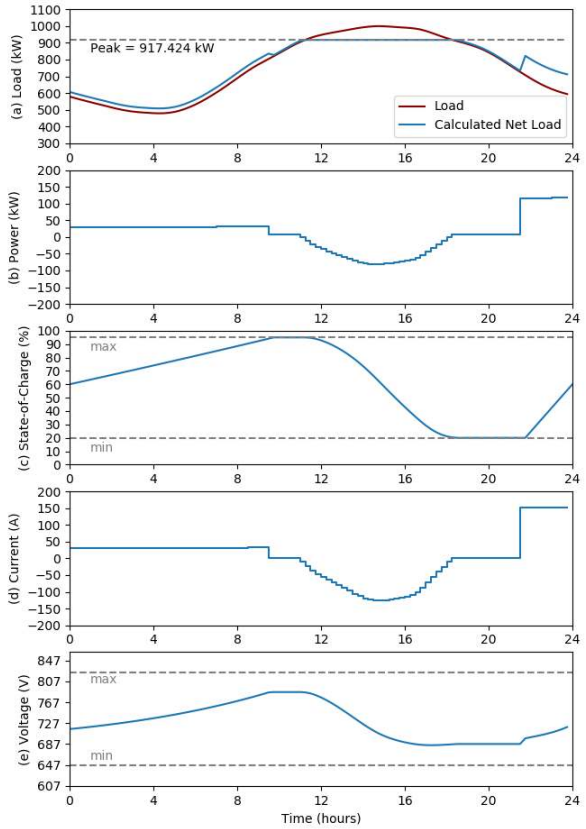

FIGURE 11. Results calculated with the CRM: (a) net load with BESS power control, (b) battery power, (c) battery SoC, (d) battery current, and (e) battery voltage.

The resulting customer's net load and optimal control schedule for the BESS are shown in Fig. 11 (a) and (b) respectively. The simulated battery current and voltage are shown in Fig. 11 (c) and (e) respectively. The CRM based controller expects to be able to reduce the peak load by approximately 83 kW. The peak battery voltage reached 780 V and the dc current reached −120 A on discharge. The control solution reduces the total electrical bill from $52,080 ($50,000 demand, $2,080 energy) to $47,948 ($45,871 demand, $2077 energy). The net effect is a $4,132, or 7.93%, reduction in the electrical bill.

If we assume that the example ERM and CRM represent the same physical BESS, then we can investigate which one is a better controller. We can observe that the ERM expects to be able to reduce the peak load, and the total bill, more than the CRM. If the ERM is the more accurate model, then the CRM will underutilize the batteries. However, if the CRM is

more accurate, as we expect it to be, then the control solution from the ERM controller may be infeasible.

C. CONCENTRATION BASED MODELS

Concentration based models measure capacity in units of the concentration (mol/L) of the active materials of the electrodes. These models can be further classified into single particle model (SPM), pseudo-two-dimensional model (P2D), and many others [12]. In this section we briefly cover SPM and P2D models as these are the concentration models most widely used in controllers. Note that concentration models may require parameters based on cell construction and chemistry that manufacturers consider proprietary and would not be available to the controller. However, there are methods available to estimate some or all of these parameters empirically [55], [58].

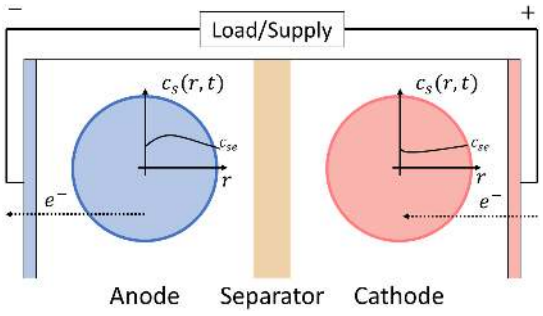

FIGURE 12. Single particle model (SPM).

SPMs represent each electrode as a single particle [54], [81]–[83] which is useful for modeling the effects of transport phenomena but loses some accuracy at high current, or wherever variations across the electrodes are significant [11], [84]. Figure 12 shows an simple generic SPM. The differential equation for mass balance in an intercalation particle is governed by Fick's law in a spherical coordinate system [85], [86]:

$$\frac{\partial c_{s,j}}{\partial t} = \frac{D_{s,j}}{r_j^2}\frac{\partial}{\partial r_j}\left(r_j^2\frac{\partial c_{s,j}}{\partial r_j}\right) \tag{29}$$

where $c_{s,j}$ is the concentration of electrode j as a function of both time t and particle radius r_j, $D_{s,j}$ is the solid phase diffusion coefficient, and the subscript $j \in \{\mathrm{p}, n\}$ represents the positive/negative electrode. The SoC is a function of the average normalized concentration (stoichiometry) in each electrode (30). To calculate SoC, we first define $x_{s,j,100\%}$ and $x_{s,j,0\%}$ as the stoichiometry at which electrode j is at its maximum and minimum respectively. Using these definitions, SoC is the state of the anode's stoichiometry between $x_{s,n,100\%}$ and $x_{s,n,0\%}$ (or equivalently, 1 - the state of the cathode's stoichiometry between $x_{s,p,100\%}$ and $x_{s,p,0\%}$) [17] as expressed in:

$$x_{s,j,\mathrm{ave}} = \frac{1}{\bar{r}_j c_{s,j,\max}}\int_0^{\bar{r}_j} c_{s,j}\,dr \tag{30}$$

$$\varsigma = \frac{x_{s,n,\mathrm{ave}} - x_{s,n,0\%}}{x_{s,n,100\%} - x_{s,n,0\%}} \tag{31}$$

$$= 1 - \frac{x_{s,p,\mathrm{ave}} - x_{s,p,0\%}}{x_{s,p,100\%} - x_{s,p,0\%}} \tag{32}$$

where ς is the SoC of the cell, $c_{s,j,\max}$ is the maximum concentrations of electrode j, and $\bar{r}_j$ is the radius of the representative particle.

Battery voltage in the SPM is based on the open circuit voltage, the chemical overpotential, and the electrical resistance. while the SoC is based on average concentration throughout the particle, open-circuit-voltage is based only on its surface concentration [17]. These relationships are shown in:

$$v_{oc} = \Phi_p\left(x_{s,p,\mathrm{surf}}\right) - \Phi_n\left(x_{s,n,\mathrm{surf}}\right) \tag{33}$$

$$x_{s,p,\mathrm{surf}} = \frac{c_{s,p}|_{r=\bar{r}_p}}{c_{s,p,\max}} \tag{34}$$

$$x_{s,n,\mathrm{surf}} = \frac{c_{s,n}|_{r=\bar{r}_n}}{c_{s,n,\max}} \tag{35}$$

where $\Phi_p : [0,1] \mapsto \mathbb{R}$ and $\Phi_n : [0,1] \mapsto \mathbb{R}$ are the positive and negative electrode potentials as functions of their normalized surface concentrations ($x_{s,p,\mathrm{surf}}$ and $x_{s,n,\mathrm{surf}}$ respectively). Like with open circuit voltage in the CRM, Φ_p and Φ_n can be approximated using polynomial or exponential functions. Authors in [17], [53] use a Redlich-Kister expansion as a general best fit function for Φ_p and Φ_n:

$$\Phi_j = v_{bat}^0 + \frac{RT}{F}\ln\left(\frac{1 - x_{s,j,\mathrm{surf}}}{x_{s,j,\mathrm{surf}}}\right) + \left\{\sum_{k=0}^{N}\frac{A_k}{F}\left((2x_{s,j,\mathrm{surf}} - 1)^{k+1} - \frac{2x_{s,j,\mathrm{surf}}k(1 - x_{s,j,\mathrm{surf}})}{(2x_{s,j,\mathrm{surf}} - 1)^{1-k}}\right)\right\} \tag{36}$$

where Φ_j is the potential at electrode j, $x_{s,j,\mathrm{surf}}$ is the normalized surface concentration at electrode j, R is the ideal gas constant (8.314 J mol/K), T is the battery temperature in Kelvin,[1] F is Faraday's constant 96,487 coulombs/mol, k is the summation index number, and N, v_{bat}^0 and A_k are the fitting parameters. Figure 13 shows example anode and cathode equilibrium potential functions. When fully charged, the active material concentration is at its maximum in the anode and at its minimum in the cathode. This means there is potential for ion movement from anode to cathode and electron movement from cathode to anode (a.k.a. discharge).

Chemical overpotential can be calculated according to the Butler-Volmer equation [17], [87], [88]:

$$J_j = \frac{i_{\mathrm{bat}}}{a_s AL} = k_j c_{s,j,max} c_e^{1-\alpha_c}(1 - x_{s,j,\mathrm{surf}})^{1-\alpha_c} x_{s,j,\mathrm{surf}}^{\alpha_c} \times \left\{\exp\left(\frac{(1-\alpha_c)F}{RT}\eta_j\right) - \exp\left(-\frac{\alpha_c F}{RT}\eta_j\right)\right\} \tag{37}$$

[1]Note that battery temperature can be assumed to be constant, or this can be coupled with one of the thermal models discussed in Section IV

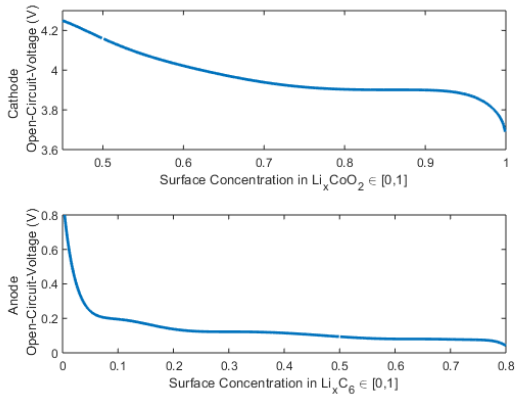

FIGURE 13. Equilibrium potentials (open-circuit-voltages) of lithium-cobalt-oxide ($LiCO_2$) cathode (top) and MesoCarbon MicroBeads (MCMB) anode (bottom) [53].

$$k_j = k_{j,\text{ref}} \exp\left[\frac{E_{k,j}}{R}\left(\frac{1}{T} - \frac{1}{T_{\text{ref}}}\right)\right] \tag{38}$$

where η_j is the reaction overpotential, J_j is the current density on the particle's surface, a_s is the specific interfacial surface area (volumetric fraction of the active material $\times 3/\bar{r}_j$), A is the current collector area, L is the electrode thickness, k_j is the Arrhenius rate of the electrochemical reaction, $E_{k,j}$ is the activation energy of the Arrhenius relationship, c_e is the concentration of the electrolyte, and α_c is the charge-transfer coefficient. This equation can be solved for η_j in terms of i_{bat} making it possible to compute the Jacobian metrics with respect to the parameters as was demonstrated in [88].

Electrical resistance is a combination of resistances in the electrolyte, the current collectors, the tabs, and the terminals. These can all be modeled using an single constant resistor R_{cell}, but it is also common to apply a temperature correction factor, current correction factor, or both [88]. With the open-circuit-voltage, the chemical overpotential, and the electrical resistance calculated, the SPM battery voltage is shown in:

$$v_{\text{bat}} = \Phi_p - \Phi_n + \eta_p - \eta_n + R_{\text{cell}} i_{\text{bat}} \tag{39}$$

To make this model more accurate at high currents, we can extend it to an additional spatial dimension along the length from the anode current collector, through the separator, to the cathode current collector, as illustrated in Fig. 13. With one dimension along the cell's thickness and the pseudo dimension describing a concentration gradient within spherical particles, this is called a pseudo-two-dimensional (P2D) model [17], [89], [90]. Whereas with the SPM, c_e, $x_{s,j,\text{surf}}$, η_j, and therefore the J_j are essentially averaged over each electrode, the P2D represents these quantities as functions of the dimension from one current-collector to the other [91]. Full order P2D built with the partial differential equations are too computationally complex for most real-time control applications [57]. However, discretized or reformulated P2D models can be applied successfully in control applications [10], [57], [58].

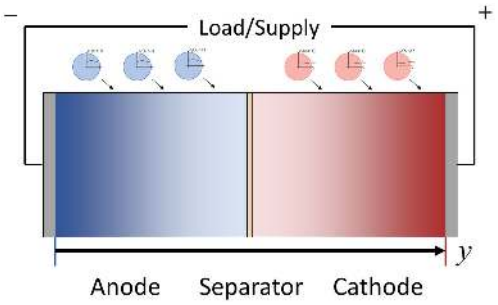

FIGURE 14. Pseudo two-dimensional model (P2D).

1) SPM APPLICATION

In this section we solve the problem outlined in Section II with an optimal controller designed around a SPM. Example parameters for the SPM are listed in Table 6 with Redlich-Kister expansion parameters for the anode and cathode voltages listed in Table 7. The SPM is used here to demonstrate its application, however, it is not the most appropriate model for this problem because of its high complexity relative to the time resolution and scale required. This model would be more appropriate for higher sample rate applications where voltage dynamics are more salient. Further, the model parameters used here are derived from literature sources on cell-level design. With calculated capacity of roughly 1.9 Ah per cell, 445 parallel cells were simulated to achieve a comparable capacity to the CRM (800 Ah). This means that the "Big Cell" modeling assumption extrapolates the performance of a single cell to $445 \times 196 = 87,220$ cells. One advantage of the SPM is that it enables investigation of how changes to cell level design parameters might affect simulated system level performance.

Within each particle we model five discrete volumes to approximate the radial dimension of the model. The core volume is spherical with radius dr_j which is surrounded by four shell volumes each with a thinness of dr_j. Fig. 15 illustrates how electrical current is transformed to current density which is transformed in turn to changes in the chemical concentrations within the modeled volumes. Fick's second law describes a concentration gradient in the representative particle that can be approximated using discrete volumes, each being shells around a spherical core. Each of these shells has a chemical concentration capacity proportional to its volume and the maximum concentration. The surface between each volume has a chemical resistance proportional to the surface area and inversely proportional to the diffusion coefficient. The current density at each particle's surface is proportional to the battery current (i_{bat}). The resulting optimization problem is formulated in:

$$\min_{\mathbf{x}_{\text{SPM}} \in \mathbb{R}^{18n+13}} \quad \Delta t\, \mathbf{w}^\top (\mathbf{l} + \mathbf{p}) + \nu\tau$$

subject to: (40a)

$$\mathbf{p}_{\text{dc}} = \phi_0 \mathbf{p}^2 + \phi_1 \mathbf{p} + \phi_2 \tag{40b}$$

$$\mathbf{p}_{\text{dc}} = \mathbf{i}_{\text{bat}} \mathbf{v}_{\text{bat}} \tag{40c}$$

$$\mathbf{v}_{\text{bat}} = \mathbf{\Phi}_{p[1:n]} - \mathbf{\Phi}_{n[1:n]} + \boldsymbol{\eta}_p - \boldsymbol{\eta}_n + R_0 \mathbf{i}_{\text{bat}}$$

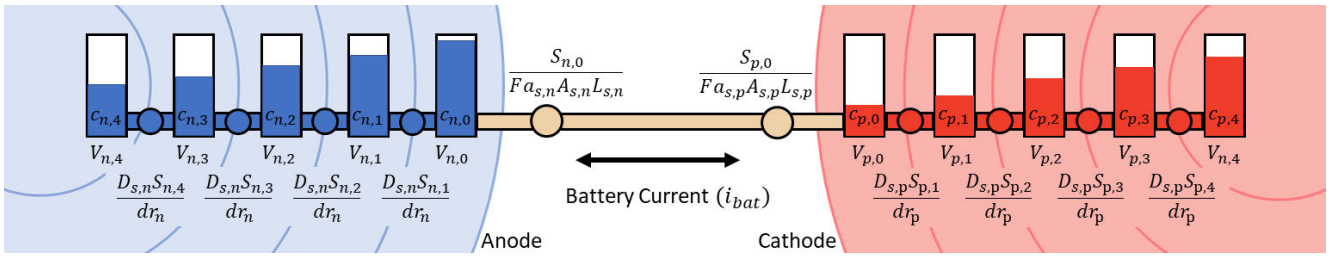

FIGURE 15. Concentration reservoir analogy of the SPM with five discrete volumes per particle.

TABLE 6. Battery System Single Particle Model (SPM) parameters.

Name	Symbol	Units	Anode	Cathode
Diffusion coefficient[a]	$D_{s,j}$	m^2/s	3.9e-14	1.0e-14
Particle Radius[a]	$\bar{r}_j$	m	12.5e-6	8.5e-6
Electrode thickness[a]	$L_{s,j}$	m	7.35e-6	7.0e-6
Electrode area per cell [a]	$A_{s,j}$	m^2	1.1167	0.7824
Volume fraction[b]	$\varepsilon_{s,j}$	m^3/m^3	0.49	0.59
Specific interfacial surface area[a,b]	$a_{s,j}$	m^2/m^3	1.176e5	2.0824e5
Reaction rate constant[b]	$k_{s,j}$	$\frac{A/m^2}{\sqrt{mol/m^3}}$	8.351e-3	6.374e-3
Charge-transfer coefficient[a,b]	α_c		0.5	0.5
Maximum concentration[a,b]	$c_{j,\max}$	mol/m^3	3.1833e4	5.1410e4
Initial concentration (60 %SoC)	$c_{j,\text{init}}$	mol/m^3	1.5917e4	3.4445e4
100% SoC concentration	$c_{j,100\%}$	mol/m^3	2.5466e4	2.3135e4
95% SoC concentration	$c_{j,95\%}$	mol/m^3	2.4273e4	2.4548e4
20% SoC concentration	$c_{j,20\%}$	mol/m^3	0.6366e4	4.1128e4
0% SoC concentration	$c_{j,0\%}$	mol/m^3	0	5.1410e4
Volume 0 (surface)	$V_{j,0}$	m^3	3.9924e-15	1.2553e-15
Volume 1	$V_{j,1}$	m^3	2.42164e-15	7.6144e-16
Volume 2	$V_{j,2}$	m^3	1.2435e-15	3.9101e-16
Volume 3	$V_{j,3}$	m^3	4.5815e-16	1.4406e-16
Volume 4 (core)	$V_{j,4}$	m^3	6.5450e-17	2.0580e-17
Surface Area 0 (surface)	$S_{j,0}$	m^2	1.9635e-9	9.0792e-10
Surface Area 1	$S_{j,1}$	m^2	1.2566e-9	5.8107e-10
Surface Area 2	$S_{j,2}$	m^2	7.0686e-10	3.2685e-10
Surface Area 3	$S_{j,3}$	m^2	3.1416e-10	1.4527e-10
Surface Area 4 (core)	$S_{j,4}$	m^2	7.8540e-11	3.6317e-11
Number of cells in parallel			445	
Total calculated capacity[c]	C_{cap}		802.36 Ah	
Electrolyte concentration [a]	c_e	mol/m^3	1000	
Ideal gas constant	R	J mol/K	8.314	
Faraday constant	F	C/mol	96,487	

[a] - Ref. [88]
[b] - Ref. [85]
[c] - Calculated using method described in Ref. [17]
* Note that the actual configuration would vary by system design (e.g. 5 systems, each with 30 strings, each string with 3 cells in parallel would have 450 cells in parallel)

TABLE 7. Equilibrium potential Redlich-Kister expansion parameters, reproduced from [53].

Parameter	MCMB (anode)	$LiCoO_2$ (cathode)
N	10	7
v^0_{bat}	-1.7203	-29.614
A_0	-0.35799×10^6	0.64832×10^7
A_1	-0.35008×10^6	-0.65173×10^7
A_2	-0.35247×10^6	0.65664×10^7
A_3	-0.35692×10^6	-0.65787×10^7
A_4	-0.38633×10^6	0.63021×10^7
A_5	-0.35908×10^6	-0.50465×10^7
A_6	-0.28794×10^6	0.27113×10^7
A_7	-0.14979×10^6	-0.69045×10^6
A_8	-0.39912×10^6	
A_9	-0.96172×10^6	
A_{10}	-0.63262×10^6	

$$\mathbf{\Phi}_j = v^0_{bat} + \frac{RT}{F}\ln\left(\frac{c_{j,max}-\mathbf{c}_{j,0}}{\mathbf{c}_{j,0}}\right) + \sum_{k=0}^{N}\frac{A_k}{F}\left[\left(\frac{2\mathbf{c}_{j,0}}{c_{j,max}}-1\right)^{k+1} - \frac{2\mathbf{c}_{j,0}k(c_{j,max}-\mathbf{c}_{s,j,0})}{c_{j,max}(2\frac{\mathbf{c}_{j,0}}{c_{j,max}}-1)^{1-k}}\right] \tag{40d}$$

$$\frac{\mathbf{i}_{\text{bat}}}{a_{s,j}A_{s,j}L_{s,j}} = k_{s,j}c_{j,max}c_e^{0.5}(-\mathbf{c}_{j,0[1:n]})^{0.5}\mathbf{c}^{0.5}_{j,0[1:n]} \tag{40e}$$

$$\times\left\{\exp\left(\frac{0.5F}{RT}\boldsymbol{\eta}_j\right) - \exp\left(-\frac{0.5F}{RT}\boldsymbol{\eta}_j\right)\right\} \tag{40f}$$

$$V_{j,0}\mathbf{Dc}_{j,0} = \frac{S_{j,0}\,\mathbf{i}_{\text{bat}}}{F\,a_{s,j}A_{s,j}L_{s,j}} - \frac{D_{s,j}S_{j,1}(\mathbf{c}_{j,1[1:n]}-\mathbf{c}_{j,0[1:n]})}{dr} \tag{40g}$$

$$\frac{dr\,V_{j,1}}{D_{s,j}}\mathbf{Dc}_{j,1} = S_{j,1}(\mathbf{c}_{j,0[1:n]}-\mathbf{c}_{j,1[1:n]}) + S_{j,2}(\mathbf{c}_{j,2[1:n]}-\mathbf{c}_{j,1[1:n]}) \tag{40h}$$

$$\frac{dr\,V_{j,2}}{D_{s,j}}\mathbf{Dc}_{j,2} = S_{j,2}(\mathbf{c}_{j,1[1:n]}-\mathbf{c}_{j,2[1:n]}) \tag{40i}$$

$$+ S_{j,3}(\mathbf{c}_{j,3[1:n]}-\mathbf{c}_{j,2[1:n]}) \tag{40j}$$

$$\frac{dr\,V_{j,3}}{D_{s,j}}\mathbf{Dc}_{j,3} = S_{j,3}(\mathbf{c}_{j,2[1:n]}-\mathbf{c}_{j,3[1:n]}) \tag{40k}$$

$$+ S_{j,4}(\mathbf{c}_{j,4[1:n]}-\mathbf{c}_{j,3[1:n]}) \tag{40l}$$

$$\frac{dr\,V_{j,4}}{D_{s,j}}\mathbf{Dc}_{j,4} = S_{j,4}(\mathbf{c}_{j,3[1:n]}-\mathbf{c}_{j,4[1:n]}) \tag{40m}$$

$$\mathbf{c}_{j,\{0:4\},[1]} = \mathbf{c}_{j,\text{init}}[\mathbf{1}] \tag{40n}$$

$$\mathbf{c}_{j,\{0:4\},[n]} = \mathbf{c}_{j,\text{init}}[\mathbf{1}] \tag{40o}$$

$$p_{\min}[\mathbf{1}] \le \mathbf{p} \le p_{\max}[\mathbf{1}] \tag{40p}$$

$$v_{\min}[\mathbf{1}] \le \mathbf{v}_{\text{bat}} \le v_{\max}[\mathbf{1}] \tag{40q}$$

$$i_{\min}[\mathbf{1}] \le \mathbf{i}_{\text{bat}} \le i_{\max}[\mathbf{1}] \tag{40r}$$

$$[\mathbf{0}] \le \mathbf{c}_{j,\{0:4\}} \le c_{j,max}[\mathbf{1}] \tag{40s}$$

$$\mathbf{l} + \mathbf{p} \le \tau[\mathbf{1}] \tag{40t}$$

where $\mathbf{x}_{\text{SPM}} = \{\mathbf{p}, \mathbf{p}_{dc}, \mathbf{i}_{\text{bat}}, \mathbf{v}_{\text{bat}}, \mathbf{\Phi}_p, \mathbf{\Phi}_n, \boldsymbol{\eta}_p, \boldsymbol{\eta}_n, \mathbf{c}_{p,\{0:4\}}, \mathbf{c}_{n,\{0:4\}}, \tau\} \in \mathbb{R}^{18n+13}$, $\mathbf{\Phi}_p \in \mathbb{R}^{n+1}$ and $\mathbf{\Phi}_n \in \mathbb{R}^{n+1}$ are the

open-circuit-voltages of the cathode and anode respectively, $\boldsymbol{\eta}_p \in \mathbb{R}^n$ and $\boldsymbol{\eta}_n \in \mathbb{R}^n$ are the overpotential voltages of the cathode and anode respectively, and $\mathbf{c}_{p,\{0:4\}} \in \mathbb{R}^{5\times(n+1)}$ and $\mathbf{c}_{n,\{0:4\}} \in \mathbb{R}^{5\times(n+1)}$ are the molar concentrations of active material in the five discretized volumes of the cathode and anode respectively.

Under this control design customer's net load and optimal control schedule for the BESS are shown in Fig. 16 (a) and (b) respectively. The simulated battery current and voltage are shown in Fig. 16 (c) and (e) respectively. The SPM based controller expects to be able to reduce the peak load by approximately 86 kW. The peak battery voltage reached 800 V and the dc current reached -125 A on discharge. Note that the dc voltage is based on the anode and cathode voltage functions which are in turn based on anode and cathode concentration fractions. As these functions are different from what the CRM uses, the results are not directly comparable. As shown in Fig. 16 (f) and (g), the cathode concentration fraction ranges from 0.50 at peak SoC to 0.87 at minimum SoC while the anode concentration ranges from 0.76 at peak SoC to 0.2 at minimum SoC. At low current densities there is almost no difference between core and surface particle concentrations. The control solution reduces the total electrical bill from \$52,080 (\$50,000 demand, \$2,080 energy) to \$47,754 (\$45,682 demand, \$2072 energy). The net effect is a \$4,325, or 8.31%, reduction in the electrical bill.

The SPM is structurally similar to the CRM, as illustrated in the comparison of Fig. 9 and Fig. 15. However, the SPM accounts for overpotential voltages in a different way from the equivalent circuit models in the CRM. These differences are not salient at the low sample rate in the example application and hence the models appear to have very similar results.

IV. TEMPERATURE MODELS

Temperature is a critical factor to consider when controlling BESS. Cell temperature can affect many of the parameters for the SoC and SoH models discussed in Sections III and V. The highest cell temperature can be the limiting factor for control action in hot environments or under high power conditions. Constraining temperature prevents over-temperature and, in a few cases, under-temperature conditions which can shorten battery life or cause hazards such as thermal run-away. The following constraint enforces limits on temperature:

$$T_{\min} \le T \le T_{\max} \tag{41}$$

where T is the battery temperature, $T_{\min}$ is the minimum battery temperature, and $T_{\max}$ is the maximum battery temperature.

Battery specification sheets will often define a lower maximum charge rate at higher temperatures [92]. This requirement would specify a conditional dynamic charge limit based on if the battery temperature exceeds a given threshold, an example of which is shown in:

$$i_{\min} \le i_{\text{bat}} \le i_{\max} \tag{42a}$$
$$i_{\text{bat}} \le i'_{\max} \tag{42b}$$

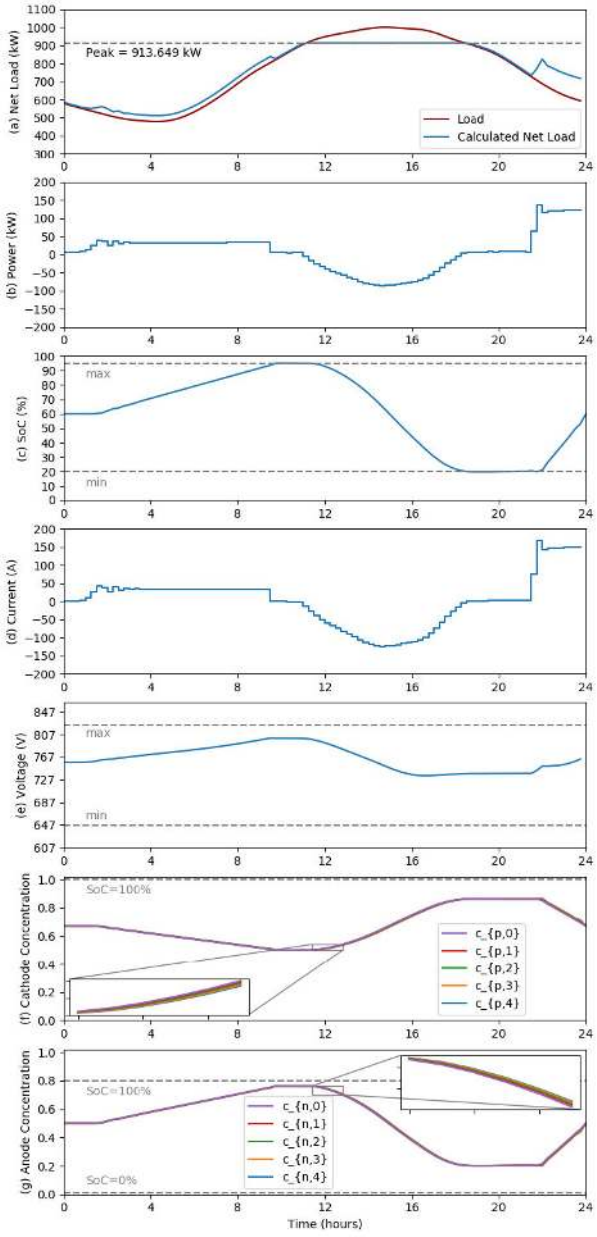

FIGURE 16. Results calculated with the SPM (a) net load with BESS power control, (b) battery power, (c) battery SoC, (d) battery current, (e) battery voltage, (f) cathode concentration fraction, (g) anode concentration fraction.

$$i'_{\max} = \begin{cases} i_{\max} & \text{if } T \le T_{\text{thr}} \\ i_{\max}/2 & \text{if } T_{\text{thr}} < T \le T_{\max} \\ 0 & \text{if } T > T_{\max} \end{cases} \tag{42c}$$

where $i'_{\max}$ is a dynamic charge current limit, T_{thr} is the temperature threshold. This type of constraint is non-convex and difficult to work with in optimal control design. Alternatively, these restrictions can be implemented with affine constraints on current as in:

$$m_1 T + b_1 \le i_{\text{bat}} \le m_2 T + b_2 \tag{43a}$$
$$m_3 T + b_3 \le i_{\text{bat}} \le m_4 T + b_4 \tag{43b}$$

TABLE 8. Summary of temperature models.

Model Type	Measurable Variables	Calculated Variables	Parameters*	Advantages	Disadvantages	References
Cell Lumped-volume resistive-heating conduction-cooling	T_{env}, T	•	C_{T}, R_0, U	lowest computational complexity, convex	lowest predictive accuracy	[95]–[97]
Cell Internal/surface-volumes resistive/overpotential-heating conduction/radiation-cooling	T_{env}, T	T'	C_{T}, C'_{T}, R_0, U, σ_{em}	low computational complexity, convex reformulation, improved accuracy at high temperature gradients	low to moderate predictive accuracy	[51], [98], [99]
Cell Multiple-internal-volumes resistive/overpotential/entropy-heating conduction/radiation/convection-cooling	$T_{\text{env}}, T, u_\infty$	$T'_{\{1:K\}}$	$C_{\text{T}\{1:K\}}$, $\Delta S(\varsigma)$**, R_0, $U(\mu_\infty)$***, σ_{em}	high predictive accuracy, entropy term improves accuracy at low currents	moderate to high complexity and computational burden	[10], [88], [98], [100]–[102]
Enclosure Lumped-air-volume HVAC efficiency cooling	$T_{\text{env}}, T_{\text{EN}}, T$	•	$C_{\text{EN}}, U_{\text{EN}}, N_{\text{cell}}$	low computational complexity, convex	low to moderate predictive accuracy	[98](includes heater temperature)
Enclosure Lumped-air-volume w/ heat-exchanger HVAC efficiency/Fan speed cooling	$T_{\text{env}}, T_{\text{EN}}, T, u_\infty$	T_{EX}		somewhat higher predictive accuracy	enables fan speed control, higher complexity, non-convex	[101]

*All inputs, outputs, state variables and parameters presented here are in addition to those presented for the CRM, with dynamic voltages model from Section III

**The function $\Delta S(\varsigma)$ can vary significantly with ς and depends on the specific battery chemistry. However, it is commonly ignored ($\Delta S = 0$) or assumed to be constant ($\frac{\partial \Delta S}{\partial t} = 0$).

***The heat transmittance U is a function of the thermodynamic properties of the environment and the velocity of fluid flow over the conductive surface. Under a constant flow rate, U can be assumed to be constant.

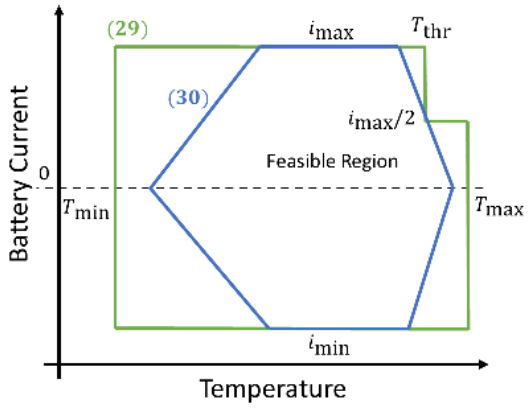

FIGURE 17. Notional examples of temperature dependent current limits.

where m_{1-4} and b_{1-4} are the slopes and intercepts of the temperature dependent current constraints. Fig. 17 shows how the constraints in (42) and (43) enclose different feasible regions. This kind of limit can be imposed on dc power instead of current [93].

Battery temperature models are based on how much heat is generated in the cell, and how much heat is lost to the environment. As controllers must balance accuracy with model complexity, we cannot use the high order finite-element-models used in simulation based design, like in [94]. Instead controller models choose a few critical temperatures to represent. Section IV-A explains the physical mechanisms underlying heat generation and transfer for batteries. Section IV-C then introduces several specific modeling approaches that can incorporate temperature into optimal control decisions. Table 8 shows a summary of the benefits and tradeoffs of the different temperature models as they apply to optimal controller design.

A. HEAT GENERATION, CONSUMPTION, AND TRANSFER

The temperature of the battery is a function of the rate of heat generated by the battery during operation (J_{in}) and the rate of heat lost to the environment (J_{out}). Heat is generated or consumed by an electrochemical cell in three ways: change in entropy, overpotential losses, and resistive heating. Changes in entropy from the electrochemical reactions reversibly generate and consume heat within cells. This process is referred to as reversible heat generation because the heat generated during charge or discharge is consumed during the reverse reaction. Charging a battery can be endothermic (e.g., some types of lithium batteries in specific ranges of SoC), or exothermic (e.g., lead-acid batteries) [10], [65], [88], [100], [102], [103]. When losses are considered, we reintroduce the equivalent circuit models outlined in Section III-B. Overpotential losses result from the kinetic and mass transport aspects of the chemical recreation which are modeled by the resistor-capacitor ladder in the 2^{nd} order equivalent circuit. The voltage drop across these elements are v_1 and

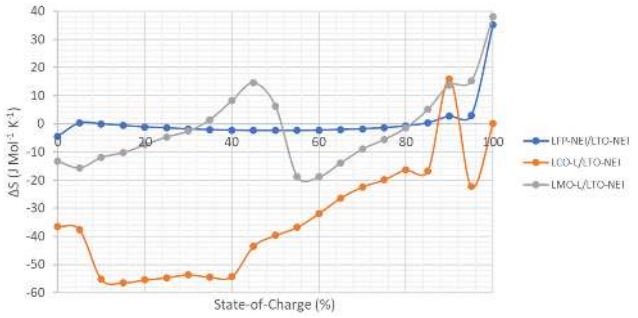

FIGURE 18. Computed full cell ΔS from individual electrode ΔS for three types of lithium-ion batteries, replotted with data from [104].

v_2 respectively. Alternatively, if the SPM or P2D model is used for a SoC model, the overpotential voltages η_p and η_n can be used in place of v_1 and v_2. Resistive or joule heating losses result from the power dissipated to the battery's internal resistance. Combining these three sources of internal heat generation yields :

$$J_{\text{in}} = i_{\text{bat}} T \frac{\Delta S(\varsigma)}{n_{\text{mol}} F} + (v_1 + v_2) i_{\text{bat}} + R_0 (i_{\text{bat}})^2 \tag{44}$$

where J_{in} is the rate of heat generation (W), i_{bat} is the battery current (A), T is battery temperature (K), ΔS is the change in entropy ($\Delta S = n_{\text{mol}} F(\partial v_{\text{oc}}/\partial T)$), n_{mol} is the number of electrons per reaction, F is the Faraday constant (-1/96,485 Coulombs per electron), v_1 and v_2 are the dynamic battery voltages from the equivalent circuit (V), R_0 is the battery internal resistance (Ω), and v_{oc} is the open-circuit-voltage (V). The total change in entropy in a battery can change drastically as a function of SoC which can be difficult to model for the purposes of control design. The change in entropy over the domain of SoC was calculated from precise measurements of $\partial v_{\text{oc}}/\partial T$ for a selection of lithium-ion battery types as shown in Fig. 18 [104]. From these data we can contrast the low entropic heat generated on discharge from lithium-iron-phosphate (LFP) batteries to the relatively high entropic heat from lithium-cobalt-oxide (LCO), especially in the range of 10% to 40% SoC. Lithium-manganese-oxide (LMO) batteries in further contrast change from generating heat (negative ΔS) to consuming heat (positive ΔS) when passing 50% SoC on discharge. Depending on the battery chemistry, and the range of operational SoC, the $\Delta S(\varsigma)$ function may be neglected entirely, or approximated by a constant, a linear function, a quadratic function, or cubic function, or even a cubic spline [56], [105]. Accurate yet simple models for changes in entropy that controllers can use to predict temperature are an underdeveloped area that warrants additional research.

Most of the heat generated in a cell, especially in high power applications, comes from the resistive heating term. Because of this, some choose to ignore overpotential losses and the thermochemistry entirely [95]. Just as with the equivalent circuit, the heat generation can be calculated with different sets of parameters depending on if the battery is charging or discharging. However, the accuracy improvement may not warrant the increased computational complexity.

Heat can be transferred between the battery and the environment through conduction, radiation, and convection. Heat conduction is proportional to the temperature difference while heat radiation is proportional to the temperature of the surface raised to the 4^{th} power according to Stefan-Boltzmann's law [106]. The combined heat loss function is shown in:

$$J_{\text{out}} = U(T_{\text{env}} - T) + \epsilon \sigma_{\text{em}} (T_{\text{env}}^4 - T^4) \tag{45}$$

where J_{out} is the rate of heat loss (W), U is the battery's thermal transmittance with its environment (W/K), T_{env} is the environmental temperature (K), ϵ is the Stefan-Boltzmann constant (5.6×10^{-8} Wm^{-2} K^{-4}), σ_{em} is the emission ratio with respect to the ideal (0.95 is common for plastics in a variety of battery designs [106]).

In an unregulated environment T_{env} can be forecasted based on local weather data. In a temperature controlled environment, it can sometimes be assumed that T_{env} is a constant. The heat transfer from radiation is normally much smaller than then heat conduction meaning that it can be ignored in many systems. A simplifying assumption is that the airflow rate is constant, thereby yielding a constant U. However, in some cases variable speed fans can be integrated into the optimal control design. Under variable airflow conditions the rate of heat transfer is described by Nusselt number (Nu) which itself is a function of Reynolds number (Re) and Prandtl number (Pr). One example of this relationship, from [107], is shown in:

$$\text{Re} = \frac{\rho \, u_\infty \, l_{\text{mm}}}{\mu} \tag{46a}$$

$$\text{Nu} = C_{\text{l}} \, \text{Re}^{\theta} \, \text{Pr}^{\frac{1}{3}} \tag{46b}$$

$$U = \frac{\text{Nu} \, k_{\text{tc}}}{l_{\text{mm}}} \tag{46c}$$

where ρ is the fluid's density, u_∞ is the unobstructed velocity of the fluid, l_{mm} is the characteristic length, μ is the dynamic viscosity, C_{l} and θ are empirically derived model parameters, and k_{tc} is the thermal conductivity of the fluid.

Table 9 shows the thermodynamic constants associated with air and water under standard temperature and pressure. As water has a much higher density and thermal conductivity, some BESS designs include water cooling systems [108]. For a cylinder in cross-flow, the characteristic length l_{mm} equals the diameter (18.63 mm for an 18650-type cell). The parameters C_{l} and θ, shown in Table 10, are properties of the geometry of the fluid flow over the battery surface and change with the Reynolds number. Together, these material properties yield the functional relationship between air speed thermal transmittance shown in Fig. 19.

The complex relationships described in (46) impact control design in several ways. First, heat transfer rate increases with increasing fluid velocity u_∞. However, there are diminishing returns meaning that the marginal improvement in heat transfer decreases with increased fluid velocity. Hence there

TABLE 9. Thermodynamic properties of common battery cooling fluids* [107].

Fluid	ρ (kg/m^2)	μ (N·s/m^2)	k_{tc} (W/m·K)	Pr
Air	1.1614	$1.846e^{-5}$	0.0263	0.707
Water	997.0	$8.55e^{-4}$	0.613	0.857

*all values reported assume atmospheric pressure and 300 Kelvin

TABLE 10. Fluid flow geometry constants for a cylinder in cross-flow [107].

Re	C_1	θ
0.4-4	0.989	0.330
4-40	0.911	0.385
40-4000	0.683	0.466
4000-40,000	0.193	0.618
40,000-400,000	0.027	0.805

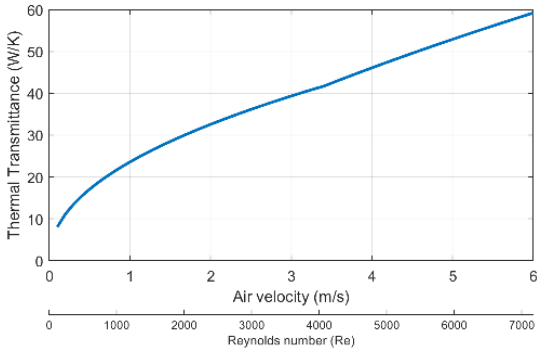

FIGURE 19. Thermal transmittance for a 18650 battery cell in cross flow as a function of air speed [107].

is likely to be an optimal, non-zero flow rate that effectively transfers heat while not consuming too much power to move air. A fan controller can be implemented to optimize battery temperature along with charge/discharge [101].

B. ENCLOSURE THERMAL MODEL

The simplest enclosure thermal model is implicit in the assumption of constant environmental temperature. This is valid if the BESS is small and installed in a temperature-controlled space. Temperature forecasts can be used in environments where temperature is weather dependent. As there is generally thermal separation between the weather dependent environment and the environment that the batteries are operating in, we can model these temperatures separately.

For a given BESS and environment, the heat transfer rate between the enclosure and the environment U_{EN} can be empirically calculated with heating ventilation and air conditioning (HVAC) systems off, and over their range of control. We may also consider the effect of solar heating which is proportional to irradiance. The HVAC power draw can also be calculated under these conditions, and the resulting functions can be included in the BESS model. Further, an HVAC system can transfer a greater amount of heat from the enclosure to the environment, or vice versa, than it requires in electrical energy. The efficiency of a room air conditioner is measured in the energy efficiency ratio (EER), which is the ratio of Btu per hour cooling to power input (W). The EER ranges from roughly 10-20 for high efficiency units [109] which, given that 1 Btu per hour = 0.293 watts, correlates to a energy efficiency (η_{HVAC}) of 300-700%. A modified version of the heat dissipation equation for a BESS enclosure is shown in:

$$J_{\text{EN,out}} = U_{\text{EN}}(T_{\text{env}} - T_{\text{EN}}) + \epsilon\sigma_{\text{em}}(T_{\text{env}}^4 - T_{\text{EN}}^4) + \epsilon\sigma_{\text{em}} p_{\text{irr}} - \eta_{\text{HVAC}} p_{\text{HVAC}} \quad (47)$$

where U_{EN} is the thermal transmittance between the enclosure and the environment, T_{EN} is the enclosure temperature, p_{irr} is solar irradiance, p_{HVAC} is the ac power load of the HVAC unit, and η_{HVAC} is the HVAC's energy efficiency. This approach assumes constant airflow and temperature in the HVAC's heat exchanger. By modeling the heat exchanger temperature and fan, we can improve the controller's accuracy predicting temperature management costs. The expanded enclosure thermal model is shown in:

$$J_{\text{EN,out}} = U_{\text{EN}}(T_{env} - T_{\text{EN}}) + \epsilon\sigma_{\text{em}}(T_{\text{env}}^4 - T_{\text{EN}}^4) + \epsilon\sigma_{\text{em}} p_{\text{irr}} + U_{\text{EX}}(u_\infty)(T_{\text{EX}} - T_{\text{EN}}) \quad (48a)$$

$$C_{\text{EX}} \frac{\partial T_{\text{EX}}}{\partial t} = U_{\text{EX}}(u_\infty)(T_{\text{EN}} - T_{\text{EX}}) - \eta_{\text{HVAC}} p_{\text{HVAC}} \quad (48b)$$

$$u_\infty = \eta_{\text{fan}} p_{\text{fan}} \quad (48c)$$

where $U_{\text{EX}}(u_\infty)$ is the thermal transmittance between the HVAC heat exchanger and the air, which is a function of the airflow u_∞, T_{EX} is the heat exchanger temperature, C_{EX} is the heat exchanger's heat capacity, p_{fan} is the fan power, and η_{fan} is the fan's efficiency (m s^{-1} kW^{-1}).

Many HVAC systems are controlled using thermostats, which activate heating or cooling modes when outside a set temperature range. The simplest thermostat implementation is shown in:

$$p_{\text{HVAC}} = \begin{cases} p_{\text{cool}} & T_{\text{EN}} > T_{\text{high}} \\ 0 & T_{\text{low}} \le T_{\text{EN}} \le T_{\text{high}} \\ p_{\text{heat}} & T_{\text{EN}} < T_{\text{low}} \end{cases} \quad (49a)$$

where p_{cool} is the power of the HVAC when in cooling mode, p_{heat} is the heating power of the HVAC when in heating mode, and T_{high} and T_{low} are the high and low environment temperature limits respectively. To limit the on/off cycling frequency, the mode will often stay latched for a set duration, or until the desired temperature is reached. However, this operational mode is recursive, meaning it is difficult to incorporate into a computationally efficient optimal controller design. If it is feasible in the design of the HVAC system, HVAC power (p_{HVAC}) and/or fan power (p_{fan}) can be decision variables available to the controller. This modeling approach enables optimal HVAC control scheduling, including pre-cooling batteries [101] or pre-heating batteries [98] to prepare for usage later in the control horizon.

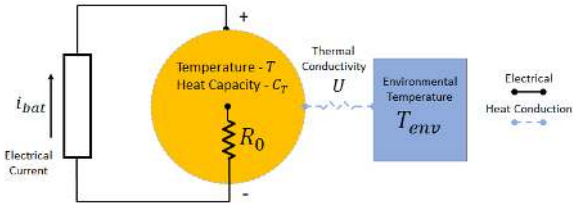

FIGURE 20. Cell thermal model w/ a lumped-volume, resistive-heating, and conduction-cooling.

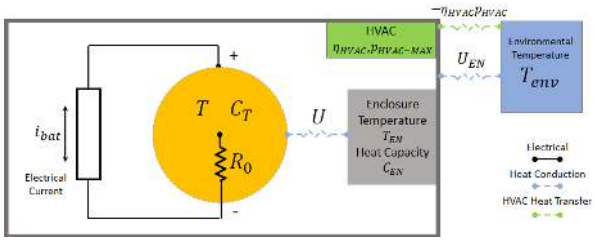

FIGURE 21. Enclosure model with lumped-air-volume and HVAC efficiency cooling.

C. TEMPERATURE MODEL TYPES

In this section we develop several increasingly complex, battery-cell thermal models to illustrate the different options for thermal model design. To build these models we pull together the physical mechanisms discussed in Sections IV-A and IV-B into systems of constraints. The simplest, and most widely used, model is to only represent a single temperature (often the hottest cell), considering only resistive heating and conduction-based cooling. An example of this type of model is shown in Fig. 20 and in:

$$C_{\mathrm{T}}\frac{\partial T}{\partial t} = R_0(i_{\mathrm{bat}})^2 + U(T_{\mathrm{env}} - T) \tag{50}$$

where C_{T} is the heat capacity of the lumped-volume. In this lumped-volume model the measurable surface temperature is assumed to be the temperature throughout the cell [95], [96]. Note that while we have depicted the cell geometry as cylindrical, this approach works equally well for pouch or prismatic cells. Note that when only the hottest cell is represented, imposing a low temperature constraint is unnecessary and potentially misleading. Instead, the low temperature limit is enforced either by battery selection at the design stage (i.e. picking a battery chemistry that is suitable for its environment) or by designing a HVAC system with a thermostat that regulates environmental temperature.

Where the BESS includes an enclosure with a controllable HVAC system, the model can include an additional state variable for the enclosure temperature [98] as in Fig. 21 and in:

$$\begin{aligned} C_{\mathrm{T}}\frac{\partial T}{\partial t} &= R_0(i_{\mathrm{bat}})^2 + U(T_{\mathrm{EN}} - T) \\ C_{\mathrm{EN}}\frac{\partial T_{\mathrm{EN}}}{\partial t} &= N_{\mathrm{cell}}\left(U\left(T - T_{\mathrm{EN}}\right)\right) + U_{\mathrm{EN}}(T_{\mathrm{env}} - T_{\mathrm{EN}}) \\ &\quad - \eta_{\mathrm{HVAC}} p_{\mathrm{HVAC}} \end{aligned} \tag{51a}$$

where C_{EN} is the heat capacity of the BESS enclosure, U_{EN} is the thermal transmittance between the enclosure and the environment, and N_{cell} is the number of cells in the enclosure. This model assumes constant or no airflow.

While temperature measurement is performed on the surface of batteries it is a better practice to constrain operation based on limiting the maximum internal temperature [51], [99]. The internal temperature can be estimated based on the surface temperature and the battery's operation. We can also include battery over-potential heating to improve accuracy as shown in:

$$\begin{aligned} C'_{\mathrm{T}}\frac{\partial T'}{\partial t} &= (v_1 + v_2)i_{\mathrm{bat}} + R_0(i_{\mathrm{bat}})^2 && \text{(52a)} \\ &\quad + U'(T - T') && \text{(52b)} \\ C_{\mathrm{T}}\frac{\partial T}{\partial t} &= U'(T' - T) + U(T_{\mathrm{env}} - T) \\ &\quad + \epsilon\sigma_{\mathrm{em}}(T_{\mathrm{env}}^4 - T^4) && \text{(52c)} \end{aligned}$$

where C'_{T} is the heat capacity of the internal mass of the cell, T' is the internal temperature, and U' is the thermal transmittance between the internal mass to the surface. As the model now distinguishes between surface and internal temperature, C_{T} is now the heat capacity of the surface of the cell, T is the surface temperature, and U is the thermal transmittance between the battery surface and its environment. The resulting model structure is illustrated in Fig. 22.

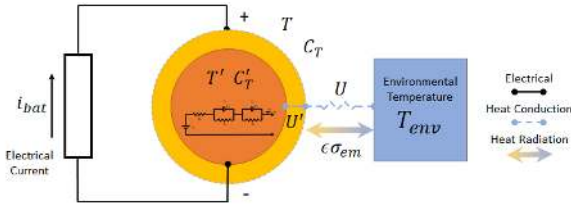

FIGURE 22. Cell thermal model w/ internal and surface-volumes, resistive and overpotential heating, and conduction/radiation cooling.

Building on this framework we can add additional internal volumes, entropy based heating, and convection cooling as a function of air velocity as shown in:

$$\begin{aligned} &C'_{T1}\frac{\partial T'_1}{\partial t} \\ &= U'_1(T'_2 - T'_1) \\ &\quad + V_1\left(i_{\mathrm{bat}}T'_1\frac{\Delta S(\varsigma)}{n_{\mathrm{mol}}F} + (v_1 + v_2)i_{\mathrm{bat}} + R_0(i_{\mathrm{bat}})^2\right) \\ &C'_{T[2:K]}\frac{\partial T'_{[2:K]}}{\partial t} \\ &= U'_{[2:K]}(T'_{[3:K+1])} - T'_{[2:K]}) && \text{(53a)} \\ &\quad + V_{[2:K]}\left(i_{\mathrm{bat}}T'_{[2:K]}\frac{\Delta S(\varsigma)}{n_{\mathrm{mol}}F} + (v_1 + v_2)i_{\mathrm{bat}} + R_0(i_{\mathrm{bat}})^2\right) \\ &\quad + U'_{[1:K-1]}(T'_{[1:K-1]} - T'_{[2:K]}) && \text{(53b)} \end{aligned}$$

$$C_T \frac{\partial T}{\partial t} = U(u_\infty)(T_{\text{env}} - T) + U'_K(T'_K - T) + \epsilon\sigma_{\text{em}}(T_{\text{env}}^4 - T^4) \tag{53c}$$

where $T_{T[1:K]'}$ are the K internal temperatures, $C_{T[1:K]'}$ are each internal volume's heat capacity, $V'_{[1:K]}$ are the volumetric fractions of each internal volume normalized to the total internal volume, and $U'_{[1:K]}$ are the thermal transmittances between internal volumes. Note that for notation simplicity the surface temperature $T'_{K+1} = T$ in (53b). The resulting model structure is illustrated in Fig. 23.

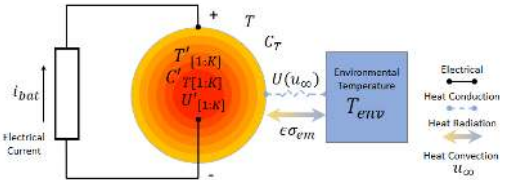

FIGURE 23. Cell model with multiple-internal-volumes, resistive/overpotential/entropy-heating, and conduction/radiation/convection-cooling.

To take advantage of the convection cooling term, the enclosure model can be further developed to include fan power, air velocity, and the temperature of the HVAC heat-exchanger. To accomplish this, we replace T_{env} with T_{EN} in (53c) and add the additional constraints shown in:

$$\begin{aligned} C_{\text{EN}} \frac{\partial T_{\text{EN}}}{\partial t} &= N_{\text{cell}} \left(U(u_\infty)(T - T_{\text{EN}}) + \epsilon\sigma_{\text{em}}(T^4 - T_{\text{EN}}^4) \right) \\ &\quad + U_{\text{EN}}(T_{\text{env}} - T_{\text{EN}}) + \epsilon\sigma_{\text{EN}}(T_{\text{env}}^4 - T_{\text{EN}}^4) \\ &\quad + U_{\text{EX}}(u_\infty)(T_{\text{EX}} - T_{\text{EN}}) \end{aligned} \tag{54a}$$

$$C_{\text{EX}} \frac{\partial T_{\text{EX}}}{\partial t} = U_{\text{EX}}(u_\infty)(T_{\text{EN}} - T_{\text{EX}}) - \eta_{\text{HVAC}} p_{\text{HVAC}} \tag{54b}$$

$$u_\infty = \eta_{\text{fan}} p_{\text{fan}} \tag{54c}$$

where T_{EX} is the heat-exchanger temperature, C_{EX} is the heat exchanger heat capacity, $U_{\text{EX}}(u_\infty)$ is the air velocity dependent thermal transmittance between the air and heat-exchanger, p_{fan} is the fan power, and η_{fan} is the fan efficiency. The resulting model structure is illustrated in Fig. 24.

There are many useful combinations of these models. For example, a controller may want to have a more detailed cell model and a less detailed enclosure model or vice-versa. Alternatively, these models can be customized to a specific cell design or enclosure architecture. The "Big cell" modeling assumption is commonly used but the "Short-board effect" and "One-by-one calculation" can be used in thermal modeling as well. A similar model extension to the enclosure would be to represent a finite number of internal volumes. Each cell would reside within a volume and the heat transfer would only depend on that volume's temperature. Each of these options greatly increases model complexity with unknown, perhaps limited, benefits to controller performance.

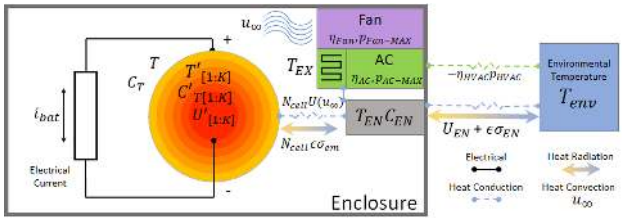

FIGURE 24. Enclosure model with, lumped-air-volume, heat-exchanger temperature, HVAC efficiency and fan speed based cooling.

TABLE 11. Example battery system temperature model parameters.

Name	Symbol	Value
Battery Thermal Transmittance	U	$0.2\ W/°\text{C}$
Battery Heat Capacity	C_{T}	$1.495\ J/°\text{C}$
Maximum Temperature	$T_{\max}$	45 °C
Initial Battery Temperature	T_0	40 °C
Minimum Temperature	$T_{\min}$	-20 °C
Nominal Temperature	T_{nom}	20 °C
Enclosure Thermal Transmittance	U_{EN}	$1\ W/°\text{C}$
Enclosure Heat Capacity	C_{EN}	$30\ kJ/°\text{C}$
Initial Enclosure Temperature	T_{EN0}	40 °C
Max HVAC power	$p_{\text{HVAC-max}}$	$100\ kW$
HVAC Efficiency	η_{HVAC}	700%

Note: these model parameters are meant to represent a typical battery system and do not necessarily reflect any specific equipment.

1) TEMPERATURE MODEL APPLICATION

For this application we solve the optimal control problem in Section II using a thermal model. However, in this section we assess how the control changes if it is in a very hot environment. In some regions, the temperature can commonly reach 43.3 °C (110 °F) during the day. BESS in such an environment are generally installed in enclosures with HVAC systems. Given this environment, we determine an optimal control schedule for both the BESS power and the HVAC system power using the parameters in Table 11. The modified objective and constraints, in addition to those for the CRM defined in Section III-B.1, are shown in:

$$\min_{\mathbf{x}_{\text{T}} \in \mathbb{R}^{9n+5}} \Delta t\, \mathbf{w}^\top (\mathbf{l} + \mathbf{p} + \mathbf{p}_{\text{HVAC}}) + \nu\tau \tag{55a}$$

subject to:

$$\vdots \text{ in addition to the constraints in (28)}$$

$$\mathbf{l} + \mathbf{p} + \mathbf{p}_{\text{HVAC}} \le \tau \tag{55b}$$

$$C_{\text{T}}\mathbf{DT} = R_0(\mathbf{i}_{\text{bat}})^2 + U(\mathbf{T}_{\text{EN}[1:n]} - \mathbf{T}_{[1:n]}) \tag{55c}$$

$$C_{\text{EN}}\mathbf{DT}_{\text{EN}} = K_{\text{H}}(\mathbf{T}_{[1:n]} - \mathbf{T}_{\text{EN}[1:n]}) + U_{\text{EN}}(\mathbf{T}_{\text{env}} - \mathbf{T}_{\text{EN}[1:n]}) - \eta_{\text{HVAC}}\mathbf{p}_{\text{HVAC}} \tag{55d}$$

$$\mathbf{T}_{[1]} = T_0 \tag{55e}$$

$$\mathbf{T}_{\text{EN}[1]} = T_0 \tag{55f}$$

$$\mathbf{T} \le T_{\max}[\mathbf{1}] \tag{55g}$$

$$[\mathbf{0}] \le \mathbf{p}_{\text{HVAC}} \le p_{\text{HVAC-max}}[\mathbf{1}] \tag{55h}$$

where $\mathbf{x}_T = \{\mathbf{p}, \mathbf{p}_{dc}, \mathbf{i}_{bat}, \mathbf{v}_{bat}, \mathbf{v}_{oc}, \varsigma, \mathbf{T}, \mathbf{p}_{HVAC}, \mathbf{T}_{EN}, \tau, \} \in \mathbb{R}^{9n+5}$, $\mathbf{T} \in \mathbb{R}^{n+1}$ is the temperature of the hottest cell at each time step, $\mathbf{T}_{EN} \in \mathbb{R}^{n+1}$ is the enclosure temperature, and $\mathbf{i}_{bat} \in \mathbb{R}^n$ is the dc current. The environmental temperature is assumed to be sinusoidal, with a period of 24 hours, a peak of 45°C at 3:00 pm, and a magnitude of 2.5°C. The formal expression for the temperature is shown in:

$$\mathbf{T}_{env} = 2.5 \cos\left(\frac{2\pi\ \Delta t}{24} k - 15\right) + 42.5 \quad \forall k \in \{1, 2, \ldots n\} \tag{56}$$

where $\mathbf{T}_{env} \in \mathbb{R}^n$ is the environmental temperature at each time step.

The net load achieved over the control horizon from the combined SoC-Thermal model is shown in Fig. 25 (a). The optimal control schedule calculated is shown in Fig. 25 (b). The HVAC power schedule is shown in Fig. 25 (d) and the environmental, battery, and enclosure temperature trajectories are shown in Fig. 25 (e). The controller can anticipate a period of high temperature and pre-cool the enclosure, and hence the battery, to achieve the desired schedule. Note also that the pre-cooling takes place during the off-peak electricity pricing period. The magnitude and duration of the HVAC cooling is precisely tuned such that the battery's temperature reaches its limit ($45\ ^\circ C$) exactly at the end of the schedule. Note also that the power profile no-longer preferentially charges during off-peak times. This is a result of the quadratic increase in temperature from high rate charging that generates too much heat for the system to transfer to the environment cost-effectively.

The control solution reduces the total electrical bill from \$52,080 (\$50,000 demand, \$2,080 energy) to \$48,001 (\$45,871 demand, \$2,130 energy). Within the energy bill, the energy required to cool the battery accounts for \$51. The net effect is a \$4,079 (7.83%) reduction from the baseline electrical bill, or a \$53 (0.11%) increase in the electrical bill calculated using only the CRM. The more important comparison is that if we model battery temperature in this environment under the control solution developed using only the CRM, the hottest battery reaches a peak temperature of $55.6\ ^\circ C$. By incorporating a thermal model into the controller, we can plan control actions to maintain defined temperature limits.

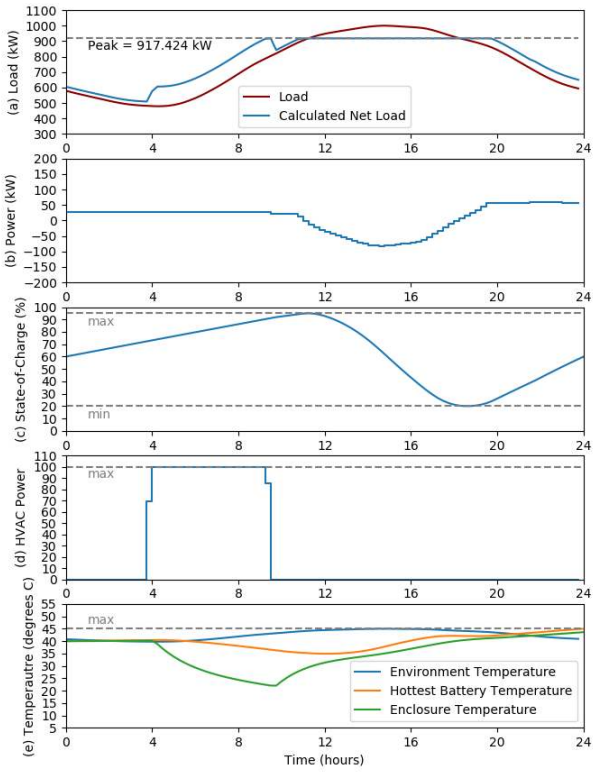

FIGURE 25. Results from control incorporating temperature model: (a) net load with BESS power control, (b) battery power, (c) battery SoC, (d) enclosure ac power, and (e) battery, enclosure, and environmental temperatures.

V. DEGRADATION MODELS

As batteries age with time and use, their energy storage and supply capabilities degrade until they no-longer meet the requirements of their designed services. When degradation is included in optimal control, it tends to rely on empirical degradation models that abstract many of the physical processes in favor of model simplicity. However, there are several studies that use the SPM or a simplified P2D to incorporate physical degradation models into a controller design [46], [81], [110]–[113].

This section first establishes definitions for state-of-health (SoH) and how they fit into optimal control. We then introduce and assess empirical stress factor based models for accurate degradation modeling. Linearizing and simplifying the detailed empirical degradation model allows us to calculate several norm-based regularization factors that efficiently incorporate degradation into optimal control objectives. Last, we cover physical degradation models based on intercalation stresses and two different side-reactions in lithium-ion batteries.

We use the terminology beginning-of-life (BoL) to denote the conditions when the battery is new, end-of-life (EoL) to denote the conditions when the battery can no-longer reliably supply energy services, and state-of-life (SoL) to denote the conditions, between BoL and EoL, that the battery is in at a given state. The EoL conditions are often specified by the battery or BESS manufacturer as a part of a warranty. Because of this lack of standardization, SoH can be defined in many ways (e.g., based on changes in capacity [114], resistance, round trip efficiency, etc.). We use a more general definition of SoH (ϱ), represented in:

$$\varrho = 1 - \left| \frac{y_{BoL} - y_{SoL}}{y_{BoL} - y_{EoL}} \right| \tag{57}$$

where ϱ is the SoH of the battery and y is a critical parameter for the battery to reliably supply services. In (57), SoH is defined as the ratio of a specific parameter's (or combination of parameters) movement from its initial state

at BoL to its final state at EoL. In this context, SoH can represent movement in energy capacity (kWh), available energy (kWh), charge capacity (Ah), available active material (e.g. through ''loss-of-lithium'' in mols), coulombic efficiency (%), or internal resistance (Ω). Available energy is a combination of available charge/discharge power, and energy capacity that is defined very precisely in the electric vertical context [114] but analogs can be imagined for energy storage applications as well. Using this definition, no matter what parameter is used, and whatever the BoL and EoL conditions are specified, ϱ at BoL always equals 1, and ϱ at EoL always equals 0. As we are focused on controller design, this definition does not account for ''rejuvenation'' cycles wherein lead-acid and some types of flow batteries can recover some loss of SoH.

For the purposes of control design, we can assume that the change in model parameters from degradation over any forward-looking control horizon is extremely small. That is, absolute changes in parameters from degradation happen over the course of months or even years, while controllers operate over hours or days. For this reason, from the perspective of control design, it is unimportant which parameter is used to calculate SoH. The rate of degradation, in contrast, can change quickly and is a critical factor in determining optimal control. Hence, rather than modeling SoH, we model the rate of degradation directly as a calculated variable.

There are at least two ways to incorporate the rate of degradation into optimal control design. The first way is to add incremental battery replacement/refurbishment cost in the objective [30]. The second method is to constrain operation to a maximum degradation rate to ensure a warranty period [28]. The following is a detailed introduction to these two methods.

When batteries reach EoL, they can be replaced with new batteries that restore the system's functionality to BoL conditions. In certain cases, the old batteries can be resold/re-purposed in a new application. The net costs predicted to be incurred at EoL, denoted by $\mathrm{C}_{\mathrm{EoL}}$, provide a quantitative estimate of how much the controller should weight battery degradation. The cost incurred through battery degradation is calculated in:

$$f_{\mathrm{b}} = \mathrm{C}_{\mathrm{EoL}} \frac{\partial \varrho}{\partial t} = \mathrm{C}_{\mathrm{EoL}} \dot{\varrho} \tag{58}$$

where f_{b} is the cost of the battery degradation over a full control horizon, $\mathrm{C}_{\mathrm{EoL}}$ is the net cost at EoL, ϱ is the present SoH, and $\dot{\varrho}$ is the average degradation rate over the control horizon.

As the cost incurred in (58) is the present value of a predicted future cost, it is possible to apply a discount rate based on an assumed interest rate. The number of compounding periods would then be estimated linearly from the current SoH, the average rate of degradation, and an assumed compound period, as shown in:

$$f_{\mathrm{b}} = (1+\mathfrak{i})^{-\mathfrak{n}} \mathrm{C}_{\mathrm{EoL}} \dot{\varrho} \tag{59a}$$

$$\mathfrak{n} = \left(\frac{1}{t_{\mathrm{comp}}}\right) \frac{\varrho}{\dot{\varrho}} \tag{59b}$$

where $\mathfrak{i}$ is the interest rate, $\mathfrak{n}$ is the number of compounding periods between SoL and EoL, and t_{comp} is the duration of each compounding period. This is meant to illustrate only one of many methods available for discounting future cost. It is sensible that control design using this method reflects whatever financial structure and assumptions are used for projected EoL costs.

Alternatively, a controller can be designed to maximize value while enforcing a designed or warranted service life. This method does not include an additional cost term in the objective and instead includes an additional constraint on the average rate of degradation, as shown in:

$$\dot{\varrho} \geq -\frac{\varrho}{L_{\mathrm{war}} - L} \tag{60}$$

where L_{war} is the total warranty life (e.g., 15 years), and L is the current life (years that the BESS has been in service). Critically, the degradation rate should be allowed to temporarily exceed the rate at which the BESS would reach EoL before the warranted service life as this allows for periods of rest to counterbalance period of high utilization. If this method is used, it is important to account for how the controller should transition operation past EoL as (60) is infeasible if $L \geq L_{\mathrm{war}}$. Note that (60) can be imposed as a soft constraint, with a slack variable subtracted from the limit and maximized in the objective. This approach can handle infeasibility at the expense of additional decision variables, which can be helpful when more complex degradation models are used.

A useful reformulation of this is for a manufacturer to supply a ''warranty life curve'' as shown in Fig. 26. This curve has a maximum warranty life and a function that describes how the warranty period would be shortened based on BESS operation increasing a supplied degradation metric (e.g., cycles as in [115]). This curve may or may not be accompanied by an equation to calculate the degradation metric as it is often described by just a few points to prevent reverse engineering. The warranty life can be interpreted in the context of control as the reciprocal of the rate of degradation, as in:

$$\dot{\varrho} = -\frac{1}{\mathfrak{D} L_{\mathrm{war}}} \geq -\frac{\varrho}{L_{\mathrm{war}} - L} \tag{61}$$

where $\mathfrak{D} : \mathbb{R} \mapsto \mathbb{R}$ is the warranty life curve supplied by the battery or BESS manufacturer. This formulation allows a generic warranty life curve to be implemented as a constraint into a BESS controller.

This section outlines various models for calculating the average rate of degradation for use in optimization. We adapt a stress factor model used for life prediction of lithium-ion cells for use in control design. We then illustrate how, through a series of operational assumptions, this stress factor model can be reduced to simple norm-based regularization. Last, we introduce several physical degradation models. Table 12 shows a summary of the types of degradation models discussed in the following sections.

TABLE 12. Summary of Degradation models.

Model Type	Measurable Variables	Calculated Variables	Parameters	Advantages	Disadvantages	References
ℓ_1 Power regularization[1]	•	$\dot{\varrho}$	C_{EoL}, L_{cyc},	simple convex reformulation, can be applied to ERM	assumptions: static cycle DoD, average SoC, cell temperature, and time horizon	[28], [30], [116]
ℓ_2 Power regularization[1]	•	$\dot{\varrho}$	C_{EoL}, K_T	simple convex epigraph reformulation, can be applied to ERM	assumptions: static cycle DoD, average SoC, cell temperature, number of cycles, and time horizon	
ℓ_1 Current regularization[2]	•	$\dot{\varrho}$	C_{EoL}, L_{cyc},	simple convex reformulation	assumptions: static cycle DoD, average SoC cell temperature, and time horizon	[46], [51], [74]
ℓ_2 Current regularization[2]	•	$\dot{\varrho}$	C_{EoL}, K_T	simple convex epigraph reformulation	assumptions: static cycle DoD, average SoC, cell temperature, number of cycles, and time horizon	[117]–[119]
ℓ_1 SoC regularization[1]	•	$\dot{\varrho}$	C_{EoL}, K_ς,	simple convex reformulation	assumptions: static cycle DoD, cell temperature, number of cycles, and time horizon	
ℓ_∞ DoD regularization[1]	•	$\dot{\varrho}$	C_{EoL}, K_{DoD}	simple convex reformulation	assumptions: static cell temperature, and time horizon, can only be applied accurately to one cycle at a time.	[120]
Rainflow cycle-counting stress factor model[3]	•	$\dot{\varrho}$, S_t,S_ς, S_T, S_δ, f_d	k_t, k_ς, ς_{ref}, k_T, T_{ref}, $k_{\delta 1}$, $k_{\delta 2}$, $k_{\delta 3}$	accurate predictor of SoH, no assumptions about static operating conditions, convex if stress factors are convex	must either discretize SoC, temperature, and current or use a subgradient solver before application in optimal control, high computational burden, assumes operational windows for DoD, SoC, and temperature	[52], [101], [120]–[126]
SEI layer formation model[5]	•	$\dot{\varrho}$, J_{SEI}, η_n, Φ_n, δ_{SEI}, L_{SEI}	n_{SEI}, k_{SEI}, D_{SEI}, M_{SEI}, ρ_{SEI}, $A_{s,n}$	physical salience, accounts for accelerated degradation from increased temperature	difficult to isolate from other physical degradation mechanisms, only applies to lithium based battery chemistries	[46], [110], [127]–[129]
Lithium-plaiting model[4]	•	$\dot{\varrho}$, η_{sr}, J_{sr}, $x_{s,n,surf}$, $L_{l.p.}$	Φ_{sr}, R_{film}, k_{sr}, α_{sr}, $C_{l.p.}$, $L_{l.p.,EoL}$	physical salience, can be avoided entirely by constraining $\eta_{sr} \geq 0$	difficult to isolate from other physical degradation mechanisms, not accurate model for degradation in performance if used on its own, only applies to lithium based battery chemistries	[81], [111]
Intercalation stress model[4]	•	$\dot{\varrho}$, σ_r, σ_t, L_{stress}	Ω_n, E_n, v_{poi}, $L_{stress,EoL}$	physical salience, applies to many battery chemistries	difficult to isolate from other physical degradation mechanisms, added complexity is proportional to number of particle volumes modeled in the SPM or P2D	[112], [113], [130], [131]

[1] Requires at least ERM SoC model from Section III-A
[2] Requires at least CRM SoC model from Section III-B
[3] Requires CRM SoC model and a temperature model from Sections III and IV
[4] Requires at least SPM SoC model from Section III-C
[5] Requires SPM SoC model and a temperature model from Sections III-C and IV

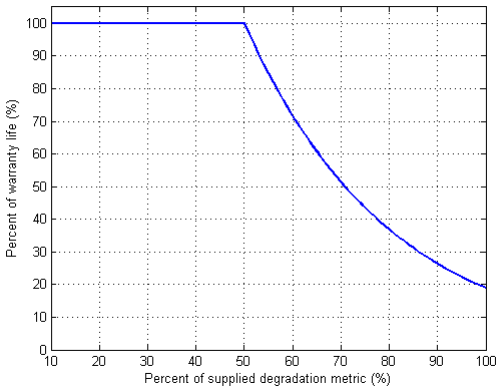

FIGURE 26. Notional example of a manufacturer supplied degradation curve (curve value = $\mathfrak{D}$).

A. EMPIRICAL DEGRADATION MODELS

Empirical battery degradation models can be classified as either calendar aging or cycle aging, with total degradation being the superposition of the two [132]. Calendar aging models are functions of time, average SoC, and average temperature and impact SoH whether or not the battery is charged or discharged. Cycle aging models are based on cycle SoC, current, cycle depth-of-discharge (DoD), and cycle temperature. Models based on current (or C-rate), such as the models presented in [133] and [134], generally work best for constant current cycling performed in laboratory experiments and have unknown accuracy in application that require variable charge or discharge rates.

It is common to represent degradation based on an exponential decay function of calendar and cycle degradation [121], as shown in:

$$\varrho = e^{-f_d} \tag{62}$$

where f_d is the aggregate degradation stress factor based on a combination of calendar life stress factors, and cycle life

stress factors. We can model the value of the aggregate degradation stress factor as an additional variable in our system representation.

A rainflow cycle counting algorithm originally developed for material degradation [135] is widely used for accurate cycle-life modeling [52], [122], [123]:

$$\mathfrak{f}_\mathrm{d} = S_\mathrm{t}\, S_\varsigma\, S_\mathrm{T} + \sum_{i=1}^{N} w_i S_\delta\, S_\varsigma\, S_\mathrm{T} \tag{63}$$

where N is the number of cycles in the control horizon, i is a cycle index variable, w_i is a binary variable indicating a full cycle or a partial cycle, and each stress factor is shown in:

$$S_\mathrm{t} = k_\mathrm{t}\, t \tag{64}$$

$$S_\varsigma = e^{k_\varsigma(\varsigma - \varsigma_\mathrm{ref})} \tag{65}$$

$$S_\mathrm{T} = e^{k_\mathrm{T}(T - T_\mathrm{ref})\frac{T_\mathrm{ref}}{T}} \tag{66}$$

$$S_\delta = a\,\delta^4 + b\,\delta^3 + c\,\delta^2 + d\,\delta + e \tag{67}$$

where t is time, S_t is the time stress factor, ς is SoC, S_ς is the SoC stress factor, T is temperature, S_T is the temperature stress factor, δ is DoD, and S_δ is the DoD stress factor. The parameters T_ref, ς_ref, k_t, k_ς, k_T, a, b, c, d, and e enable their associated stress factors to be tuned to specific batteries. Degradation models that do not use rainflow cycle counting often make duty-cycle profile assumptions such as in [136], [137].

Here we could extend the short board and cell-by-cell modeling approaches introduced in Section III-B to the distribution of degradation rates within a battery string or pack. However, from a control perspective, representing the maximum and minimum SoH in a string is less critical than for either SoC or Temperature because particularly low SoH cells can be replaced during regular maintenance, and hence would not limit operation. For this reason, the "big cell" representation of string level degradation is generally the most appropriate for optimal control applications.

As the controller objective is to minimize the change in SoH, we can take the derivative of (62) to obtain:

$$\dot{\varrho} = -\frac{\partial \mathfrak{f}_\mathrm{d}}{\partial t}\, e^{-\mathfrak{f}_\mathrm{d}} = -k_\mathrm{t}\, S_\varsigma\, S_\mathrm{T}\, e^{-\mathfrak{f}_\mathrm{d}} \tag{68}$$

yielding the form of SoH used in a controller model. Modeling SoH in this way presents a fundamental challenge. The rainflow counting algorithm in (63) is recursive in that, under most conditions, we cannot determine the number or time of each cycle within an schedule. When performing a rainflow counting algorithm on a known schedule, the schedule is broken into many smaller pieces that add up to the total degradation. However, this schedule splitting cannot be done a priori and hence is very difficult for optimization algorithms to work with. We discuss three imperfect workarounds and one apparent solution to this problem. First, there are some cases where the time windows for each cycle are predetermined (e.g., daily cycling). This makes the rainflow counting algorithm trivially simple and easy to implement in optimization. However, under some circumstances, the optimal solution, assuming only one cycle, yields two or more cycles. Similarly, the optimal solution assuming two cycles can often yield an optimal schedule that includes just one cycle, or cycles with different boundaries than expected. The second approach is to discretize the control schedule as demonstrated in [115], [124]. By breaking the available range of SoC and current into a number of discrete states it allows the controller to map each state transition onto a piecewise linearized degradation curve. This approach has the benefit of accuracy of the degradation function at the cost of precision of the control solution and computation time. The third workaround is to linearize the degradation rate around assumed static operational conditions, including cycles. Doing this, it can be found that the rate of degradation can be written in the form of a regularization term. This third approach is discussed in the following section. Lastly, an apparent solution is presented by Shi et al, who first prove the convexity of the rainflow counting algorithm and then demonstrate a subgradient algorithm for efficient optimal control [125]. This method works by recognizing that every charge (and discharge) action belongs to either one charge half cycle or two charge half cycles if it is at the time boundary between two cycles. The cost of a charge action at the boundary can be mapped from the cycle depth of either of its member half cycles. Hence the subgradient algorithm can avoid the calculation of the number of cycles entirely, instead adding the cost associated with the member half cycle to the subgradient of the charge action.

1) DEGRADATION AS REGULARIZATION

In machine learning, regularization is commonly used to prevent a model from overfitting data. Here we use similar methods to prevent our controller from over-using batteries. In this section we derive several different kinds of regularization terms based on the stress factors described above. While most of the degradation stress factors are nonlinear functions, their first-order Taylor series approximations can be reformulated as the norms of specific decision variables.

The simplest approach to calculating the rate of degradation ($\dot{\varrho}$) is to linearize it to an assumed cycle depth-of-discharge, temperature, and average SoC. Under these assumptions, the degradation rate can be written:

$$\dot{\varrho} = \frac{|p_\mathrm{e}|}{(1 + \frac{1}{\eta_\mathrm{e}})L_\mathrm{cyc} Q_\mathrm{cap}} \tag{69}$$

$$\dot{\varrho} = \frac{|i_\mathrm{bat}|}{(1 + \frac{1}{\eta_\mathrm{c}})L_\mathrm{cyc} C_\mathrm{cap}} \tag{70}$$

where p is BESS ac real power, i_bat is the battery current, η_c is the coulombic efficiency, L_cyc is the rated cycle-life to EoL, Q_cap is the energy capacity, and C_cap is the charge capacity. Under these narrow conditions, degradation is proportional to the absolute value of the battery power as shown in (69) when using the ERM [28], [30], [116], [138] or to the absolute value of the battery current as shown in (70) when using the CRM [46], [74]. A modification to this approach is to

establish a power or current threshold above which the linear cost increases as in [33]. Another modification is to multiply the absolute value of power or current by a stress factor based on temperature and charge/discharge rate as in [51], [116]. Note that, when adding (69) or (70) up over a discrete control horizon, this form of degradation is equivalent to applying a ℓ_1 norm power regularization, or ℓ_1 norm current regularization, as shown in:

$$f_{\mathrm{b}}(\mathbf{p}) = \Pi_{\mathrm{cyc}} ||\mathbf{p}||_1 \tag{71a}$$

$$\Pi_{\mathrm{cyc}} = \frac{\Delta t \, \mathrm{C}_{\mathrm{EoL}}}{(1 + \frac{1}{\eta_{\mathrm{e}}}) L_{\mathrm{cyc}} Q_{\mathrm{cap}}} \tag{71b}$$

$$f_{\mathrm{b}}(\mathbf{i}_{\mathrm{bat}}) = \Pi_{\mathrm{cyc}} ||\mathbf{i}_{\mathrm{bat}}||_1 \tag{72a}$$

$$\Pi_{\mathrm{cyc}} = \frac{\Delta t \, \mathrm{C}_{\mathrm{EoL}}}{(1 + \frac{1}{\eta_{\mathrm{c}}}) L_{\mathrm{cyc}} C_{\mathrm{cap}}} \tag{72b}$$

The regularization weight Π_{cyc} has units of \$/kW or \$/A depending on which equation it is in because of the units of the relevant decision variable.

At an assumed static temperature, the derivative of degradation rate with respect to temperature is constant (K_{T}) as shown in (73). Ignoring the reversible heat generation, overpotential heating, and assuming that battery temperature and environmental temperature are very close, the derivative of temperature in (50) reduces to simply the resistive heating term, as in:

$$K_{\mathrm{T}} = \frac{\partial^2 \varrho}{\partial T \, \partial t} = \frac{\partial}{\partial T} \left(-\dot{f}_{\mathrm{d}} \, e^{-\mathrm{f_d}} \right) \Bigg|_{\substack{T=T_0 \\ t=t_0 \\ \delta=\delta_0 \\ \varsigma=\varsigma_0}} \tag{73}$$

$$\frac{\partial T}{\partial t} = \frac{R_0}{C_{\mathrm{T}}} i_{\mathrm{bat}}^2 \tag{74}$$

where K_{T} is the partial derivative of degradation rate with respect to temperature, T is the battery temperature, t is time, R_0 is the battery ohmic resistance, and C_{T} is the battery's total heat capacity. From (73) and (74), we obtain the second derivative of degradation:

$$\ddot{\varrho} = \frac{K_{\mathrm{T}} R_0}{C_{\mathrm{T}}} i_{\mathrm{bat}}^2 \tag{75}$$

Assuming piecewise constant values for current, integrating (75) yields an approximation of the average degradation rate:

$$\dot{\varrho} \approx \frac{\Delta t K_{\mathrm{T}} R_0}{C_{\mathrm{T}}} ||\mathbf{i}_{\mathrm{bat}}||_2^2 \tag{76}$$

Again note that, when added up over the control horizon, this form of degradation is equivalent to applying a ℓ_2 norm-squared current regularization to the objective function as shown in:

$$f_{\mathrm{b}}(\mathbf{i}_{\mathrm{bat}}) = \Pi_{\mathrm{T}} ||\mathbf{i}_{\mathrm{bat}}||_2^2 \tag{77a}$$

$$\Pi_{\mathrm{T}} = \frac{\Delta t^2 \mathrm{C}_{\mathrm{EoL}} K_{\mathrm{T}} R_0}{C_{\mathrm{T}}} \tag{77b}$$

where the regularization weight Π_{T} in this equation has units of \$/A^2. This form of degradation cost has been used in [117]–[119] to minimize heat generation in hybrid vehicle energy management optimization.

Further, assuming a constant battery voltage ($v_{\mathrm{bat}} = v_0$), (77) can be reformulated using ac power instead of dc current. Assuming the ac/dc conversion model in (24), with $\phi_{\mathrm{b}} = 0$, the minimum heat generation regularization is shown in:

$$f_{\mathrm{b}}(\mathbf{p}) = \Pi_{\mathrm{T}} ||\mathbf{p}||_2^2 \tag{78a}$$

$$\Pi_{\mathrm{T}} = \frac{\Delta t^2 \mathrm{C}_{\mathrm{EoL}} K_{\mathrm{T}} R_0 \phi_{\mathrm{m}}^2}{C_{\mathrm{T}} v_0} \tag{78b}$$

where the regularization weight Π_{T} in this equation has units of \$/kW^2.

At an assumed static average SoC (ς_{avg}), the the derivative of the degradation rate with respect to average SoC is constant, as shown in:

$$\varsigma_{\mathrm{avg}} = \frac{||\boldsymbol{\varsigma}||_1}{n} \tag{79}$$

$$K_{\varsigma} = \frac{d^2 \varrho}{d \varsigma_{\mathrm{avg}} \, dt} = \frac{\partial}{\partial \varsigma_{\mathrm{avg}}} \left(-\dot{f}_{\mathrm{d}} \, e^{-\mathrm{f_d}} \right) \Bigg|_{\substack{T=T_0 \\ t=t_0 \\ \delta=\delta_0 \\ \varsigma=\varsigma_0}} \tag{80}$$

where K_{ς} is the partial derivative of degradation rate with respect to SoC, ς_{avg} is the average SoC, and n is the number of steps in the discrete control horizon. Multiplying both sides by $\partial \varsigma_{\mathrm{avg}}$ and, assuming piecewise constant values for SoC, integrating yields an approximation for the average degradation rate:

$$\dot{\varrho} \approx \frac{K_{\varsigma}}{n} ||\boldsymbol{\varsigma}||_1 \tag{81}$$

This form of degradation is equivalent to applying a ℓ_1 norm SoC regularization to the objective function as shown in:

$$f_{\mathrm{b}}(\boldsymbol{\varsigma}) = \Pi_{\varsigma} ||\boldsymbol{\varsigma}||_1 \tag{82a}$$

$$\Pi_{\varsigma} = \frac{\Delta t \, \mathrm{C}_{\mathrm{EoL}} K_{\varsigma}}{n} \tag{82b}$$

where the regularization weight Π_{ς} in this equation has units of \$/(%SoC).

At an assumed static cycle DoD, the derivative of degradation rate with respect to DoD is constant, as shown in:

$$\delta = \max(\boldsymbol{\varsigma}) - \min(\boldsymbol{\varsigma}) = ||\boldsymbol{\varsigma}||_\infty + ||\mathbf{1} - \boldsymbol{\varsigma}||_\infty - 1 \tag{83}$$

$$K_{\mathrm{DoD}} = \frac{\partial^2 \varrho}{\partial \delta \, \partial t} = \frac{\partial}{\partial \delta} \left(-\dot{f}_{\mathrm{d}} \, e^{-\mathrm{f_d}} \right) \Bigg|_{\substack{T=T_0 \\ t=t_0 \\ \delta=\delta_0 \\ \varsigma=\varsigma_0}} \tag{84}$$

where K_{DoD} is the partial derivative of degradation rate with respect to DoD, and δ is the DoD. Multiplying both sides by $\partial \delta$ and, assuming piecewise constant values for SoC, integrating yields an approximation for the average degradation rate:

$$\dot{\varrho} \approx K_{\mathrm{DoD}} \delta = K_{\mathrm{DoD}} \left(||\boldsymbol{\varsigma}||_\infty + ||\mathbf{1} - \boldsymbol{\varsigma}||_\infty - 1 \right) \tag{85}$$

This form of degradation is equivalent to applying an ℓ_∞ norm ς and $1 - \varsigma$ regularization to the objective function as shown in:

$$f_{\mathrm{b}}(\boldsymbol{\varsigma}) = \Pi_{\mathrm{DoD}} \left(||\boldsymbol{\varsigma}||_\infty + ||\mathbf{1} - \boldsymbol{\varsigma}||_\infty \right) \tag{86a}$$

$$\Pi_{\text{DoD}} = \text{C}_{\text{EoL}} K_{\text{DoD}} \tag{86b}$$

Note that the -1 can be omitted from ς_{DoD} in this formulation because, as a constant, it would not affect the minimizers of the optimization. This degradation cost has been applied to BESS in a daily energy market arbitrage application [120]. The regularization weight Π_{DoD} in this equation has units of \$/(%DoD).

Now that the partial derivatives have each been derived, we can combine them to yield a function for total degradation. As the current based cycle-counting and heat-generation degradation functions require fewer assumptions than their ac power based counterparts, we use (72a) and (77) instead of (71) and (78) though either option produces a viable estimate of total degradation. The formulation for linearized total degradation cost is shown in:

$$\begin{aligned} f_{\text{b}}(\mathbf{i}_{\text{bat}}, \boldsymbol{\varsigma}) = \Pi_{\text{cyc}} ||\mathbf{i}_{\text{bat}}||_1 + \Pi_{\text{T}} ||\mathbf{i}_{\text{bat}}||_2^2 + \Pi_{\varsigma} ||\boldsymbol{\varsigma}||_1 \\ + \Pi_{\text{DoD}} \left(||\boldsymbol{\varsigma}||_\infty + ||\mathbf{1} - \boldsymbol{\varsigma}||_\infty \right) \end{aligned} \tag{87}$$

B. PHYSICAL DEGRADATION MODELS

Physical degradation models have already been reviewed in [85], [139], [140]. These models are built on top of the concentration-based SoC model type discussed in Section III-C. As with empirical models, physical degradation models can emphasize calendar aging [141] or cycle aging [142]. However, a better classification is to distinguish models that focus on chemical side-reactions [129], [141]–[145] or material fatigue [112], [131]. Rather than duplicating a review of all the models available, the rest of this section analyzes the narrower intersection between physical degradation modeling and optimal control.

In lithium-ion batteries, which are the primary focus of research on degradation mechanisms, the formation of the solid electrolyte interphase (SEI) layer both increases resistance and reduces the available lithium resulting in both power and capacity fade [110]. The current density of the side-reaction that leads to the growth of the SEI layer [46], [127], [128] is shown in:

$$J_{\text{SEI}} = \frac{\exp\left(-\frac{F}{RT}\eta_n\right)}{\frac{1}{n_{\text{SEI}} F k_{\text{SEI}} \exp\left(\frac{n_{\text{SEI}} F}{RT}(\Phi_n - 0.4)\right)} - \frac{\delta_{\text{SEI}}}{n_{\text{SEI}} F D_{\text{SEI}}}} \tag{88}$$

where J_{SEI} is the SEI side-reaction current density, F is Faraday's constant, R is the ideal gas constant, T is the battery temperature, η_n is the negative electrode overpotential, n_{SEI} is the number of electrons in the SEI side-reaction, k_{SEI} is the chemical rate constant of the SEI side-reaction, Φ_n is the open circuit voltage of the negative electrode, δ_{SEI} is the thickness of the SEI layer, and D_{SEI} is the diffusion coefficient of lithium in the SEI layer.

If power is the critical parameter for operation, then we use the growth in the thickness of the SEI layer to calculate the rate of change in SoH as shown in:

$$\frac{\partial \delta_{\text{SEI}}}{\partial t} = \frac{J_{\text{SEI}} M_{\text{SEI}}}{n_{\text{SEI}} F \rho_{\text{SEI}}} \tag{89a}$$

$$\varrho_{\text{SEI}} = 1 - \frac{\delta_{\text{SEI}}}{\delta_{\text{SEI,EoL}}} \tag{89b}$$

where M_{SEI} is the molar volume of SEI reaction products,and ρ_{SEI} is the density of the SEI layer. It should be noted that there are many other ways of modeling the growth of the SEI layer [129].

If capacity is the critical parameter for operation, then we use the loss-of-lithium to calculate the rate of change in SoH as shown in:

$$\frac{\partial L_{\text{SEI}}}{\partial t} = J_{\text{SEI}} A_{s,n} \tag{90a}$$

$$\varrho_{\text{SEI}} = 1 - \frac{L_{\text{SEI}}}{L_{\text{SEI,EoL}}} \tag{90b}$$

where L_{SEI} is the lost lithium content, and $A_{s,n}$ area of the negative electrode.

Another side-reaction to consider is lithium-plating, which can occur under adverse charging conditions or as a result of accidental overcharge [81], [111]. In this case, the rate of change in SoH can be calculated as the magnitude of the side-reaction over-potential if it is negative as shown in:

$$\eta_{\text{sr}} = \phi_{1,n} - \phi_{2,n} - \Phi_{\text{sr}} - F J_{\text{sr}} R_{\text{film}} \tag{91}$$

$$J_{\text{sr}} = k_{\text{sr}} (x_{s,n,\text{surf}})^{\alpha_{\text{sr}}} \tag{92}$$

$$\times \left\{ \exp\left(\frac{(1-\alpha_{\text{sr}})F}{RT} \eta_{\text{sr}} \right) - \exp\left(-\frac{\alpha_{\text{sr}} F}{RT} \eta_{\text{sr}} \right) \right\} \tag{93}$$

$$\frac{\partial L_{\text{l.p.}}}{\partial t} = C_{l.p.} |\min(\eta_{\text{sr}}, 0)| \tag{94}$$

where η_{sr} is the side-reaction overpotential, $\phi_{1,n}$ is the solid-phase potential, $\phi_{2,n}$ is the solution-phase potential, η_n is the anode overpotential, calculated using the Butler-Volmer equation (37), Φ_{sr} is the side reaction reference voltage, which can be conservatively estimated to be zero in this case [81], [111], J_{sr} is the side-reaction current density, R_{film} is the lithium metal film resistance, k_{sr} is the side-reaction rate constant $x_{s,n,\text{surf}}$ is the surface concentration of lithium divided by the maximum concentration, α_{sr} is the side-reaction transfer coefficient, $C_{l.p.}$ is the ratio between negative magnitude of η_{sr} and the quantity of lithium-plaiting, $L_{\text{l.p.}}$ is a quantitative measure of the accumulated lithium plaiting, and $L_{\text{l.p.,EoL}}$ is the lithium-plaiting limit at EoL. Authors in [81] simplify this by assuming that R_{film} is zero, meaning that $\eta_{\text{sr}} = \eta_n - \Phi_n$. Alternatively, a controller can be configured to prevent this side-reaction entirely by constraining η_{sr} to be non-negative as shown in:

$$\eta_{\text{sr}} \geq 0 \tag{95}$$

A controller can be designed to minimize intercalation-induced fatigue [112], [113]. Intercalation-induced fatigue occurs in many battery chemistries, including lithium-ion, and so this mechanism is more general than the side-reactions discussed above. The radial and tangential intercalation

stresses in a spherical partial can be calculated as shown in:

$$\frac{3\,\sigma_r(r)}{\left(\frac{\Omega_n E_n c_{n,max}}{(1-\nu_{\text{poi}})}\right)} = \frac{2}{3}\left(\int_0^1 x_{s,n}(r) r^2 dr - \frac{1}{r^3}\int_0^r x_{s,n}(r) r^2 dr\right) \tag{96a}$$

$$\frac{3\,\sigma_t(r)}{\left(\frac{\Omega_n E_n c_{n,max}}{(1-\nu_{\text{poi}})}\right)} = 2\left(\int_0^1 x_{s,n}(r) r^2 dr + \frac{1}{r^3}\int_0^r x_{s,n}(r) r^2 dr - x_{s,n}(r)\right) \tag{96b}$$

$$\frac{\partial L_{\text{stress}}}{\partial t} = \max_{r\in[0,\bar{r}_n]}\{\sigma_r(r), \sigma_t(r)\} \tag{96c}$$

$$\varrho_{\text{stress}} = 1 - \frac{L_{\text{stress}}}{L_{\text{stress,EoL}}} \tag{96d}$$

where σ_r is the radial intercalation stress, σ_t is the tangential intercalation stress, $c_{n,max}$ is the maximum concentration of lithium in the negative electrode, Ω_n is the partial molar volume, E_n is Young's modulus, ν_{poi} is Poisson's ratio, $x_{s,n}$ is the normalized concentration in the negative electrode, r is the radial distance, L_{stress} is the accumulated stress, and $L_{\text{stress,EoL}}$ is the accumulated stress limit at EoL.

It can be difficult to know how these physical degradation mechanisms combine. Each have been shown to be accurate on their own, meaning that simply adding them would overestimate the rate of degradation. One method is to calculate a weighted combination of degradation factors as shown in:

$$\dot{\varrho} = \frac{\alpha_\varrho \dot{\varrho}_{\text{stress}} + \beta_\varrho \dot{\varrho}_{\text{stress}} + \gamma_\varrho \dot{\varrho}_{\text{stress}}}{\alpha_\varrho + \beta_\varrho + \gamma_\varrho} \tag{97}$$

where α_ϱ, β_ϱ, and γ_ϱ are unitless weights selected to linearly combine physical degradation mechanisms. However, degradation clearly does not follow simple superposition (e.g. intercalation stress and loss of lithium may have compounding effects) so this simplistic combination may be inaccurate. We are not aware of any experimental methods for isolating the effects of different physical degradation mechanisms and so selecting weights to combine them may be misleading.

C. DEGRADATION MODEL APPLICATION

For this application we solve the optimal control problem in Section II while incorporating the stress-factor degradation model with parameters listed in Table 13.

The rainflow, static-cycle model is the most appropriate for this problem given that there is one-cycle that takes the whole day, and a low time resolution so low computational burden. The modified objective and constraints, in addition to those for the CRM and temperature models defined in Sections III-B.1 and IV-C.1, are shown in:

$$\min_{\mathbf{x}_{\text{H}}\in\mathbb{R}^{9n+12}} \quad \Delta t\,\mathbf{w}^\top(\mathbf{l}+\mathbf{p}+\mathbf{p}_{\text{HVAC}}) + \nu\tau + \text{C}_{\text{EoL}}\dot{\varrho} \tag{98a}$$

subject to:

$$\vdots \text{ in addition to the constraints in (28) and (55)}$$

$$\dot{\varrho} = -k_{\text{t}}\,S_\varsigma\,S_{\text{T}}\,e^{-\text{f}_{\text{d}}} \tag{98b}$$

TABLE 13. Example battery system degradation model parameters.

Name	Symbol	Value
Thermal Degradation Constant	k_{T}	0.0693
Time Degradation Constant	k_{t}	1.49e-6
SoC Degradation Constant	k_ς	1.04
Reference SoC	ς_{ref}	50%
Reference Temperature	T_{ref}	25%
EoL Cost Assumed	C_{EoL}	-$800,000
Regularization weight	Π	1e-5

Polynomial Fit	a	b	c	d	e
DoD Stress Factor	5.7905	-6.8292	3.3209	5.3696 e-01	6.1638 e-02

Note: The parameters in [121] were used as a basis for the representative BESS presented here. The model parameters were modified to for use in Pyomo (in the case of the DoD Stress Factor being a polynomial), and to more clearly demonstrate the effect of degradation on controller action (in the case of k_{T} and k_ς). The DoD Stress Factor has be multiplied by five to represent a battery cell type with 1/5 the cycle life.

$$\text{f}_{\text{d}} = S_{\text{t}}\,S_\varsigma\,S_{\text{T}} + S_\delta\,S_\varsigma\,S_{\text{T}} \tag{98c}$$

$$S_{\text{t}} = k_{\text{t}}\,n\,\Delta t \tag{98d}$$

$$S_\varsigma = e^{k_\varsigma(\frac{||\boldsymbol{\varsigma}||_1}{n} - \varsigma_{\text{ref}})} \tag{98e}$$

$$S_{\text{T}} = e^{k_{\text{T}}(||\mathbf{T}||_1 - T_{\text{ref}})\frac{T_{\text{ref}}}{||\mathbf{T}||_1}} \tag{98f}$$

$$\delta = \max(\boldsymbol{\varsigma}) - \min(\boldsymbol{\varsigma}) \tag{98g}$$

$$S_\delta = a\,\delta^4 + b\,\delta^3 + c\,\delta^2 + d\,\delta + e \tag{98h}$$

where $\mathbf{x}_{\text{H}} = \{\mathbf{p}, \mathbf{p}_{\text{dc}}, \mathbf{i}_{\text{bat}}, \mathbf{v}_{\text{bat}}, \mathbf{v}_{\text{oc}}, \boldsymbol{\varsigma}, \tau, \mathbf{p}_{\text{HVAC}}, \mathbf{T}, \mathbf{T}_{\text{EN}}, \dot{\varrho}, \text{f}_{\text{d}}, S_{\text{t}}, S_\varsigma, S_{\text{T}}, \delta, S_\delta, \} \in \mathbb{R}^{9n+12}$, $\dot{\varrho} \in \mathbb{R}$ is the rate of degradation, $\text{f}_{\text{d}} \in \mathbb{R}$ is the degradation forcing function, $S_{\text{t}} \in \mathbb{R}$ is the time stress-factor, $S_\varsigma \in \mathbb{R}$ is the SoC stress-factor, $S_{\text{T}} \in \mathbb{R}$ is the temperature stress-factor, $\delta \in \mathbb{R}$ is the cycle depth-of-discharge (DoD), and $S_\delta \in \mathbb{R}$ is the DoD stress-factor.

The net load achieved using the combined SoC-Thermal-Degradation model is shown in Fig. 27 (a). The optimal control schedule calculated over the control horizon is shown in Fig. 27 (b). Observe that the period of high HVAC power in Fig. 27 (d), compared to the solution using only the SoC-Temperature model, simply shifts to the beginning of the control horizon. The resulting environmental, battery, and enclosure temperature trajectories are shown in Fig. 27 (e).

The control solution reduces the total electrical bill from $52,080 ($50,000 demand, $2,080 energy) to $48,006 ($45,871 demand, $2,135 energy). Within the energy bill, the energy required to cool the battery accounts for $56. The net effect is a $4074 (7.82%) reduction from the baseline electrical bill, or a $5 (0.01%) increase in the electrical bill calculated using only the charge and temperature models. The cost of degradation was reduced from $209, calculated by applying the degradation model to the schedule derived from the SoC-Temperature model application in Section IV-C.1, to $111 from this schedule (a 47% reduction in estimated degradation rate). Further, when compared to the solution calculated using only the SoC model in Section III-B.1, the cost of degradation was reduced from $897 to $111 (an 88% reduction). Again, these results are

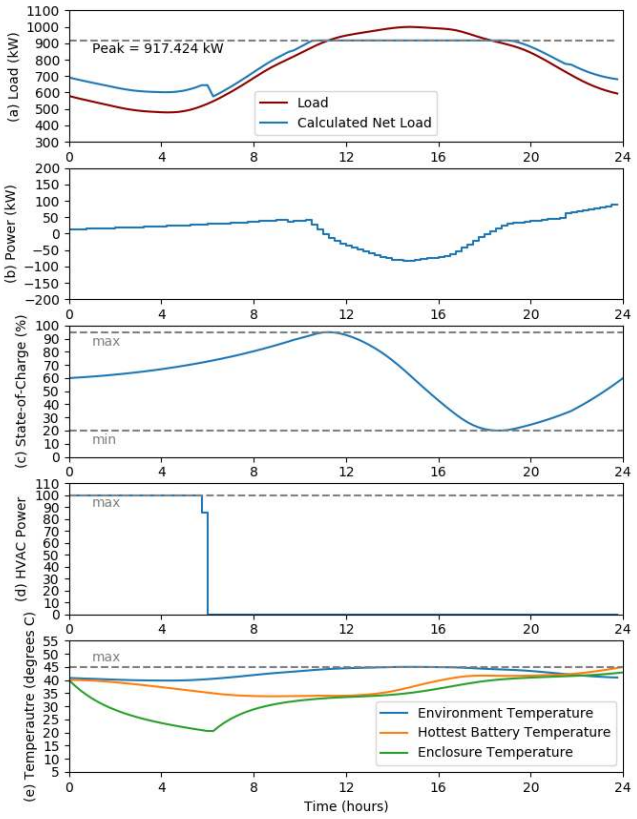

FIGURE 27. Results from control incorporating a degradation model: (a) net load with BESS power control, (b) battery power, (c) battery SoC, (d) enclosure ac power, and (e) battery, enclosure, and environmental temperatures.

highly conditional based on the specific BESS parameters. This analysis demonstrates that even small changes in control actions can have large impacts on the rate of degradation.

VI. DISCUSSION

Section III introduced several varieties of models for BESS SoC, with the primary classification distinguishing energy based models, charge based models, and concentration-based models. By applying all three to the same problem we can identify several differences in how controllers might work differently when operating with each type. Contrasting Fig. 7 and 11, we can observe that by accounting for the change in battery voltage, the CRM steadily increases power as SoC increases. The ERM does not model voltage and hence is imprecise in its estimates for how much power is needed to charge or available for discharge. In general, the ERM is best for use in large scale systems where a more detailed model would be impractical (e.g. centralized control of 1000's of individual BESS) or in very short duration problems that are insensitive to changes in voltage. The CRM and SPM are mathematically similar in structure, in that they both require empirical open-circuit-voltage functions and several internal storage elements in the form of either a equivalent circuit model or a partial concentration model. The CRM tends to simplify or combine many of the nuances of SPM type models, such as only using a single open-circuit-voltage function as opposed to one for the cathode and another for the anode. The SPM has the advantage of the ability to incorporate the physical degradation models, while the ERM and CRM must rely on empirical degradation models. To give a sense for the relative complexity of the model types, the minimal ERM has $3n + 2$ decision variables (were n is the number of time-steps), the minimal CRM has $6n + 2$, and the minimal SPM has $18n + 13$. Further, the ERM is convex, while the CRM and SPM have several non-convex constraints.

In Section IV we introduce three cell temperature models and two enclosure temperature models. The primary difference between the cell models is what heating and cooling mechanisms are considered, with another distinction being how many internal volumes are modeled. The enclosure models generally rely on an assumption of well-mixed air but can be classified based on how precisely they represent the HVAC system. As was demonstrated in the application section, by including the HVAC system in the control design the batteries can be pre-cooled to have maximum temperature margin during peak discharge when significant heat is being generated. Not accounting for temperature in control actions can lead to over-temperature shutdown or curtailment during peak times when the battery is needed most.

Lastly, Section V introduces several models to incorporate battery degradation into control decisions. Including degradation allows for charge/discharge to be balanced against how much the increase in use also accelerates degradation. A wide range of empirical degradation models is available that can be used on their own or in combinations to consider many different underlying mechanisms. Physical degradation mechanisms are less widely used but offer the potential to reduce the uncertainty of degradation modeling. Also, it can be observed from Fig. 27 that modeling the HVAC system and degradation together can have compounding benefits to prolonging battery life. Not accounting for degradation in control design allows batteries to operate in ways that could lead to premature EoL conditions. The following is a discussion of the gaps identified in the current state-of-the-art in models for optimal control of battery energy storage.

A. GAP IDENTIFICATION

This paper has focused on providing guidance for how and where to use different types of battery models for optimal control. In this section we take a broader perspective to understand the state-of-the-art more generally and identify opportunities for advancement.

1) REAL-WORLD DATA

There is a significant deficit of operational performance data in studies on optimal control of battery energy storage. This results in many of the modeling assumptions that proposed

controllers are based on having gone unchallenged. This gap emphasizes the importance of systematic data collection and publication in BESS demonstration projects.

2) CONTROL OF LARGE-SCALE PARALLEL AND SERIES COMBINATIONS OF BATTERIES

The 'big-cell' assumption is widely used to reduce the complexity of a large battery system to a manageable level. However, we do not know at what point the uncertainty of cell-to-cell variations outweighs the uncertainty from other modeling assumptions. Using a simpler model, with more representative cells, may yield better performance at a lower complexity than a highly precise battery model that assumes all cells behave the same. This trade-off is poorly understood even though it could greatly impact BESS performance.

3) RISK-AVERSE AND ROBUST CONTROL

While there exists a large body of experimental work quantifying the uncertainty of the different model types, this uncertainty is rarely incorporated into the battery controller design. Even many controllers that consider the uncertainty of renewable power, through risk-averse or robust control, fail to consider the uncertainty of the battery model's, implicitly assuming them to be deterministic systems.

4) NONLINEAR ERM

Nonlinear system dynamics can be integrated into ERM used in controller design to improve model accuracy. The degree to which this improved model accuracy improves optimal control is an under-explored branch of research.

5) VOLTAGE HYSTERESIS IN CONTROL

The path dependence of open circuit voltage can be a large contributor to error in SoC models. However, few controller designs consider hysteresis in their equivalent circuit, or solid-electrolyte interface voltage models. As these models are already nonlinear, and the optimal control problems are already non-convex, adding hysteresis should have minimal impact on computation time.

6) ENTROPY IN THERMAL MODELING

The electrochemical reaction in batteries can be exothermic or endothermic, depending on the specific chemistry and the SoC. While this concept is well understood in battery simulation, it is rare in optimal control. Incorporating the entropy-based heat generation and consumption into controllers could greatly reduce optimistic shortfall in many applications.

7) COMPARATIVE ANALYSIS OF EMPIRICAL DEGRADATION STRESS FACTORS

Battery degradation is a complex phenomenon to research. Cycling studies try and isolate the stress factors that accelerate aging, but many of these factors either can't be isolated or have nonlinear effects when combined with others. For example, charge/discharge current generates heat and leads to higher temperatures. A cycling study cannot fully isolate these variables because they are interlinked. Further, if battery degradation is a nonlinear function of both current and temperature, then a stress factor model that assumes independence will be inaccurate. The current direction of research on degradation models improves accuracy with increasing complexity, but controllers require computational efficiency and hence can make limited use of these improved methods. Research is needed to improve the accuracy of stress factor models that are simple enough to be incorporated into onboard controllers.

The literature intersecting battery energy storage modeling and optimal control is primarily simulation based with very little work that includes experimental analysis or real-world application. This is a natural result of the combination of battery energy storage technologies having tremendous potential to change grid operation, and only recently coming down in cost enough to the point where demonstration projects can proliferate. This means that there is significant academic interest while there are relatively few operational systems. A result of this lack of data is that there is little understanding of the impact of modeling assumptions on the design of controllers. Most of the gaps identified in the state-of-the-art stem from this lack of understanding. The remaining gaps can be summarized as an underdeveloped optimization framework. Stochastic optimization methods have been widely used in operation research to incorporate uncertainty into the optimization problem. This mathematical background has been underutilized in BESS controller design. With more data will come improvements in the understanding of uncertainty which can, in turn, be incorporated into optimal control approaches to achieve risk averse or robust control.

Broadly speaking, the field on optimal control of BESS is still nascent when compared to the markets and control systems for thermal generation systems. The most commonly used models (ERM) are a simplistic approximation of extremely complicated electrochemical systems. If we are to learn from the historical course of optimization of thermal generation, we can understand that simplistic models are normal at this stage of development. We may expect that these models will become more developed and accurate as time progresses, leading to greater utilization of BESS to supply services on the grid. Additionally, we might also expect that the models used to optimize energy storage within markets will be more abstract than the models used by individual systems to optimize their operation. Navigating the balance between the applications that desire model simplicity and applications that desire model accuracy will require ongoing research, especially given the accelerated pace of battery energy storage technology development.

VII. SUMMARY AND CONCLUSIONS

The choice of what model to use is critical in the design of optimal controllers for any physical system. This is especially true for electrochemical energy storage as we have shown

the wide range of physical mechanisms that impact batteries during operation. Understanding the assumptions that are implicit in the choice of battery models will help engineers and researchers to improve the design of optimal controllers in BESS serving the electric grid.

This paper thoroughly reviews battery models used for optimal control of BESS. We identify three broad types of SoC models: energy reservoir models (ERMs), charge reservoir models (CRMs), and concentration-based models that include both single partial models (SPMs) and pseudo two-dimensional (P2D) models. ERMs are computationally efficient and hence are more appropriate for the optimization of large fleets of BESS. However, ERMs can be inaccurate over wide operational ranges. CRMs, in contrast, are more computationally intensive but have the potential for better accuracy. An under-explored middle ground for these is a nonlinear ERM, that may provide improved accuracy with a modest increase in computational complexity. Concentration based models are significantly more complex than either ERM or CRM and include many parameters that may be considered proprietary by a battery manufacturer. As the concentration-based SPM has a similar mathematical structure to the CRM, it is unclear how much this increase in complexity yields increased predictive accuracy. The SPM has the distinct advantage of enabling the application of physical degradation models that may reduce modeling uncertainty.

When battery temperature can limit BESS control actions, it is important to include a temperature model in the controller. Heat is generated in a battery from joule heating, over potential heating, and thermodynamic entropy. While the impact of entropy can be significant, it is rarely calculated in control systems. Heat is transferred from the battery, or the battery's enclosure, to the environment through conduction, convection, or radiation. Representing these mechanisms in the controller model enables optimal cooling control that can efficiently enforce temperature limits and significantly reduce battery degradation.

Lastly, battery degradation can be critical to consider when making control decisions. Factors such as SoC, temperature, and DoD can stress the materials in batteries and cause degradation over time and use. The empirical rainflow cycle counting algorithm or physical degradation models for calculating degradation are both highly accurate but difficult to fully incorporate into an optimization problem. With a few simplifying assumptions, the stress factor model can be reduced to take the form of a sum of regularization terms in the objective function. These assumptions partially justify the more widely used formulations for degradation based on number of cycles, heat generation, and DoD. However, by including the nonlinear models in the controller, we observe that small changes in controller schedules can have disproportionate impacts on the rate of degradation. The myriad of tradeoffs between model complexity and model accuracy can be difficult to navigate, but these engineering decisions can offer significant benefits in terms of BESS controller performance.

ACKNOWLEDGMENT

This article describes objective technical results and analysis. Any subjective views or opinions that might be expressed in the article do not necessarily represent the views of the U.S. Department of Energy or the United States Government. SAND2019-14663 J.

REFERENCES

[1] A. A. Akhil, G. Huff, A. B. Currier, B. C. Kaun, D. M. Rastler, S. B. Chen, A. L. Cotter, D. T. Bradshaw, and W. D. Gauntlett, "DOE/EPRI 2013 electricity storage handbook in collaboration with NRECA," Sandia Nat. Laboratories, Albuquerque, NM, USA, Tech Rep. SAND2013-5131, Sep. 2013, [Online]. Available: http://www.sandia.gov/ess/publications/SAND2013-5131.pdf

[2] R. H. Byrne, T. A. Nguyen, D. A. Copp, B. R. Chalamala, and I. Gyuk, "Energy management and optimization methods for grid energy storage systems," *IEEE Access*, vol. 6, pp. 13231–13260, 2018, doi: 10.1109/ACCESS.2017.2741578.

[3] D. N. T. How, M. A. Hannan, M. S. H. Lipu, and P. J. Ker, "State of charge estimation for lithium-ion batteries using model-based and data-driven methods: A review," *IEEE Access*, vol. 7, pp. 136116–136136, 2019, doi: 10.1109/ACCESS.2019.2942213.

[4] B. Hredzak, V. G. Agelidis, and M. Jang, "A model predictive control system for a hybrid battery-ultracapacitor power source," *IEEE Trans. Power Electron.*, vol. 29, no. 3, pp. 1469–1479, Mar. 2014, doi: 10.1109/TPEL.2013.2262003.

[5] M. A. Xavier and M. S. Trimboli, "Lithium-ion battery cell-level control using constrained model predictive control and equivalent circuit models," *J. Power Sour.*, vol. 285, pp. 374–384, Jul. 2015, doi: 10.1016/j.jpowsour.2015.03.074.

[6] J. Donadee and J. Wang, "AGC signal modeling for energy storage operations," *IEEE Trans. Power Syst.*, vol. 29, no. 5, pp. 2567–2568, Sep. 2014, doi: 10.1109/tpwrs.2014.2301592.

[7] E. Perez, H. Beltran, N. Aparicio, and P. Rodriguez, "Predictive power control for PV plants with energy storage," *IEEE Trans. Sustain. Energy*, vol. 4, no. 2, pp. 482–490, Apr. 2013, doi: 10.1109/TSTE.2012.2210255.

[8] H. S. Ko and J. Jatskevich, "Power quality control of wind-hybrid power generation system using fuzzy-LQR controller," *IEEE Trans. Energy Convers.*, vol. 22, no. 2, pp. 516–527, Jun. 2007, doi: 10.1109/TEC.2005.858092.

[9] D. Rosewater, Q. Nguyen, and S. Santoso, "Optimal field voltage and energy storage control for stabilizing synchronous generators on flexible AC transmission systems," in *Proc. IEEE/PES Transmiss. Distrib. Conf. Expo. (TD)*, Apr. 2018, pp. 1–9, doi: 10.1109/TDC.2018.8440436.

[10] R. Klein, N. A. Chaturvedi, J. Christensen, J. Ahmed, R. Findeisen, and A. Kojic, "Electrochemical model based observer design for a lithium-ion battery," *IEEE Trans. Control Syst. Technol.*, vol. 21, no. 2, pp. 289–301, Mar. 2013, doi: 10.1109/TCST.2011.2178604.

[11] M. T. Lawder, B. Suthar, P. W. C. Northrop, S. De, C. M. Hoff, O. Leitermann, M. L. Crow, S. Santhanagopalan, and V. R. Subramanian, "Battery energy storage system (BESS) and battery management system (BMS) for grid-scale applications," *Proc. IEEE*, vol. 102, no. 6, pp. 1014–1030, Jun. 2014, doi: 10.1109/JPROC.2014.2317451.

[12] V. Ramadesigan, P. W. C. Northrop, S. De, S. Santhanagopalan, R. D. Braatz, and V. R. Subramanian, "Modeling and simulation of lithium-ion batteries from a systems engineering perspective," *J. Electrochem. Soc.*, vol. 159, no. 3, pp. R31–R45, 2012, doi: 10.1149/2.018203jes.

[13] T. A. Nguyen and R. H. Byrne, "Maximizing the cost-savings for time-of-use and net-metering customers using behind-the-meter energy storage systems," in *Proc. North Amer. Power Symp. (NAPS)*, Sep. 2017, pp. 1–6, doi: 10.1109/NAPS.2017.8107380.

[14] J. McLaren and S. Mullendore, "Identifying potential markets for behind-the-meter battery energy storage: A survey of U.S. demand charges," Nat. Renew. Energy Lab., Denver, Co, USA, Tech. Rep. nREL/BR-6A20-68963., Aug. 2017, [Online]. Available: https://www.nrel.gov/docs/fy17osti/68963.pdf

[15] EPRI OpenDSS Test Circuits. *Ckt5 Loadshape*. Accessed: Nov. 2017. [Online]. Available: http://svn.code.sf.net/p/electricdss/code/trunk/Distrib/EPRITestCircuits/ckt5/

[16] D. Rosewater, R. Baldick, and S. Santoso, "Risk-averse model predictive control design for battery energy storage systems," *IEEE Trans. Smart Grid*, to be published, doi: 10.1109/TSG.2019.2946130.
[17] G. L. Plett, *Battery Management Systems, Volume 1: Battery Modeling*, J. Wang, Ed. Norwood, MA, USA: Artech House, 2015.
[18] A. Y. S. Lam, K.-C. Leung, and V. O. K. Li, "Capacity estimation for vehicle-to-grid frequency regulation services with smart charging mechanism," *IEEE Trans. Smart Grid*, vol. 7, no. 1, pp. 156–166, Jan. 2016, doi: 10.1109/tsg.2015.2436901.
[19] *WECC Battery Storage Dynamic Modeling Guideline*, Standard, Western Electricity Coordinating Council, Salt Lake City, UT, USA, 2016. [Online]. Available: https://www.wecc.org/Reliability/WECC Battery Storage Guideline updates_Bo 4-5-17 SLT 4-7-17 XX SC.docx
[20] H. Mohsenian-Rad, "Coordinated price-maker operation of large energy storage units in nodal energy markets," *IEEE Trans. Power Syst.*, vol. 31, no. 1, pp. 786–797, Jan. 2016, doi: 10.1109/tpwrs.2015.2411556.
[21] J. Donadee and M. D. Ilić, "Stochastic optimization of grid to vehicle frequency regulation capacity bids," *IEEE Trans. Smart Grid*, vol. 5, no. 2, pp. 1061–1069, Mar. 2014, doi: 10.1109/tsg.2013.2290971.
[22] T. Erseghe, A. Zanella, and C. G. Codemo, "Optimal and compact control policies for energy storage units with single and multiple batteries," *IEEE Trans. Smart Grid*, vol. 5, no. 3, pp. 1308–1317, May 2014, doi: 10.1109/TSG.2014.2303824.
[23] Y. Huang, S. Mao, and R. M. Nelms, "Adaptive electricity scheduling in microgrids," *IEEE Trans. Smart Grid*, vol. 5, no. 1, pp. 270–281, Jan. 2014, doi: 10.1109/TSG.2013.2282823.
[24] C. Suazo-Martinez, E. Pereira-Bonvallet, R. Palma-Behnke, and X.-P. Zhang, "Impacts of energy storage on short term operation planning under centralized spot markets," *IEEE Trans. Smart Grid*, vol. 5, no. 2, pp. 1110–1118, Mar. 2014, doi: 10.1109/tsg.2013.2281828.
[25] L. H. Macedo, J. F. Franco, M. J. Rider, and R. Romero, "Optimal operation of distribution networks considering energy storage devices," *IEEE Trans. Smart Grid*, vol. 6, no. 6, pp. 2825–2836, Apr. 2015, doi: 10.1109/tsg.2015.2419134.
[26] R. H. Byrne, M. K. Donnelly, V. W. Loose, and D. J. Trudnowski, "Methodology to determine the technical performance and value proposition for grid-scale energy storage systems," Sandia Nat. Laboratories, Albuquerque, NM, USA, Tech rep. SAND2012-10639, 2012. [Online]. Available: https://www.sandia.gov/ess-ssl/publications/SAND2012-10639.pdf
[27] Y. Wen, C. Guo, H. Pandžić, and D. S. Kirschen, "Enhanced security-constrained unit commitment with emerging utility-scale energy storage," *IEEE Trans. Power Syst.*, vol. 31, no. 1, pp. 652–662, Jan. 2016, doi: 10.1109/tpwrs.2015.2407054.
[28] J. Tant, F. Geth, D. Six, P. Tant, and J. Driesen, "Multiobjective battery storage to improve PV integration in residential distribution grids," *IEEE Trans. Sustain. Energy*, vol. 4, no. 1, pp. 182–191, Jan. 2013, doi: 10.1109/TSTE.2012.2211387.
[29] T. Wang, H. Kamath, and S. Willard, "Control and optimization of grid-tied photovoltaic storage systems using model predictive control," *IEEE Trans. Smart Grid*, vol. 5, no. 2, pp. 1010–1017, Mar. 2014, doi: 10.1109/TSG.2013.2292525.
[30] N. Jayasekara, M. A. S. Masoum, and P. J. Wolfs, "Optimal operation of distributed energy storage systems to improve distribution network load and generation hosting capability," *IEEE Trans. Sustain. Energy*, vol. 7, no. 1, pp. 250–261, Jan. 2016, doi: 10.1109/TSTE.2015.2487360.
[31] EPRI. (Mar. 2011). *OpenDSS STORAGE Element STORAGECONTROLLER Element*. [Online]. Available: http://svn.code.sf.net/p/electricdss/code/trunk/Distrib/Doc/OpenDSS%20STORAGE%20Element.pdf
[32] P. P. Zeng, Z. Wu, X.-P. Zhang, C. Liang, and Y. Zhang, "Model predictive control for energy storage systems in a network with high penetration of renewable energy and limited export capacity," in *Proc. Power Syst. Comput. Conf.*, Aug. 2014, pp. 1–7, doi: 10.1109/PSCC.2014.7038359.
[33] P. Malysz, S. Sirouspour, and A. Emadi, "An optimal energy storage control strategy for grid-connected microgrids," *IEEE Trans. Smart Grid*, vol. 5, no. 4, pp. 1785–1796, Jul. 2014, doi: 10.1109/TSG.2014.2302396.
[34] (2018). *GridLAB-D Wiki: Battery Model*. [Online]. Available: http://gridlab-d.shoutwiki.com/wiki/Battery
[35] X. Qiu, T. A. Nguyen, J. D. Guggenberger, M. L. Crow, and A. C. Elmore, "A field validated model of a vanadium redox flow battery for microgrids," *IEEE Trans. Smart Grids*, vol. 5, no. 4, pp. 1592–1601, Jul. 2014, doi: 10.1109/TSG.2014.2310212.
[36] T. Lambert, P. Gilman, and P. Lilienthal, "Micropower system modeling with HOMER," in *Integration Of Alternative Sources Of Energy*. Hoboken, NJ, USA: Wiley, Apr. 2006, pp. 379–418, doi: 10.1002/0471755621.ch15.
[37] G. Zini, *Green Electrical Energy Storage*, New York, NY, USA: McGraw-Hill, 2016. [Online]. Available: http://www.ebook.de/de/product/26046671/gabriele_zini_green_electrical_energy_storage.html
[38] T. A. Nguyen, D. A. Copp, R. H. Byrne, and B. R. Chalamala, "Market evaluation of energy storage systems incorporating technology-specific nonlinear models," *IEEE Trans. Power Syst.*, vol. 34, no. 5, pp. 3706–3715, Sep. 2019, doi: 10.1109/TPWRS.2019.2909764.
[39] D. A. Copp, T. A. Nguyen, and R. H. Byrne, "Adaptive model predictive control for real-time dispatch of energy storage systems," in *Proc. Amer. Control Conf. (ACC)*, Jul. 2019, pp. 3611–3616. [Online]. Available: https://ieeexplore.ieee.org/document/8814902
[40] S.-K. Kim, J.-Y. Kim, K.-H. Cho, and G. Byeon, "Optimal operation control for multiple BESSs of a large-scale customer under time-based pricing," *IEEE Trans. Power Syst.*, vol. 33, no. 1, pp. 803–816, Jan. 2018, doi: 10.1109/TPWRS.2017.2696571.
[41] S. Grillo, M. Marinelli, S. Massucco, and F. Silvestro, "Optimal management strategy of a battery-based storage system to improve renewable energy integration in distribution networks," *IEEE Trans. Smart Grid*, vol. 3, no. 2, pp. 950–958, Jun. 2012, doi: 10.1109/tsg.2012.2189984.
[42] S. Teleke, M. E. Baran, S. Bhattacharya, and A. Q. Huang, "Optimal control of battery energy storage for wind farm dispatching," *IEEE Trans. Energy Convers.*, vol. 25, no. 3, pp. 787–794, Sep. 2010, doi: 10.1109/tec.2010.2041550.
[43] X. Feng, H. B. Gooi, and S. X. Chen, "Hybrid energy storage with multimode fuzzy power allocator for PV systems," *IEEE Trans. Sustain. Energy*, vol. 5, no. 2, pp. 389–397, Apr. 2014, doi: 10.1109/tste.2013.2290543.
[44] X. Liu, P. Wang, and P. C. Loh, "A hybrid AC/DC microgrid and its coordination control," *IEEE Trans. Smart Grid*, vol. 2, no. 2, pp. 278–286, Jun. 2011, doi: 10.1109/tsg.2011.2116162.
[45] H. H. Abdeltawab and Y. A.-R. I. Mohamed, "Market-oriented energy management of a hybrid wind-battery energy storage system via model predictive control with constraint optimizer," *IEEE Trans. Ind. Electron.*, vol. 62, no. 11, pp. 6658–6670, Nov. 2015, doi: 10.1109/TIE.2015.2435694.
[46] S. J. Moura, J. L. Stein, and H. K. Fathy, "Battery-health conscious power management in plug-in hybrid electric vehicles via electrochemical modeling and stochastic control," *IEEE Trans. Control Syst. Technol.*, vol. 21, no. 3, pp. 679–694, May 2013, doi: 10.1109/TCST.2012.2189773.
[47] Y. Liu, Z. Li, Z. Lin, K. Zhao, and Y. Zhu, "Multi-objective optimization of energy management strategy on hybrid energy storage system based on radau pseudospectral method," *IEEE Access*, vol. 7, pp. 112483–112493, 2019, doi: 10.1109/ACCESS.2019.2935188.
[48] M. Chen and G. A. Rincon-Mora, "Accurate electrical battery model capable of predicting runtime and I-V performance," *IEEE Trans. Energy Convers.*, vol. 21, no. 2, pp. 504–511, Jun. 2006, doi: 10.1109/tec.2006.874229.
[49] A. Rahmoun and H. Biechl, "Modelling of Li-ion batteries using equivalent circuit diagrams," *Przeglad Elektrotechniczny*, vol. 88, no. 7, pp. 152–156, Jan. 2012, [Online]. Available: http://www.red.pe.org.pl/articles/2012/7b/40.pdf
[50] M. Ceraolo, "New dynamical models of lead-acid batteries," *IEEE Trans. Power Syst.*, vol. 15, no. 4, pp. 1184–1190, Nov. 2000, doi: 10.1109/59.898088.
[51] H. E. Perez, X. Hu, S. Dey, and S. J. Moura, "Optimal charging of Li-Ion batteries with coupled electro-thermal-aging dynamics," *IEEE Trans. Veh. Technol.*, vol. 66, no. 9, pp. 7761–7770, Sep. 2017, doi: 10.1109/TVT.2017.2676044.
[52] A. M. Gee, F. V. P. Robinson, and R. W. Dunn, "Analysis of battery lifetime extension in a small-scale wind-energy system using supercapacitors," *IEEE Trans. Energy Convers.*, vol. 28, no. 1, pp. 24–33, Mar. 2013, doi: 10.1109/tec.2012.2228195.
[53] D. K. Karthikeyan, G. Sikha, and R. E. White, "Thermodynamic model development for lithium intercalation electrodes," *J. Power Sources*, vol. 185, pp. 1398–1407, Dec. 2008, doi: 10.1016/j.jpowsour.2008.07.077.

[54] S. Santhanagopalan, Q. Guo, P. Ramadass, and R. E. White, "Review of models for predicting the cycling performance of lithium ion batteries," *J. Power Sour.*, vol. 156, no. 2, pp. 620–628, 2006, doi: 10.1016/j.jpowsour.2005.05.070.

[55] S. Santhanagopalan, Q. Guo, and R. E. White, "Parameter estimation and model discrimination for a lithium-ion cell," *J. Electrochem. Soc.*, vol. 154, no. 3, pp. A198–A206, 2007, doi: 10.1149/1.2422896.

[56] M. Guo and R. White, "Thermal model for lithium ion battery pack with mixed parallel and series configuration," *J. Electrochem. Soc.*, vol. 158, no. 10, pp. A1166–A1176, 2011, doi: 10.1149/1.3624836.

[57] M. Torchio, L. Magni, R. D. Braatz, and D. M. Raimondo, "Design of piecewise affine and linear time-varying model predictive control strategies for advanced battery management systems," *J. Electrochem. Soc.*, vol. 164, no. 4, pp. A949–A959, 2017, doi: 10.1149/2.0201706jes.

[58] M. Torchio, N. A. Wolff, D. M. Raimondo, L. Magni, U. Krewer, R. B. Gopaluni, J. A. Paulson, and R. D. Braatz, "Real-time model predictive control for the optimal charging of a lithium-ion battery," in *Proc. Amer. Control Conf. (ACC)*, Jul. 2015, pp. 4536–4541, doi: 10.1109/ACC.2015.7172043.

[59] M. Bahramipanah, D. Torregrossa, R. Cherkaoui, and M. Paolone, "A decentralized adaptive model-based real-time control for active distribution networks using battery energy storage systems," *IEEE Trans. Smart Grid*, vol. 9, no. 4, pp. 3406–3418, Jul. 2018, doi: 10.1109/tsg.2016.2631569.

[60] R. Baldick, *Applied Optimization: Formulation and Algorithms for Engineering Systems*. Cambridge, U.K.: Cambridge Univ. Press, 2006.

[61] S. Boyd and L. Vandenberghe, *Convex Optimization*, 1st ed. Cambridge, U.K.: Cambridge Univ. Press, 2004. [Online]. Available: https://web.stanford.edu/ boyd/cvxbook/

[62] W. E. Hart, C. D. Laird, J.-P. Watson, D. L. Woodruff, G. A. Hackebeil, B. L. Nicholson, and J. D. Siirola, *Pyomo—Optimization Modeling in Python*, vol. 67, 2nd ed. Cambridge, U.K.: Springer, 2017.

[63] W. E. Hart, J.-P. Watson, and D. L. Woodruff, "Pyomo: Modeling and solving mathematical programs in python," *Math. Program. Comput.*, vol. 3, no. 3, pp. 219–260, 2011, doi: 10.1007/s12532-011-0026-8.

[64] A. Wächter and L. T. Biegler, "On the implementation of an interior-point filter line-search algorithm for large-scale nonlinear programming," *Math. Program.*, vol. 106, no. 1, pp. 25–57, Mar. 2006, doi: 10.1007/s10107-004-0559-y.

[65] D. Linden and T. Reddy, Ed., *Handbook of Batteries*, New York, NY, USA: McGraw-Hill, 2011.

[66] A. R. Sparacino, G. F. Reed, R. J. Kerestes, B. M. Grainger, and Z. T. Smith, "Survey of battery energy storage systems and modeling techniques," in *Proc. IEEE Power Energy Soc. Gen. Meeting*, Jul. 2012, pp. 1–8, doi: 10.1109/PESGM.2012.6345071.

[67] D. Cadar, D. Petreus, I. Ciocan, and P. Dobra, "An improvement on empirical modelling of the batteries," in *Proc. 32nd Int. Spring Seminar Electron. Technol.*, May 2009, pp. 1–6, doi: 10.1109/ISSE.2009.5207015.

[68] G. Wang, M. Ciobotaru, and V. G. Agelidis, "Power management for improved dispatch of utility-scale PV plants," *IEEE Trans. Power Syst.*, vol. 31, no. 3, pp. 2297–2306, May 2016, doi: 10.1109/TPWRS.2015.2459065.

[69] R. Xiong, J. Cao, Q. Yu, H. He, and F. Sun, "Critical review on the battery state of charge estimation methods for electric vehicles," *IEEE Access*, vol. 6, pp. 1832–1843, 2017, doi: 10.1109/ACCESS.2017.2780258.

[70] Y.-H. Kim and H.-D. Ha, "Design of interface circuits with electrical battery models," *IEEE Trans. Ind. Electron.*, vol. 44, no. 1, pp. 81–86, Feb. 1997, doi: 10.1109/41.557502.

[71] A. Hentunen, T. Lehmuspelto, and J. Suomela, "Time-domain parameter extraction method for Thévenin-equivalent circuit battery models," *IEEE Trans. Energy Convers.*, vol. 29, no. 3, pp. 558–566, Sep. 2014, doi: 10.1109/TEC.2014.2318205.

[72] J. F. Manwell and J. G. McGowan, "Lead acid battery storage model for hybrid energy system," *Solar Energy*, vol. 50, no. 5, pp. 399–405, May 1993, doi: 10.1016/0038-092X(93)90060-2.

[73] T. Kim and W. Qiao, "A hybrid battery model capable of capturing dynamic circuit characteristics and nonlinear capacity effects," *IEEE Trans. Energy Convers.*, vol. 26, no. 4, pp. 1172–1180, Dec. 2011, doi: 10.1109/TEC.2011.2167014.

[74] Y. Riffonneau, S. Bacha, F. Barruel, and S. Ploix, "Optimal power flow management for grid connected PV systems with batteries," *IEEE Trans. Sustain. Energy*, vol. 2, no. 3, pp. 309–320, Jul. 2011, doi: 10.1109/tste.2011.2114901.

[75] O. Tremblay and L. Dessaint, "Experimental validation of a battery dynamic model for EV applications," *World Electric Vehicle J.*, vol. 3, pp. 289–298, May 2009, [Online]. Available: https://pdfs.semanticscholar.org/8f16/68ffef08c83a3a69f8f3c557d04cd9a5ffc2.pdf

[76] H. U. R. Habib, S. Wang, M. R. Elkadeem, and M. F. Elmorshedy, "Design optimization and model predictive control of a Standalone hybrid renewable energy system: A case study on a small residential load in Pakistan," *IEEE Access*, vol. 7, pp. 117369–117390, 2019, doi: 10.1109/ACCESS.2019.2936789.

[77] D. L. King, S. Gonzalez, G. M. Galbraith, and W. E. Boyson, "Performance model for grid-connected photovoltaic inverters," Sandia Nat. Laboratories, Albuquerque, NM, USA, Tech Rep. SAND2007-5036, 2007, [Online]. Available: http://energy.sandia.gov/download/21044/

[78] W. Bower, C. Whitaker, W. Erdman, M. Behnke, and M. Fitzgerald, "Performance test protocol for evaluating inverters used in grid-connected photovoltaic systems," Sandia Nat. Laboratories, Albuquerque, NM, USA, Tech. Rep., 2004. [Online]. Available: https://www.gosolarcalifornia.ca.gov/equipment/documents/2004-11-22_Test_Protocol.pdf

[79] G. L. Plett, *Battery Management Systems, Volume II: Equivalent-Circuit Methods*, J. Wang, Ed. Norwood, MA, USA: Artech House, 2016.

[80] L. McCurlie, M. Preindl, and A. Emadi, "Fast model predictive control for redistributive lithium-ion battery balancing," *IEEE Trans. Ind. Electron.*, vol. 64, no. 2, pp. 1350–1357, Feb. 2017, doi: 10.1109/TIE.2016.2611488.

[81] J. Liu, G. Li, and H. K. Fathy, "An extended differential flatness approach for the health-conscious nonlinear model predictive control of lithium-ion batteries," *IEEE Trans. Control Syst. Technol.*, vol. 25, no. 5, pp. 1882–1889, Sep. 2017, doi: 10.1109/TCST.2016.2624143.

[82] X. Han, M. Ouyang, L. Lu, and J. Li, "Simplification of physics-based electrochemical model for lithium ion battery on electric vehicle. Part I: Diffusion simplification and single particle model," *J. Power Sour.*, vol. 278, pp. 802–813, Mar. 2015, doi: 10.1016/j.jpowsour.2014.12.101.

[83] M. Pathak, S. Kolluri, and V. R. Subramanian, "Generic model control for lithium-ion batteries," *J. Electrochem. Soc.*, vol. 164, no. 6, pp. A973–A986, 2017, doi: 10.1149/2.1521704jes.

[84] N. A. Chaturvedi, R. Klein, J. Christensen, J. Ahmed, and A. Kojic, "Modeling, estimation, and control challenges for lithium-ion batteries," in *Proc. Amer. Control Conf.*, Jun. /Jul. 2010, pp. 1997–2002, doi: 10.1109/ACC.2010.5531623.

[85] G. Ning and B. N. Popov, "Cycle life modeling of lithium-ion batteries," *J. Electrochem. Soc.*, vol. 151, no. 10, pp. A1584–A1591, 2004, doi: 10.1149/1.1787631.

[86] W. M. Deen, *Analysis Of Transport Phenomena*, K. E. Gubbins, Ed. Oxford, U.K.: Oxford Univ. Press, 1998.

[87] C. Y. Wang and W. B. Gu, "Micro-macroscopic coupled modeling of batteries and fuel cells: I. model development," *J. Electrochem. Soc.*, vol. 145, no. 10, pp. 3407–3417, 1998, doi: 10.1149/1.1838820.

[88] M. Guo, G. Sikha, and R. E. White, "Single-particle model for a lithium-ion cell: Thermal behavior," *J. Electrochem. Soc.*, vol. 158, no. 2, pp. A122–A132, 2011, doi: 10.1149/1.3521314.

[89] X. Han, M. Ouyang, L. Lu, and J. Li, "Simplification of physics-based electrochemical model for lithium ion battery on electric vehicle. Part II: Pseudo-two-dimensional model simplification and state of charge estimation," *J. Power Sour.*, vol. 278, pp. 814–825, Mar. 2015, doi: 10.1016/j.jpowsour.2014.08.089.

[90] A. Jokar, B. Rajabloo, and M. Désilets, and M. Lacroix, "Review of simplified pseudo-two-dimensional models of lithium-ion batteries," *J. Power Source*, vol. 327, pp. 44–55, Sep. 2016, doi: 10.1016/j.jpowsour.2016.07.036.

[91] T. F. Fuller, M. Doyle, and J. Newman, "Simulation and optimization of the dual lithium ion insertion cell," *J. Electrochem. Soc.*, vol. 141, no. 1, pp. 1–10, 1994, doi: 10.1149/1.2054684.

[92] *Specification Li-ion Polymer Battery 3.7V 10000 mAh*, 2nd ed. Richmond, CA USA: AA Portable Power Group, 2004, [Online]. Available: https://www.batteryspace.com/prod-specs/3.7V9059156.pdf

[93] Q. Wang, B. Jiang, B. Li, and Y. Yan, "A critical review of thermal management models and solutions of lithium-ion batteries for the development of pure electric vehicles," *Renew. Sustain. Energy Rev.*, vol. 64, pp. 106–128, Oct. 2016, doi: 10.1016/j.rser.2016.05.033.

[94] G.-H. Kim, K. Smith, K.-J. Lee, S. Santhanagopalan, and A. Pesaran, "Multi-domain modeling of lithium-ion batteries encompassing multi-physics in varied length scales," *J. Electrochem. Soc.*, vol. 158, no. 8, pp. A955–A969, 2011, doi: 10.1149/1.3597614.

[95] S. Barsali and M. Ceraolo, "Dynamical models of lead-acid batteries: Implementation issues," *IEEE Trans. Energy Convers.*, vol. 17, no. 1, pp. 16–23, Mar. 2002, doi: 10.1109/60.986432.
[96] T. I. Bø and T. A. Johansen, "Battery power smoothing control in a marine electric power plant using nonlinear model predictive control," *IEEE Trans. Control Syst. Technol.*, vol. 25, no. 4, pp. 1449–1456, Jul. 2017, doi: 10.1109/TCST.2016.2601301.
[97] C. Masjosthusmann, U. Köhler, N. Decius, and U. Büker, "A vehicle energy management system for a battery electric vehicle," in *Proc. IEEE Vehicle Power Propuls. Conf.*, Oct. 2012, pp. 339–344, doi: 10.1109/VPPC.2012.6422676.
[98] S. Mohan, J. B. Siegel, A. G. Stefanopoulou, and R. Vasudevan, "An energy-optimal warm-up strategy for Li-Ion batteries and its approximations," *IEEE Trans. Control Syst. Technol.*, vol. 27, no. 3, pp. 1165–1180, Mar. 2018, doi: 10.1109/TCST.2017.2785833.
[99] H. E. Perez, S. Dey, X. Hu, and S. J. Moura, "Optimal charging of Li-Ion batteries via a single particle model with electrolyte and thermal dynamics," *J. Electrochem. Soc.*, vol. 164, no. 7, pp. A1679–A1687, 2017, doi: 10.1149/2.1301707jes.
[100] P. H. L. Notten, W. S. Kruijt, and H. J. Bergveld, "Electronic network modeling of rechargeable batteries: II. the NiCd system," *J. Electrochem. Soc.*, vol. 145, no. 11, Nov. 1998, doi: 10.1149/1.1838872.
[101] D. Rosewater, A. Headley, F. A. Mier, and S. Santoso, "Optimal control of a battery energy storage system with a charge-temperature-health model," in *Proc. IEEE PES GM*, Atlanta, GA, USA, Aug. 2019.
[102] H. E. Perez, X. Hu, and S. J. Moura, "Optimal charging of batteries via a single particle model with electrolyte and thermal dynamics," in *Proc. Amer. Control Conf. (ACC)*, Jul. 2016, pp. 4000–4005, doi: 10.1109/ACC.2016.7525538.
[103] H. J. Bergveld, W. S. Kruijt, and P. H. L. Notten, *Battery Management Systems: Design by Modelling* (Battery Modeling). Berlin, Germany: Springer, 2005.
[104] V. Viswanathan, D. W. D. Choi, S. T. W. Xu, R. E. Williford, J.-G. Zhang, J. Liu, and Z. Yang, "Effect of entropy change of lithium intercalation in cathodes and anodes on Li-ion battery thermal management," *J. Power Sour.*, vol. 195, no. 11, pp. 3720–3729, 2010, doi: 10.1016/j.jpowsour.2009.11.103.
[105] T. M. Bandhauer, S. Garimella, and T. F. Fuller, "A critical review of thermal issues in lithium-ion batteries," *J. Electrochem. Soc.*, vol. 158, no. 3, pp. R1–R25, 2011, doi: 10.1149/1.3515880.
[106] D. Berndt, "Valve-regulated lead-acid batteries," *J. Power Sour.*, no. 100, pp. 29–46, Nov. 2001, doi: 10.1016/S0378-7753(01)00881-3.
[107] T. Bergman, A. Lavine, F. Incropera, and D. Dewitt, *Fundamentals of Heat and Mass Transfer*, L. Ratts, Ed. Hoboken, NJ, USA: Wiley, 2011.
[108] N. F. Ponchaut, F. Colella, V. Somandepalli, and M. Stern, "Thermal management modeling for thermal runaway avoidance in lithium-ion batteries," in *Proc. SAE World Congr. Exhib.*, Detroit, MI, USA, 2014, doi: 10.4271/2014-01-0707.
[109] *ENERGY STAR Program Requirements for Air Source Heat Pump (ASHP) and Central Air Conditioner Equipment - Eligibility Criteria*, 3rd ed. Washington, DC, USA, Environmental Protection Agency. [Online]. Available: https://www.energystar.gov/sites/default/files/specs/private/Room_Air_Conditioner_Program_Requirements_Version_3.pdf
[110] M. B. Pinson and M. Z. Bazant, "Theory of SEI formation in rechargeable batteries: Capacity fade, accelerated aging and lifetime prediction," *J. Electrochem. Soc.*, vol. 160, no. 2, pp. A243–A250, 2013, doi: 10.1149/2.044302jes.
[111] P. Arora, M. Doyle, and R. E. White, "Mathematical modeling of the lithium deposition overcharge reaction in lithium-ion batteries using carbon-based negative electrodes," *J. Electrochem. Soc.*, vol. 146, no. 10, pp. 3543–3553, 1999, doi: 10.1149/1.1392512.
[112] B. Suthar, P. W. C. Northrop, R. D. Braatz, and V. R. Subramanian, "Optimal charging profiles with minimal intercalation-induced stresses for lithium-ion batteries using reformulated pseudo 2-dimensional models," *J. Electrochem. Soc.*, vol. 161, no. 11, pp. F3144–F3155, 2014, doi: 10.1149/2.0211411jes.
[113] Y.-T. Cheng and M. W. Verbrugge, "Evolution of stress within a spherical insertion electrode particle under potentiostatic and galvanostatic operation," *J. Power Sour.*, vol. 190, no. 2, pp. 453–460, 2009, doi: 10.1016/j.jpowsour.2009.01.021.
[114] U. Car, "Battery test manual for electric vehicles," Idaho Nat. Lab., Idaho Falls, ID, USA, Tech Rep. INL/EXT-15-34184 2015, [Online]. Available: http://www.uscar.org/commands/files_download.php?files_id=405
[115] Y. Wang, Z. Song, V. D. Angelis, and S. Srivastava, "Battery life-cycle optimization and runtime control for commercial buildings demand side management: A new york city case study," *Energy*, vol. 165, pp. 782–791, Dec. 2018, doi: 10.1016/j.energy.2018.09.117.
[116] S. Ebbesen, P. Elbert, and L. Guzzella, "Battery state-of-health perceptive energy management for hybrid electric vehicles," *IEEE Trans. Veh. Technol.*, vol. 61, no. 7, pp. 2893–2900, Sep. 2012, doi: 10.1109/TVT.2012.2203836.
[117] C. Vagg, S. Akehurst, C. J. Brace, and L. Ash, "Stochastic dynamic programming in the real-world control of hybrid electric vehicles," *IEEE Trans. Control Syst. Technol.*, vol. 24, no. 3, pp. 853–866, May 2016, doi: 10.1109/TCST.2015.2498141.
[118] C. Vagg, C. J. Brace, S. Akehurst, and L. Ash, "Minimizing battery stress during hybrid electric vehicle control design: Real world considerations for model-based control development," in *Proc. IEEE Vehicle Power Propuls. Conf. (VPPC)*, Oct. 2013, pp. 1–6, doi: 10.1109/VPPC.2013.6671713.
[119] E. Vinot, R. Trigui, and B. Jeanneret, "Optimal management of electric vehicles with a hybrid storage system," in *Proc. IEEE Vehicle Power Propuls. Conf.*, Sep. 2010, pp. 1–6, doi: 10.1109/VPPC.2010.5729126.
[120] Y. Tian, A. Bera, J. Mitra, B. Chalamala, and R. H. Byrne, "Effect of operating strategies on the longevity of lithium-ion battery energy storage systems," in *Proc. IEEE Ind. Appl. Soc. Annu. Meeting (IAS)*, Sep. 2018, pp. 1–8, doi: 10.1109/IAS.2018.8544518.
[121] B. Xu, A. Oudalov, A. Ulbig, G. Andersson, and D. S. Kirschen, "Modeling of lithium-ion battery degradation for cell life assessment," *IEEE Trans. Smart Grid*, vol. 9, no. 2, pp. 1131–1140, Mar. 2018, doi: 10.1109/TSG.2016.2578950.
[122] Y. Niu and S. Santoso, "Sizing and coordinating fast- and slow-response energy storage systems to mitigate hourly wind power variations," *IEEE Trans. Smart Grid*, vol. 9, no. 2, pp. 1107–1117, Mar. 2018, doi: 10.1109/tsg.2016.2577549.
[123] X. Ke, N. Lu, and C. Jin, "Control and size energy storage systems for managing energy imbalance of variable generation resources," *IEEE Trans. Sustain. Energy*, vol. 6, no. 1, pp. 70–78, Jan. 2015, doi: 10.1109/tste.2014.2355829.
[124] B. Xu, J. Zhao, T. Zheng, E. Litvinov, and D. S. Kirschen, "Factoring the cycle aging cost of batteries participating in electricity markets," *IEEE Trans. Power Syst.*, vol. 33, no. 2, pp. 2248–2259, Mar. 2018, doi: 10.1109/TPWRS.2017.2733339.
[125] Y. Shi, B. Xu, Y. Tan, D. Kirschen, and B. Zhang, "Optimal battery control under cycle aging mechanisms in pay for performance settings," *IEEE Trans. Autom. Control*, vol. 64, no. 6, pp. 2324–2339, Jun. 2019, doi: 10.1109/TAC.2018.2867507.
[126] H. Bindner, T. Cronin, P. Lundsager, J. Manwell, U. Abdulwahid, and I. Baring-Gould, *English Lifetime Modelling Of Lead Acid Batteries*. Roskilde, Denmark: Risø Nat. Lab., 2005. [Online]. Available: https://orbit.dtu.dk/fedora/objects/orbit:88309/datastreams/file_7710966/content
[127] J. M. Reniers, G. Mulder, and S. Ober-Blöbaum, and D. A. Howey, "Improving optimal control of grid-connected lithium-ion batteries through more accurate battery and degradation modelling," *J. Power Sour.*, vol. 379, pp. 91–102, 2018, doi: 10.1016/j.jpowsour.2018.01.004.
[128] J. Christensen and J. Newman, "Cyclable lithium and capacity loss in Li-Ion cells," *J. Electrochem. Soc.*, vol. 152, no. 4, pp. A818–A829, 2005, doi: 10.1149/1.1870752.
[129] M. Safari, M. Morcrette, A. Teyssot, and C. Delacourt, "Multimodal physics-based aging model for life prediction of Li-ion batteries," *J. Electrochem. Soc.*, vol. 156, no. 3, pp. A145–A153, 2009, doi: 10.1149/1.3043429.
[130] M. K. S. Verma, S. Basu, K. S. Hariharan, S. M. Kolake, T. Song, and J. Jeon, "A strain-diffusion coupled electrochemical model for lithium-ion battery," *J. Electrochem. Soc.*, vol. 164, no. 13, pp. A3426–A3439, 2017, doi: 10.1149/2.0021714jes.
[131] M. Safari, M. Morcrette, A. Teyssot, and C. Delacourt, "Life-prediction methods for lithium-ion batteries derived from a fatigue approach i. introduction: Capacity-loss prediction based on damage accumulation," *J. Electrochem. Soc.*, vol. 157, no. 6, pp. A713–A720, 2010, doi: 10.1149/1.3374634.
[132] J. Schmalstieg and S. Käbitz, M. Ecker, and D. U. Sauer, "A holistic aging model for Li(NiMnCo)O_2 based 18650 lithium-ion batteries," *J. Power Source*, vol. 257, pp. 325–334, Jul. 2014, doi: 10.1016/j.jpowsour.2014.02.012.

[133] Y. Cui, C. Du, G. Yin, Y. Gao, L. Zhang, T. Guan, L. Yang, and F. Wang, "Multi-stress factor model for cycle lifetime prediction of lithium ion batteries with shallow-depth discharge," *J. Power Sources*, vol. 279, pp. 123–132, Apr. 2015, doi: 10.1016/j.jpowsour.2015.01.003.

[134] J. Wang, J. Purewal, P. Liu, J. Hicks-Garner, S. Soukazian, E. Sherman, A. Sorenson, L. Vu, H. Tataria, and M. W. Verbrugge, "Degradation of lithium ion batteries employing graphite negatives and nickel-cobalt-manganese oxid + spinel manganese oxide positives: Part 1, aging mechanisms and life estimation," *J. Power Sour.*, vol. 269, pp. 937–948, Dec. 2014, doi: 10.1016/j.jpowsour.2014.07.030.

[135] S. D. Downing and D. F. Socie, "Simple rainflow counting algorithms," *Int. J. Fatigue*, vol. 4, no. 1, pp. 31–40, Jan. 1982, doi: 10.1016/0142-1123(82)90018-4.

[136] E. Thomas, I. Bloom, J. Christophersen, and V. Battaglia, "Statistical methodology for predicting the life of lithium-ion cells via accelerated degradation testing," *J. Power Source*, vol. 184, no. 1, pp. 312–317, 2008, doi: 10.1016/j.jpowsour.2008.06.017.

[137] M. Ecker, J. B. Gerschler, J. Vogel, S. Kabitz, F. Hust, P. Dechent, and D. U. Sauer, "Development of a lifetime prediction model for lithium-ion batteries based on extended accelerated aging test data," *J. Power Source*, vol. 215, pp. 248–257, Oct. 2012, doi: 10.1016/j.jpowsour.2012.05.012.

[138] K. Abdulla, J. de Hoog, V. Muenzel, F. Suits, K. Steer, A. Wirth, and S. Halgamuge, "Optimal operation of energy storage systems considering forecasts and battery degradation," *IEEE Trans. Smart Grid*, vol. 9, no. 3, pp. 2086–2096, May 2018, doi: 10.1109/TSG.2016.2606490.

[139] M. R. Palacin and A. de Guibert, "Why do batteries fail?" *Science*, vol. 351, no. 6273, Feb. 2016, Art. no. 1253292, doi: 10.1126/science.1253292.

[140] Y. K. Lee, J. Park, and W. Lu, "A comprehensive experimental and modeling study on dissolution in Li-Ion batteries," *J. Electrochem. Soc.*, vol. 166, no. 8, pp. A1340–A1354, 2019, doi: 10.1149/2.0111908jes.

[141] T. Lu, Y. Luo, Y. Zhang, W. Luo, L. Yan, and J. Xie, "Degradation analysis of commercial lithium-ion battery in long-term storage," *J. Electrochem. Soc.*, vol. 164, no. 4, pp. A775–A784, 2017, doi: 10.1149/2.1321704jes.

[142] J. Wang, P. Liu, J. Hicks-Garner, E. Sherman, S. Soukiazian, M. Verbrugge, H. Tataria, J. Musser, and P. Finamore, "Cycle-life model for graphite-lifepo4 cells," *J. Power Source*, vol. 196, no. 8, pp. 3942–3948, 2011, doi: 10.1016/j.jpowsour.2010.11.134.

[143] P. Arorat, R. E. White, and M. Doyle, "Capacity fade mechanisms and side reactions in lithium-ion batteries," *J. Electrochem. Soc.*, vol. 145, no. 10, pp. 3647–3667, 1998, doi: 10.1149/1.1838857.

[144] T. Waldmann, B.-I. Hogg, and M. Wohlfahrt-Mehrens, "Li plating as unwanted side reaction in commercial Li-ion cells—A review," *J. Power Source*, vol. 384, pp. 107–124, Apr. 2018, doi: 10.1016/j.jpowsour.2018.02.063.

[145] P. Ramadass, B. Haran, P. M. Gomadam, R. White, and B. N. Popov, "Development of first principles capacity fade model for Li-Ion cells," *J. Electrochem. Soc.*, vol. 151, no. 2, pp. A196–A203, 2004, doi: 10.1149/1.1634273.

DAVID M. ROSEWATER (M'11) is currently pursuing the Ph.D. degree in electrical and computer engineering with UT Austin. He worked with the Idaho National Laboratory developing advanced spectral impedance measurement techniques for hybrid vehicle battery cells. He is currently a Senior Member of the Technical Staff with the Sandia National Laboratories. He researches applications of energy storage technologies in electric power systems. His research interests include modeling and simulation, performance testing, safety, and standardization of battery energy storage systems.

DAVID A. COPP received the B.S. degree in mechanical engineering from the University of Arizona and the M.S. and Ph.D. degrees in mechanical engineering from the University of California, Santa Barbara. He was a Senior Member of the Technical Staff with the Sandia National Laboratories and an Adjunct Faculty Member in electrical and computer engineering with the University of New Mexico. He is currently an Assistant Professor of teaching with the Department of Mechanical and Aerospace Engineering, University of California, Irvine. His broad research interests include engineering education, as well as control and optimization of nonlinear and hybrid systems with applications to power and energy systems, multiagent systems, robotics, and biomedicine. He was a recipient of the UCSB's Center for Control, Dynamical Systems, and the Computation Best Ph.D. Thesis Award.

TU A. NGUYEN received the B.S. degree in power systems from the Hanoi University of Science and Technology, Vietnam, in 2007, and the Ph.D. degree from the Missouri University of Science and Technology, in December 2014. He was worked as a Power Transformer Test Engineer with the ABB High Voltage Test Department, Vietnam, from 2008 to 2009. He was worked as a Postdoctoral Research Associate with the University of Washington. In September 2016, he joined the Sandia National Laboratories, where he is currently a Senior Member of the Technical Staff. His research interests include energy storage economics, microgrid modeling and analysis, and the integration of distributed resources into power grids.

RAYMOND H. BYRNE (F'17) received the B.S. degree in electrical engineering from the University of Virginia, the M.S. degree in electrical engineering from the University of Colorado, the M.S. degree in financial mathematics (financial engineering) from The University of Chicago, and the Ph.D. degree in electrical engineering from The University of New Mexico. He is currently a Distinguished Member of the Technical Staff with the Sandia National Laboratories, where he has been employed, since 1989. He also serves as the Team Lead of the Equitable Regulatory Environment thrust area of the Sandia energy storage program. He was elevated to the IEEE Fellow for contributions to miniature robotics and grid integration of energy storage, in 2017. He is a member of Tau Beta Pi, Eta Kappa Nu, and Sigma Xi. He was recipient of several awards, including Time Magazine invention of the year in robotics, in 2001, and the Prize Paper Award at the 2016 IEEE Power and Energy Society General Meeting for a article on maximizing revenue from energy storage in grid applications.

SURYA SANTOSO (F'15) received the B.S. degree from Satya Wacana Christian University, Salatiga, Indonesia, in 1992, and the M.S.E. and Ph.D. degrees in electrical and computer engineering from The University of Texas at Austin, in 1994 and 1996, respectively. He was a Senior Power Systems and Consulting Engineer with Electrotek Concepts, Knoxville, TN, USA, from 1997 to 2003. He joined the faculty of The University of Texas at Austin, in 2003, where he is currently a Professor of electrical and computer engineering. He is a coauthor of *Electrical Power Systems Quality* (third edition), sole author of *Fundamentals of Electric Power Quality*, and an Editor of *Handbook of Electric Power Calculations* (fourth edition) and *Standard Handbook for Electrical Engineers* (17th edition). His research interests include power quality, power systems, and renewable energy integration in transmission, and distribution systems.